Daniel Mackner, BSc

Quantitative MRI - analysis and clinical evaluation of simultaneous intrinsic parameter quantification

MASTER'S THESIS

to achieve the university degree of

Diplom-Ingenieur

Master's degree programme: Biomedical Engineering

submitted to

Graz University of Technology

Supervisor

Univ.-Prof. Dipl.-Ing. Dr.techn.
Rudolf Stollberger

Institute of Medical Engineering
Stremayrgasse 16/III, A-8010 Graz

Graz, December 2021

STATUATORY DECLARATION

I declare that I have authored this thesis independently, that I have not used other than the declared sources/resources, and that I have explicitly indicated all material which has been quoted either literally or by content from the sources used. The text document uploaded to TUGRAZonline is identical to the present master‘s thesis dissertation.

_____ _____

Daniel MACKNER

Acknowledgments

First and foremost I want to owe Prof. Rudolf Stollberger for supervising the thesis with his valuable inspirations and the competent expertise as well as supporting me with helpful discussions.

I would also like to thank Prof. Erich Sorantin for the possibility to gather experience in a clinical environment, for his inspiring discussions and the chance to present the topic at congresses. Also I want to thank Dr. Veronika Weiss for conducting these presentations with me and the medical expertise. Furthermore I want to thank DDr. Sebastian Tschauner, Dr. Alexander Pilhatsch, Dr. Georg Apfaltrer, Dr. Franz Lindbichler and Dr. Doris Zebedin for the assessment of the images and the useful discussions.

A special thank goes to Dr. Peter Opriessnig and Dr. Oliver Maier for their help and expertise regarding the practical measurements on the scanners and many hours of interesting discussions.

My thanks also go to my colleagues and friends in Graz for making the past couple of years a special experience, especially Omar Saracevic for proof reading this thesis.

Finally, I want to express my gratitude to my parents, Doris and Christian, who gave me the opportunity to study and supported me always. I want to thank my sister Sophie and especially Isabella, for always motivating and encouraging me.

Abstract

Quantitative Magnetic Resonance Imaging (qMRI) has the potential to overcome some issues posed by conventional MRI including the necessarity of multiple acquisitions with different settings for Repetition Time (T_R) and Echo Time (T_E) as well as segmentation. The major drawback of quantification sequences is the prolonged scan time which prevents a clinical usage. With the QRAPMASTER sequence it is possible to quantify simultaneously the Longitudinal Relaxation Time (T_1), Transversal Relaxation Time (T_2), Proton Density (PD) and the RF field B_1 of the whole brain within seven minutes. These maps allow for a synthetic image reconstruction with retrospective setting of the parameters. A validated model is the basis for a fully automatic characterization of the tissue in white, grey matter and cerebrospinal fluid clusters. The determination of myelin, which is crucial for a variety of neurodegenerative diseases, can be processed by additionally taking Magnetization Transfer (MT) effects into consideration.

The accuracy of the QRAPMASTER determination was compared to gold-standard methods revealing a precise and reliable parameter quantification. Synthetic and conventional images were compared objectively with the Structural Similarity Index (SSIM) and subjectively by radiologists indicating a restricted potential for replacement and a limited acceptance by the users. The benefits for clinical usage of this technique include a better contrast between white and grey matter in synthetic images and an objective determination of different tissue types, especially myelin.

Keywords: quantitative MRI, synthetic MRI, automatic brain segmentation, myelin measurement, white/grey matter contrast

Kurzfassung

Quantitative Magnetresonanzbildgebung (qMRI) hat das Potential gewisse Probleme des konventionellen MRI, wie zum Beispiel die Notwendigkeit mehrerer Messungen mit unterschiedlichen Kontrasteinstellung mittels Variation von Repetitions- (T_R) und Echozeit (T_E) und auch Segmentierung, zu bewältigen. Ein großer Nachteil quantitativer Sequenzen ist die lange Akquisitionszeit, welche eine klinische Anwendung verhindert. Mit der QRAPMASTER Sequenz ist es möglich, die longitudinale (T_1) und transversale Relaxationszeit (T_2), die Protonendichte und das Hochfrequenzfeld B_1 gleichzeitig, innerhalb von 7 Minuten für das gesamte Gehirnvolumen zu bestimmen. Die quantitativen Karten ermöglichen eine synthetische Bildrekonstruktion mit retrospektiver Einstellung der Parameter. Ein validiertes Modell ermöglicht die Klassifizierung in weißer und grauer Substanz sowie Hirn- und Rückenmarksflüssigkeiten. Die Bestimmung der Myelinisierung, welche entscheidend für eine Vielzahl von neurodegenerativen Erkrankungen ist, erfolgt mit einem weiteren Modell, welches zusätzlich Magnetisierungstransfer (MT) in Betracht zieht.

Die Genauigkeit des QRAPMASTER Ansatzes wurde mit gängigen Gold-Standard Methoden verglichen und zeigte eine präzise und zuverlässige Parameterquantifizierung. Synthetisch erzeugte und konventionell akquirierte Bilder wurden objektiv mit dem Structural Similarity Index (SSIM) und durch subjektive Einschätzung von Radiologen verglichen und zeigte ein beschränktes Potential für den Ersatz sowie eine limitierte Akzeptanz der Benutzer. Die Vorteile für die klinische Anwendung der Technik sind zum einen der bessere Kontrast zwischen weißer und grauer Substanz in synthetischen Bildern und zum anderen die objektive Bestimmung der verschiedenen Gewebearten, im Speziellen Myelin.

Schlüsselwörter: quantitatives MR, synthetisches MR, automatische Gehirnsegmentierung, Myelinbestimmung, weißer/grauer Substanz Kontrast

Table of contents

Abbreviations

T_1 Longitudinal Relaxation Time. iii, 3–15, 17–19, 21, 23, 26, 38–43, 45, 47, 50–52, 55–58, 64–67, 69–75, 78, 79, 81

T_2 Transversal Relaxation Time. iii, 2–10, 12–14, 18, 19, 21–23, 26, 27, 32, 35, 38, 42–45, 47, 52, 53, 55–58, 65, 68–75, 78–81

T_E Echo Time. iii, 3–8, 10, 11, 28, 30, 35, 38, 39, 41–45, 47, 55, 56, 76

T_I Inversion time. 4, 6, 7, 28, 30, 38, 39, 43, 47

T_R Repetition Time. iii, 4–8, 10, 35, 39–41, 43–45, 47, 55, 56, 65–67, 76

BPF Brain Parenchym Fraction. 22, 76

BPV Brain Parenchym Volume. 22, 76

bSSFP balanced Steady-State Free Precession. 9, 10, 26

CSF Cerebrospinal Fluid. 6, 19–22, 27, 28, 39, 64, 66–68, 71, 76, 77

DAM Double Angle Method. 41, 44

DESPOT1 Driven Equilibrium Single Pulse Observation of T_1. 40

DIR Double Inversion-Recovery. 8

FID Free Induction Decay. 2, 3

FLAIR Fluid-Attenuated Inversion Recovery. 4, 6, 8, 46, 47, 57, 58, 71–75, 81

FoV Field Of View. 35, 44, 46, 47

GM Grey Matter. 5, 6, 19–22, 27, 32, 37, 47, 48, 55, 56, 58, 59, 67, 69, 73, 74, 76, 79, 81

GRE Gradient Echo. 11, 12, 44

ICV Intracranial Volume. 22, 31, 47, 48, 56, 57, 71–73, 76, 78

IR Inversion-Recovery. 9, 10, 38–40, 43, 45, 50, 51, 64–66, 69, 70, 81

LL Look-Locker. 11

MDME Multi-Dynamic, Multi-Echo. 10, 38, 43, 45–47, 50–56, 64, 66–70, 75, 78

MRF Magnetic Resonance Fingerprinting. 9, 10

MRI Magnetic Resonance Imaging. iii, 1, 4–9, 22, 23, 32, 33, 43, 46, 82

MSE Multi Spin Echo. 42, 43, 52, 53, 64, 65, 68–70, 81

MT Magnetization Transfer. iii, 23, 26, 27, 32, 37, 70, 79, 80, 82

MTC Magnetization Transfer Contrast. 44

MTR Magnetization Transfer Ratio. 45, 55, 64, 70, 79–81

PACS Picture Archiving and Communication System. 47

PD Proton Density. iii, 4, 5, 7–9, 11, 18–22, 27, 28, 38, 47, 70, 79

qMRI Quantitative Magnetic Resonance Imaging. iii, 1, 4, 7, 9, 21, 27, 64

QRAPMASTER Quantification of Relaxation Times and Proton Density by Multiecho Acquisition of a Saturation-Recovery using Turbo-Spin-Echo Readout. iii, iv, 10–14, 20, 26, 30, 32, 37, 38, 50, 52, 64, 65, 67, 70, 73–76, 79, 81

QRAPTEST Quantification of Relaxation Times and Proton Density by Twin-Echo Saturation-Recovery Turbo-Field-Echo. 10–12

RF Radiofrequency. iii, 2–4, 7, 13–17, 19, 20, 23–25, 28, 41, 43, 45, 80

SE Spin Echo. 3–5, 12, 13, 17, 37–39, 41–46, 52, 53, 55, 56, 69, 78, 79

SNR Signal-To-Noise Ratio. 4, 12, 20, 38, 39, 41, 61, 68

SPGR Spoiled Gradient Echo. 26, 40

SR Saturation-Recovery. 38

SSIM Structural Similarity Index. iii, 32–36, 47–50, 56, 57, 61–63, 71–73, 81

STIR Short-Tau Inversion Recovery. 8

TSE Turbo Spin Echo. 12, 13, 35, 37, 44, 45, 55, 56, 78, 79

VFA Variable Flip Angle. 40, 41, 50, 51, 64, 65, 69

WM White Matter. 5, 6, 19–22, 27, 32, 37, 47, 48, 55, 56, 58, 59, 67, 69, 73, 74, 76, 79, 81

1 Introduction

Magnetic Resonance Imaging (MRI) is commonly used in radiology to image the anatomy and (patho-) physiological processes with high soft-tissue contrast and the ability to gain functional information. This sophisticated method is a versatile technique offering the possibility to examine a variety of organs and body regions. The most commonly scanned region is the brain (neuroimaging) due to the fact that MRI provides in general plenty of information about this complex organ and especially a better contrast between grey and white matter. Besides the diagnosis of pathologies like the majority of cancers and tumors, MRI is the method of choice for staging, follow-up, pre- and postoperative states because it does not involve the use of ionizing radiation and therefore the patient is not exposed to hazards. However, the intensity in the images is highly dependent on a wide range of different parameters besides the physical quantity of the examined tissue. Therefore, Quantitative Magnetic Resonance Imaging (qMRI), e.g., methods for the determination of intrinsic parameters causing the signal, has become a highly focused topic in research.

1.1 MRI background

The MRI signal is based on the electromagnetic field of precessing protons (in general hydrogen nuclei) present in water, fat and other biological tissues. In presence of an external magnetic field, named B_0 and arbitrary defined along the z-axis, the precession axis of the protons is aligned parallel or anti-parallel in z-direction. The net magnetization in this direction is the longitudinal magnetization M_z and is defined in the equilibrium state as M_0. All of the nuclei precess with a specific frequency, i.e., the Lamor frequency (ω_L) which is dependent on the static magnetic field B_0 and the gyromagnetic constant

for hydrogen nuclei ($\gamma_{H+} = 42.58MHz/T$) and can be calculated as follows:

$$\omega_L = \gamma_{H+} B_0 \tag{1.1}$$

Since the spins are out of phase in the equilibrium state, the transversal component M_{xy} is initially null.

With the application of an Radiofrequency (RF) excitation pulse with the amplitude B_1 by the RF coils the spins align in-phase and the energy absorption causes parallel precession axes to become anti-parallel aligned. Macroscopically, the net magnetization is flipped in the direction of the transversal plane with the flip angle according to

$$\alpha = \gamma B_1 t_p \tag{1.2}$$

where t_p is the pulse duration of the RF pulse.

The rotating magnetization in the transversal plane can be measured by an induced voltage in the RF coils perpendicular to this plane. The damped oscillation observed is the Free Induction Decay (FID) exponentially decaying with T_2^*. The FID includes the transversal relaxation with the parameter Transversal Relaxation Time (T_2) and also $T_{2'}$ according to equation 1.3

$$\frac{1}{T_2^*} = \frac{1}{T_2} + \frac{1}{T_{2'}} \tag{1.3}$$

While the variable $T_{2'}$ is due to technical reasons like the inhomogeneity of B_0, T_2 is caused by the tissue and therefore the parameter of main interest. The T_2 decay is also called spin-spin relaxation named after the reason for this effect. After an excitation, e.g. a 90° pulse, numerous spins are in phase but adjacents spins provoke a small change of the resonance frequency and the resulting phase dispersion or dephasing causes the transversal magnetization and therefore also the signal to decay, mathematically described with:

$$M_{xy}(t) = M_0 \exp^{-\frac{t}{T_2}} \tag{1.4}$$

This effect is random and irreversible in contrary to the $T_{2'}$ decay which can be rephased by an 180° RF pulse due to the fact that the inhomogeneities are constant in time and

space. This basic principle is known as Spin Echo (SE) and shown in figure 1.1

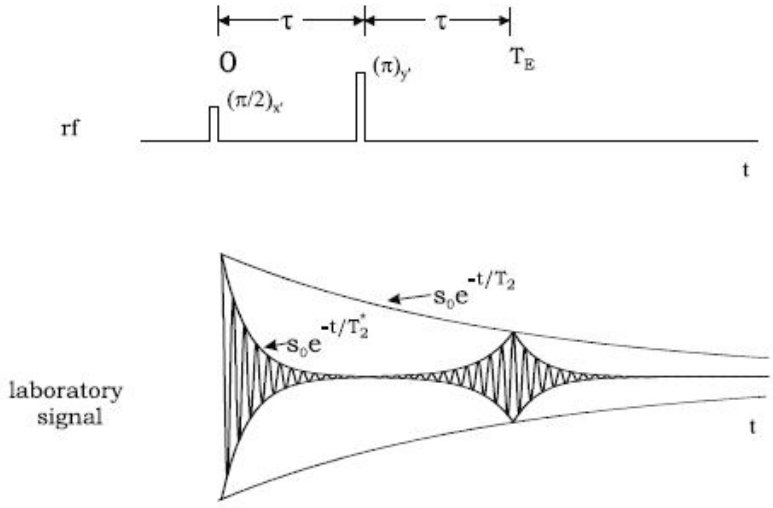

Figure 1.1: Spin echo acquisition scheme with a 90° excitation and 180° refocusing pulse. The FID with T_2^*, and the maximum rephased echo at T_E with the T_2 evelope, from [1]

In order to return to the equilibrium state, another relaxation process has to take place. The energy transferred by the RF pulse and absorbed by the spins has to be dissipated by coupling it from the hydrogen nuclei to other magnetic moments present in the environment like other species of nuclei and electrons through collisions, rotations or electromagnetic interactions. This dipole-dipole interaction is the most important interaction to bring the spins in the lower energy state, i.e. parallel to the magnetic field, by stimulated emission. The whole effect of longitudinal relaxation is also called spin-lattice relaxation and can be described mathematically with the variable Longitudinal Relaxation Time (T_1) as follows:

$$M_z(t) = M_0(1 - \exp^{-\frac{t}{T_1}}) \tag{1.5}$$

T_2 relaxation always occurs when there is T_1 relaxation and, therefore, without spin-spin coupling M_{xy} would decay to 0 with the same rate as M_z decays to the equilibrium state. Hence, T_2 has to be shorter than T_1, for example, the relaxation times of grey matter are $962ms$ and $101ms$ and for white matter $725ms$ and $85ms$ at $1.5T$. [2]

As it can be seen in equations 1.4 and 1.5 there is another parameter affecting the magnetization. M_0 is the effective magnetization which is available for the MRI signal. M_0 is a proportionality factor including coil sensitivities, field inhomogeneities, the RF amplification chain and other technically related influences. For qMRI however, the most important factor of M_0 is the Proton Density (PD) which is defined as the number of spins per voxel and hence is a physical density. As a consequence of biological tissues mainly composed of hydrogen, MRI has a very high Signal-To-Noise Ratio (SNR) and can achieve excellent soft-tissue contrasts.

The acquisition of volumes is quite sophisticated but in principal a pulse sequence has to be applied to measure the signal in the appropriate way. The sequence is basically a set of gradients and RF pulses for either encoding the image in spatial direction or defining the contrast. The latter can be adjusted by variation of Repetition Time (T_R), Echo Time (T_E) and other parameters like flip angle α. In the case of a SE, T_R is the distance between two consecutive excitation pulses and T_E the time between the excitation and the middle of the echo signal. By varying T_R and T_E the influence or weighting of T_1, T_2 and also PD is adjusted.
T_1-weighted images can be considered as a function of T_R which is chosen in the range of the mean T_1 of the observed tissue in combination with a short T_E. On the contrary, the echo time of T_2-weighted images is chosen in the range of the mean T_2 of the tissue. T_R is very long to achieve longitudinal relaxation which makes the sequence time-consuming. The combination of a long T_R and a short T_E minimizes the effects of T_1 and T_2 and is therefore referred as PD-weighted.
The contrast can be further enhanced when applying an additional inversion or saturation pulse before the regular SE sequence. A typical example is a Fluid-Attenuated Inversion Recovery (FLAIR) sequence which suppresses the signal of fluids and water. This can be achieved by choosing Inversion time (T_I), i.e. the time between the inversion and the excitation pulse, in a way that M_z of the tissues, which should be attenuated, is approximately zero when starting the SE sequence.

1.2 Problems of conventional MRI

The wide range of different adjustable contrasts is definitely a very important feature of MRI because it can be adapted to the examined body region. Nevertheless, the pixel intensity has no direct physical meaning as a result of the dependency of T_R, T_E and other parameters. Thus, the image contrast is mainly due to relative differences of T_1, T_2 and PD between adjacent tissues and the diagnosis relies on the comparison with the surrounding of the interested region. It is therefore often necessary to acquire the same region with different contrast weightings to highlight specific tissues of interest. The necessarity of different image characteristics requires various measurements with different sequences which elongates the overall scan time. A longer acquisition is typically uncomfortable for the patient and leads often to motion artefacts. These artefacts are pronounced in either a misregistration of the different contrasts which is not that crucial for visual inspection or artefacts in the image itself. The latter can depict a problem for the diagnosis because the quality is often significantly decreased as blurring and ghosting can appear.
When considering pediatric radiology additional issues arise in comparison to examinations of adults. First, children feel uncomfortable more easily and often need a sedation during the scan. This minimizes the motion artefacts but the duration should not be expanded for too long due to assessable but nevertheless existing health risks. Second, especially babies with the typically fast developing brain can have very dynamic tissue parameters. Leppert et al. [3] showed an exponential decay of White Matter (WM) tissue T_2 from up to $404ms$ at birth to about $80ms$ for adults. Also the Grey Matter (GM) T_2 decreases exponentially altough not that extensive. Graefe et al. [4] showed a similar behaviour of the longitudinal relaxation time T_1 with a rapid decrease in the first three years of age followed by a weaker decrease. Also here the effect is more pronounced for WM than for GM. In figure 1.2 an example of the relaxation times evolution in the dependance of the age are shown for WM. The exponential decay of the relaxation times is linked to the changes of water content and distribution and the myelination of the developing brain. The latter can be a explanation of the more prominent effect in WM tissue.

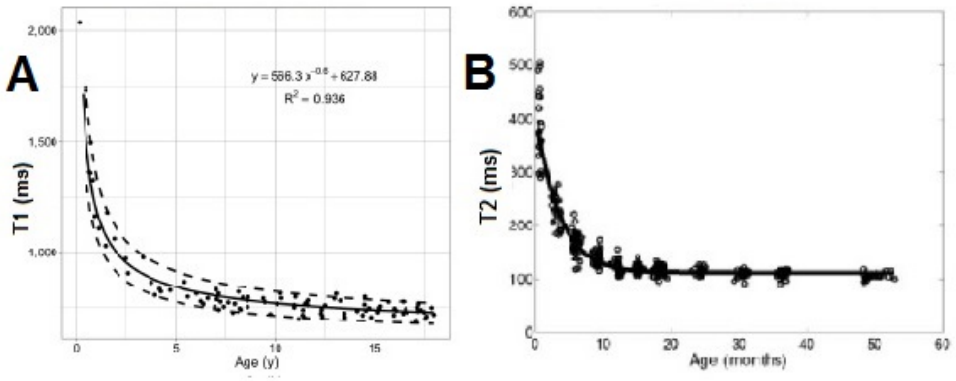

Figure 1.2: Age-related evolution of T_1 (A) and T_2 (B) in white matter tissue, modified from [3] and [4]

Indeed, the relaxation times contribute not directly to the different contrasts like T_1-, T_2- or T_2-FLAIR-weighted, but as a matter of course there is an indirect influence. This means that a fixed configuration of T_R, T_E and eventually T_I results in different image characteristics in dependance of the age. Consequentially, this can imply an inferior contrast between tissues of interest for infants or children. Therefore, the configuration has to be adapted but the dynamic behaviour of the relaxation times complicates the finding of the optimal settings for the patient.

The well-known and highly developed contrast-weighted images provide high anatomical details of the different structures. Nevertheless, the application of segmentation and volume estimation to MRI images extends the potential for the diagnosis. Numerous different methods for the segmentation of the brain in the tissue classes WM, GM and Cerebrospinal Fluid (CSF) were proposed. Typically these methods use multiple acquisitions to create a multi-feature space since one contrast image is often not sufficient to distinguish the brain tissues. In addition it is not sufficient to classify one voxel to a specific tissue type. When a combination of tissues in a voxel is allowed, images can be acquired with a lower resolution because the dependency on the spatial resoultion is minimized.

As mentioned before the intensity in contrast images is not directly linked to the physical

composition of the tissue and dependent on T_R, T_E and T_I. Furthermore the images are influenced by inhomogeneities of the static field B_0 and the transmit and receive field B_1. The pulse profile of the transmitted RF pulses as well as the coil sensitivities and the RF amplification chain settings of the receiving part complicate the measured signal in addition. Naturally the segmentation should only be dependent on the physical properties which makes the classification of tissue or even tissue mixtures for such numerous affected signals complex. [5]

1.3 Quantitative Magnetic Resonance Imaging

Quantitative Magnetic Resonance Imaging (qMRI) includes methods for the absolute quantification of physical parameters, i.e., the relaxation times T_1 and T_2 as well as the PD or the pseudo proton density M_0. Contrary to conventional MRI, the pixel values have a direct physical meaning equal to intrinsic parameters and thus can overcome the above mentioned problems. Since only the direct parameters are shown, the influences of the sequence and deviations between scanners or patients are diminished leading to a more objective comparison and evalution of the examined body parts.

The requirement for more contrast-weighted images can be ordinary fulfilled with the synthesis of contrasts. The reconstruction in the postprocessing, assuming a flip angle of $\alpha = 90°$, is calculated as follows

$$S = PD(1 - exp^{-\frac{T_R}{T_1}})exp^{-\frac{T_E}{T_2}} \tag{1.6}$$

With a virtual application of an inversion pulse for images with FLAIR or Short-Tau Inversion Recovery (STIR) sequences the formula is

$$S = PD(1 - 2 \cdot exp^{-\frac{T_I}{T_1}} + exp^{-\frac{T_R}{T_1}})exp^{-\frac{T_E}{T_2}} \tag{1.7}$$

and for Double Inversion-Recovery (DIR) with two inversion pulses the signal is calculated

$$S = PD(1 - 2 \cdot exp^{-\frac{T_{I1}}{T_1}} + 2 \cdot exp^{-\frac{T_{I2}}{T_1}} - exp^{-\frac{T_R}{T_1}})exp^{-\frac{T_E}{T_2}} \tag{1.8}$$

where T_R, T_E and, where necessary, the inversion time(s) are independent parameters which can be arbitrary chosen. Additionally, α can be varied which would expand the denominator with a term proportional to $cos(\alpha)$ and further increase the number of possibilities. Nevertheless, with the shown equations 1.6-1.8 a wide range of image contrasts can be synthesized. This manual contrast adjustment alters the way MRI is performed because after the quantification of the intrinsic parameters no more sequences have to be acquired. The different image characteristics are synthesized retrospective without additional measurement time. For a dynamic relaxation behaviour the synthesis during postprocessing has the potential to adapt the virtual sequence settings in order to optimize the desired image contrast. [6]

The direct quantification of the physical quantities which are independent of the acquisition strategy and system imperfections [7] simplifies the segmentation and the subsequently volume estimation. This can give insights for certain diseases where the conventionally contrast-weighted images are not sufficient and the detection can be improved. Multiple sclerosis, Alzheimer's, dementia and Parkinson's are associated with global and local brain atrophy with pathological processes like axonal damage, gliosis, inflammation and edema causing the diseases. These symptoms provoke changes in the relaxation behaviour and water content which can be well detected in the quantitative T_1, T_2 and PD maps and easily classified by the segmentation. [2] [5] [7] The importance of this method is elevated since neurodegenerative diseases show an increasing prevalence. Furthermore the volume estimation allows for an objective and reliable intrapatient, e.g. a quantitative progression measure and interpatient, e.g. detection and staging, comparison. [7]

The fundamentals for the quantification of the relaxation times were proposed more than

50 years ago but are considered as the gold-standard methods even today. In chapter 2.2.2 a short summary of the methods is given. However, the excessive scan time of these approaches prohibited an application in clinical routine. Because of the described necessarity for qMRI several methods for a faster quantification have been proposed. Often the required scan time or the background noise hindered a clinical usage. Furthermore the sequentially determination of the parameters can have the drawback of misregistration. To overcome these issues some approaches of simultaneous quantification of T_1, T_2 and PD were introduced.

1.4 Simultaneous Quantification of T_1, T_2, PD and B_1

In 2004 Schmitt et al. [8] introduced a method for the simultaneous quantification of the tissue parameters from the signal of a series of IR - balanced Steady-State Free Precession (bSSFP). The series of acquisitions offers the possibility to reconstruct several images after the inversion pulse and to measure the signal intensity over a time course. With this approach the measurement can be executed in a clinically acceptable time but there is a undesired sensitivity for off-resonant spins. There is also a significant influence of the B_1 inhomogeneity and the resulting spatial flip angle distribution on the quantification accuracy.

When Ma et al. [9] introduced Magnetic Resonance Fingerprinting (MRF) in 2013 a novel paradigm of MRI was presented because the data acquisition, post-processing and visualization are a completely different approach. The basic principle is the assumption that a unique set of tissue parameters results in a unique signal evolution, called fingerprints, using an appropriate acquisition scheme. The method is applicable with a wide range of sequences, e.g. IR-bSSFP because it is sensitive to T_1, T_2 and off-resonance. The fingerprints are acquired with a continuous variation of sequence parameters, like T_R, T_E or the flip angle in a pseudorandom manner. A pattern recognition algorithm is used to find the best match of the fingerprints in a previously constructed dictionary. The dictionary contains signal evolutions of all foreseeable combinations of the parameters

calculated with the Bloch equations and hence the used parameters can be retrieved for a fingerprint if a matched entry is found. The MRF acquisition can be done in a clinically acceptable time but nevertheless the approach has some critical drawbacks. First, there is a lack of proof for the uniqueness of the measured signal in the dictionary regarding the parameters. Second, the computation time and storage requirement of the dictionary expands exponentially with the number of fitting parameters. In consequence of the huge database also the reliance and computation time of the pattern recognition can have limitations. Machine learning, especially neural networks, have the potential to manage the computational issues but there is still need for further development. [10]

A method overcoming the mentioned difficulties is Quantification of Relaxation Times and Proton Density by Multiecho Acquisition of a Saturation-Recovery using Turbo-Spin-Echo Readout (QRAPMASTER) proposed by Warntjes et al. in 2008. [6] The sequence can be acquired in a clinically acceptable scan time combined with postprocessing time less than one minute. In addition also the B_1 field is measured in order to use a correction for the effects of deviations in the flip angle distribution. The entire technique including the acquisition, quantification, image synthesis and segmentation is referred to as "SyMRI". SyMRI has regulatory approval in several countries and is commercially distributed by SyntheticMR, Linköping, Sweden, across various platforms, e.g. Siemens Healthcare, Erlangen, Germany. On Siemens scanners the QRAPMASTER sequence is also referred to Multi-Dynamic, Multi-Echo (MDME).
Before the introduction of QRAPMASTER the same research group introduced the method Quantification of Relaxation Times and Proton Density by Twin-Echo Saturation-Recovery Turbo-Field-Echo (QRAPTEST). Similar to the above described IR-bSSFP or the Look-Locker (LL) method it is also a Gradient Echo (GRE) but the QRAPTEST uses a saturation pulse of 90° instead of an inversion pulse. Nevertheless, the calculation of the T_1 decay is similar to the LL method which is [11]

$$\frac{1}{T_1} = \frac{1}{T_1^*} + \frac{ln(cos(\alpha))}{T_R} \tag{1.9}$$

where T_1^* is the estimated relaxation time from $-M_0$ to the steady-state magnetization M_0^*.

T_1 can also be determined by the ratio of the unsaturated (M_0) and saturated magnetization in the case of a sufficient delay time as required for the LL

$$T_1 = T_1^* \frac{M_0}{M_0^*} \tag{1.10}$$

Equation 1.10 shows that the LL method is independent of the actual flip angle. However, the QRAPTEST approach omits the time-consuming delay between subsequent cycles which makes the adequate determination of the steady-state magnetization M_0^* impossible since there is no full relaxation to thermal equilibrium. Therefore, the reliability of the T_1 quantification is dependent on the accuracy of the flip angles which requires a B_1 field correction with a multiplication factor. This factor is derived from the intensity at cycle time T_C before the subsequent saturation pulse and the intensity after the saturation pulse. T_2^* can be calculated with the two point approach from the two intensities I_1 and I_2 of the shots with the echo times T_{E1} and T_{E2}, respectively, according to equation 1.11

$$T_2^* = \frac{T_{E2} - T_{E1}}{ln(I_1/I_2)} \tag{1.11}$$

PD is determined with the measured intensity at echo time T_E with flip angle α, the calculated values of T_1 and the obtained apparant relaxation times T_1^* and T_2^*. Furthermore numerous scaling factors including the consideration of local receive coil sensitivity, temperature, voxel volume and many more are included in the calculation.

Despite the validation in the research setting the method has it limitations and issues which are substantially improved by QRAPMASTER. [12] [13]

1.4.1 Sequence

The first modification from the QRAPTEST to the QRAPMASTER is the usage of a spin-echo instead of a gradient echo. The SE in contrast to GRE is insensitive to suscep-

tibility effects caused by the B_0 inhomogeneities. This makes it possible to determine the relaxation time T_2 instead of the shorter appearant relaxation time T_2^* (cf. eq. 1.3). A longer relaxation time diminishes image blurring at longer echo times and has therefore a better estimation at tissue interfaces. The second improvement is the elimination of the excitation flip angle limitation which is for the QRAPTEST method in the range $4 - 8°$. The limitation arises from the fact that a larger flip angle not only increases the SNR but also the correction factor for the T_1 quantification. The noise in the observed T_1^* amplified by the square of the correction factor requires a smaller flip angle in order to obtain accurate results. [12] On the contrary, the QRAPMASTER sequence uses a long repetition time between subsequent acquisitions which removes the limitation of the flip angle because T_1 is not computed on the basis of T_1^* and therefore no correction factor is needed. Furthermore a saturation pulse with a nominal value of 120° instead of 90° is applied. [6]

The quantification measurement is basically executed following the sequence diagram as shown in figure 1.3. The basic block consists of two phases which are repeated over the whole measurement, namely the saturation and the acquisition block. In the first phase, a slice-selective saturation pulse with flip angle θ is applied. The saturation pulse leads to the starting position of the longitudinal relaxation curve which is a function of the B_1 field. Hence, the measurement of the local B_1 field is possible by the determination of the flip angle deviations which can be used for corrections. The second phase includes the acquisition by a slice-selective spin echo. The acquisition consists of a 90° excitation pulse followed by multiple 180° refocusing pulses to measure multiple echoes in order to be able to extract the transversal relaxation time T_2. The usage of more refocusing pulses than reconstructed echoes causes an acceleration of the acquisition by Turbo Spin Echo (TSE), e.g. 10 refocusing pulses for two echoes results in a turbo factor of 5. A further acceleration can be achieved using an echo-planar imaging technique to acquire several k-space lines per SE. The saturation is applied to a slice m, whereas the acquisition is executed on slice n. By introducing a shift between m and n, the desired delay times can

be set in order to obtain the longitudinal relaxation time T_1. Practically this is achieved by shifting the order of the slices with respect to each other, e.g. when measuring 27 slices with 4 delay times, the shift is a multiple of 1, 4, 12, and 26 of the acquisition time per sequence block. The number of echoes in the acquisition block and the number of scans with different delay times can be freely chosen to accomodate the dynamic ranges of T_2 and T_1, respectively.

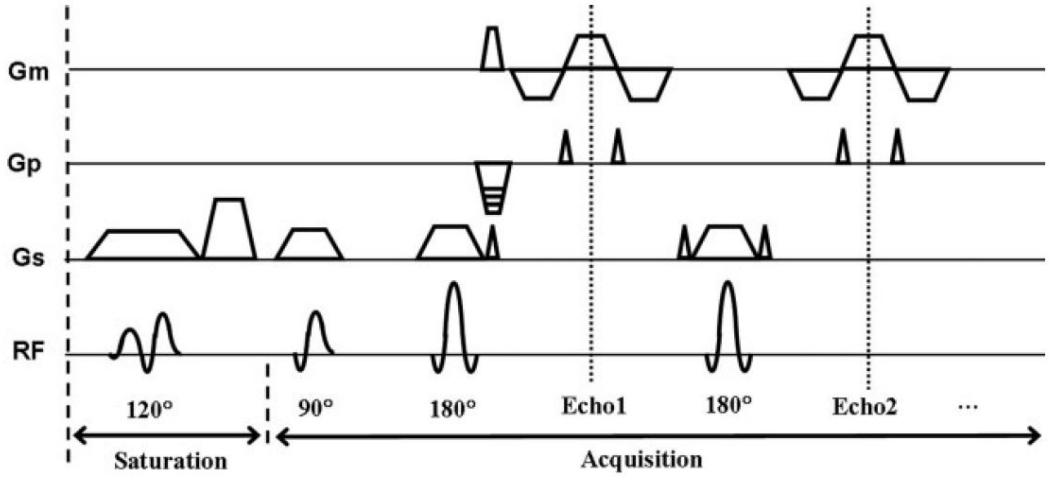

Figure 1.3: Schematic sequence diagram of a single QRAPMASTER block with measurement (Gm), phase-encoding (Gp), slice-selection (Gs) gradients and the RF pulse amplitudes. The saturation in the first phase is applied to slice m and the acquisition, which can be accelerated with further 180° pulses, is performed on slice n. [6]

The long repetition time between subsequent acquisitions in combination with short scan time can be achieved with a multislice sequence. One issue of this sequence type is slice cross-talk which can be avoided by an interleaved slice order. However, the interleaved scheme would lead to a varying error per slice which results in a quantification error of T_1. In order to get a similar error for each slice a linear slice order of the quantification scan is chosen. Due to the constant saturation of flowing blood the sequence is inherently black-blood. The inflow effects may lead to flow artefacts, mostly in the first slices of the neck. To avoid these artefacts, a regional saturation pulse located at the neck of the patient can be added.

In general the method is signal efficient and the sequence is effective with a duty cycle of the receivers up to approximately 50% to 60% of total scan time. This is the basis for an accurate quantification of the absolute parameters within a clinically acceptable time. [6] [14]

1.4.2 Postprocessing

The quantification of the parameters with the QRAPMASTER approach has two main advantages. First, the relaxation times T_1 and T_2 are measured independently. Hence, the error propagation between the two parameters is prevented. Second, the simultaneous acquisition of the parameters results in perfectly registered maps. Nevertheless, the motion artefacts can generate problems which are pronounced as blurring or ghosting in the image. Also if there are only artefacts during one part of the acquisition, inherently all of the quantitative maps and therefore also the synthetic images are influenced and have an inferior quality.

Pulse profile simulation

A correction is necessary since the sequence uses slice-selective RF pulses which typically have a non-ideal behaviour causing inaccuracies of the measurements. Furthermore the observed saturation flip angle θ_{eff} must be reliable related to the effective excitation flip angle α_{eff} to obtain accurate results. Therefore, a spin system simulation of the whole sequence was performed.
Warntjes et al. [6] obtained the amplitude envelopes of the different pulses, including the saturation, excitation and refocusing pulse, from the scanner software (1.5T Achieva, Philips Medical Systems, Best, The Netherlands). In the simulation these envelopes are approximated with a set of RF block pulses with the length of $1\mu s$ unit time. With this small unit time near-zero changes of the magnetization per time step are achieved which is mandatory for the validity of the Bloch equations. The effects of the individual RF block

pulses and the simultaneously applied gradient fields are calculated on the spin system and the simulation of the whole scan is done for each individual spin. The 120° saturation pulse rotates the spins around the y-axis and the resulting transverse magentization is spoiled with a z-gradient. During the following delay, a longitudinal relaxation with T_1 of $1000ms$ is simulated. Subsequent the spin-echo aquisition with the 90° excitation pulse (around the y-axis) and a series of 180° refocusing pulses (around the x-axis) is performed. In order to get accurate results also the gradient winders and rewinders are simulated and by integrating the x-component of the transversal magnetization, the macroscopic signal intensity can be calculated. A complementary measurement of the longitudinal magnetization after a saturation, excitation and refocusing pulse was held in order to validate the simulation. Therefore, the RF pulses were applied to an agar phantom (T_1 of $380ms$) with gradient spoiling and acquisition perpendicular to the slice to determine the effective flip angle as a function of the slice.

In figure 1.4 the flip angle distribution of the 120° saturation, 90° excitation and 180° refocusing pulse in dependence of the normalized slice distance is shown. The dashed lines indicate the ideal rectangular RF pulse profiles with the simulation curves (solid lines) achieving the ideal flip angle only at resonance in the center of the slice. Neglecting the central peak of the refocusing pulse which is not resolved in the measurement, the simulated and measured data have a good agreement. Furthermore the cross-talk between slices can be investigated with the RF pulse simulations. The non-zero effective flip angles outside the intended slice thickness can be quantified with 7% of the total signal. The usage of a spacing between the slices of 10% (of slice thickness) which is the minimum recommendation according to [15] reduces the contribution to 3%.

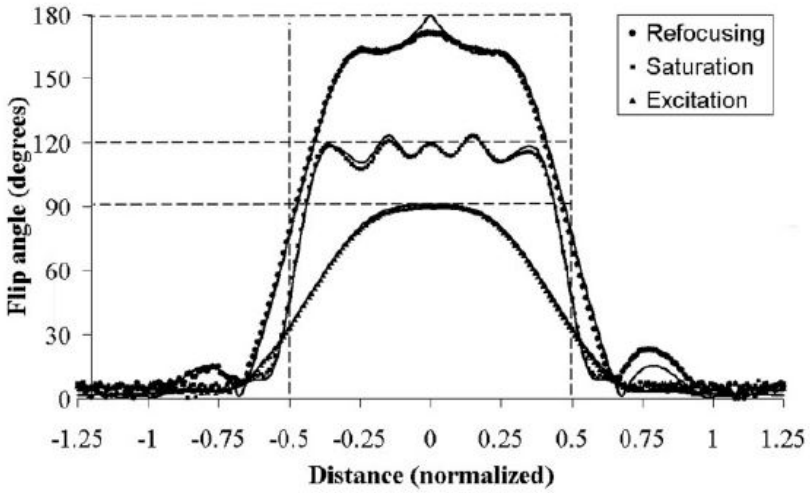

Figure 1.4: The 90° excitation flip angle α, the 120° saturation flip angle θ and the 180° refocusing pulse as function of normalized slice thickness. The dashed lines indicate ideal slice-selective pulses, the solid lines are calculated based on the Bloch simulations and the points indicate the measured data points, from [6].

The simulation of an ideal slice profile of the saturation pulse results in a magnetization as function of the delay time corresponding to the dashed line of figure 1.5. This longitudinal relaxation starts ideally at $cos(120°) = -0.5$ and converges to 1 for an infinite time after the saturation pulse. However, when simulating each point of the non-ideal RF pulse profile and integrating the transverse magnetization over the complete slice distance, the spin-echo readout begins at -0.26 when there is no delay time. With a delay of $4000ms$ after saturation a value of 0.899 for the first and 0.954 for the second spin-echo readout can be approached. The average intensity is quantified with 0.932 corresponding to an effective excitation flip angle of $\alpha_{eff} = asin(0.932) = 68.7°$. In order to improve the the T_2 quantification which uses typically a relatively low number of readouts, the first and second echo have to be corrected to get computationally affected by an effective excitation angle of 68.7° at nominal B_1 field. This can be achieved by multiplications with the factors 1.036 and 0.977 for the intensities of the first and second echo, respectively. The difference of M_{T0}, the intensity after a saturation pulse, and M_{TR}, the measured intensity at T_R just before the subsequent saturation pulse, is only due to the effects of the saturation and

the subsequent spoiling. The effective saturation flip angle can therefore be calculated according to:

$$\theta_{eff} = acos(M_{T0}/M_{TR}) = acos(-0.26/0.932) = 106.2^{\circ} \tag{1.12}$$

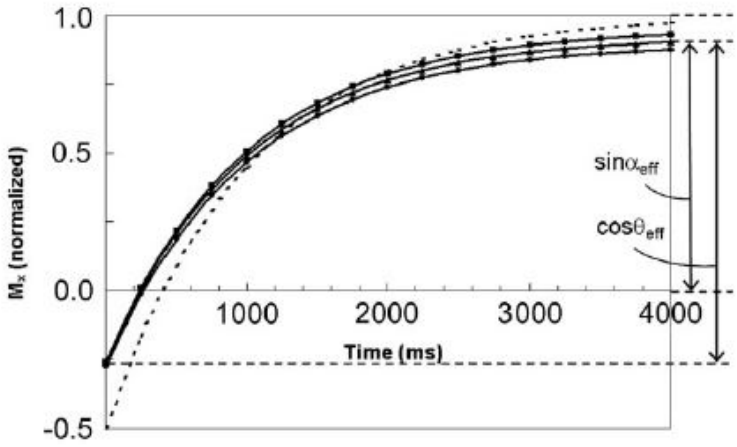

Figure 1.5: Signal intensity of an ideal saturation recovery curve (dotted line) with a 120° saturation pulse at time 0 and T_1 of the phantom $1000ms$. The solid lines show the intensities using imperfect RF pulses with a multiecho SE acquired at different times. The intensity of the first echo is lower and of the second higher than the average of the first 10 echoes. The effective flip angles can be calculated from the shown arrows, from [6]

Different B_1 fields are considered for the simulation due to the variation across a patient and thus the according pulse amplitude variation. In figure 1.6 the effective saturation and excitation pulse angles are plotted as function of the respective nominal angles. The third subplot combines the two correlations in order to map the effective excitation angle α_{eff} as a function of the effective saturation angle θ_{eff}. Observing the diagram the following empirical approximation can be introduced

$$\alpha_{eff} = (\theta_{eff} - 34.5^{\circ}) < 69^{\circ} \tag{1.13}$$

valid for θ_{eff} in the range $80^{\circ} - 115^{\circ}$ which corresponds to a field inhomogeneity between

70% and 110%.

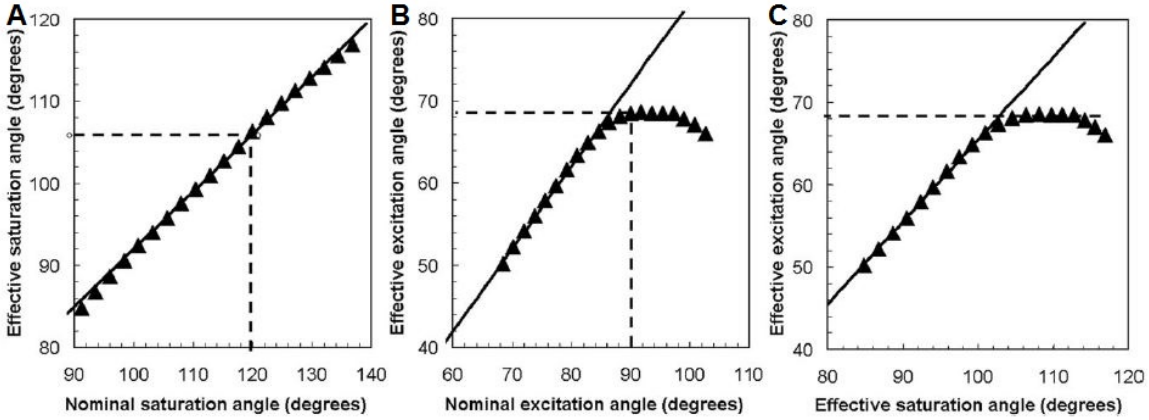

Figure 1.6: Simulation of different B_1 field strengths with a varying intendend saturation and excitation amplitude. The relation of nominal flip angles to the observed effective flip angles for the saturation (A) and excitation pulse (B) with the dashed lines indicating the intended B_1 field. (C) Relation of effective saturation flip angle to effective excitation flip anlge, from [6]

Fitting algorithm

The post-processing algorithm is based on a pixel-wise least square fit of the signals (S) in each of the images which are typically 8 in a number. The formula for the quantification of T_1, T_2, PD and B_1 is

$$S = A \cdot PD \cdot exp^{-\frac{T_E}{T_2}} \cdot \frac{1 - [1 - cos(B_1\theta)]exp^{-\frac{T_I}{T_1}} - cos(B_1\theta)exp^{-\frac{T_R}{T_1}}}{1 - cos(B_1\alpha)cos(B_1\theta)exp^{-\frac{T_R}{T_1}}} \tag{1.14}$$

where A is overall intensity scaling factor with the coefficients explained later (eq. 1.16). The measurement and relation of the effective excitation flip angle α and the effective saturation flip angle θ is explained above. As it can be seen in equation 1.14 a monoexponential decay is assumed for either longitudinal and transversal relaxation.

Since an iterative fitting for 4 unknown parameters is linked to a high computational effort and therefore is very time-consuming Warntjes et al. introduced a more analytical solution. At first the transversal relaxation time T_2 is determined from all images

weighted by the absolute intensities with a least-square fit. When only two echoes are applied the usage of the two point approach (see eq. 1.11) is possible. With the knowledge of the intensity at a specific echo time and T_2 the expected intensity for $T_E = 0$ can be further calculated. This value is projected onto a single T_1 curve. From this curve the effective saturation angle θ_{eff} can be extracted and the effective excitation angle is calculated following equation 1.13. The resulting B_1 field is smoothed with a median filter of $10mm$ because the field is assumed to not change rapidly over the volume. From the T_1 curve and the additional conditiion $M_{T0} = M_{TR}cos(\theta_{eff})$ (cf. eq. 1.12) the longitudinal relaxation T_1 and the pseudo proton density M_0 can be retrieved with a least-square fit of the following formula

$$M = M_0 \frac{1 - (1 - cos(\theta_{eff})exp^{-\frac{T_I}{T_1}} - cos(\theta_{eff})exp^{-\frac{T_R}{T_1}}}{1 - cos(\alpha_{eff})cos(\theta_{eff})exp^{-\frac{T_R}{T_1}}} \tag{1.15}$$

where M is the magnetization at a specific delay time T_I and echo-time zero. [6] Finally, PD can be calculated by scaling M_0 with a number of factors as follows:

$$PD = C_{coil}C_{load}C_{vol}C_{pix}C_{temp}C_{arb}\frac{M_0}{sin(\alpha_{eff})\alpha_{eff}} \tag{1.16}$$

C_{coil} is a scaling factor for the local sensitivity of the applied receive coil, C_{load} accounts for load differences of the quadrature body coil using the RF pulse amplitude settings (unconstrained load factor). C_{vol} scales the volume to the reference voxel volume of $1mm^3$, C_{pix} is a factor for the relation image pixel intensity to absolute MR intensity (like rescale slope and intercept) and C_{temp} takes temperature differences into consideration and is 1 for normal body temperature. C_{arb} is introduced to display more convenient values for the PD, e.g. to match the PD of free water to a value of 1000. [12]

1.4.3 Segmentation

West et al. [5] proposed an approach for whole brain segmentation in White Matter (WM), Grey Matter (GM) and Cerebrospinal Fluid (CSF) and subsequent volume estimation

which is performed with a lookup-grid and therefore very time-efficient. This lookup-grid is a 3-dimensional space with the coordinates R_1, R_2 (relaxation rates; inverse of relaxation times) and PD.

The construction of the model is based on a numerical Bloch simulator including the RF pulses, gradients and timings of the QRAPMASTER sequence in order to calculate the magnetization of the different echo and inversion time combinations with additional noise. The pure tissue characterisitcs of WM, GM and CSF are based on the values from [6] and result in a magnetization vector $\mathbf{E}_{tissue}$. In figure 1.7 the 95% prediction ellipses (of the 10000 times repeated Monte Carlo simulations) for the pure tissue clusters and 50% combinations of tissues are shown. The three contour lines of each cluster are contributed to different SNR where the highest SNR are related to the smallest ellipses, respectively.

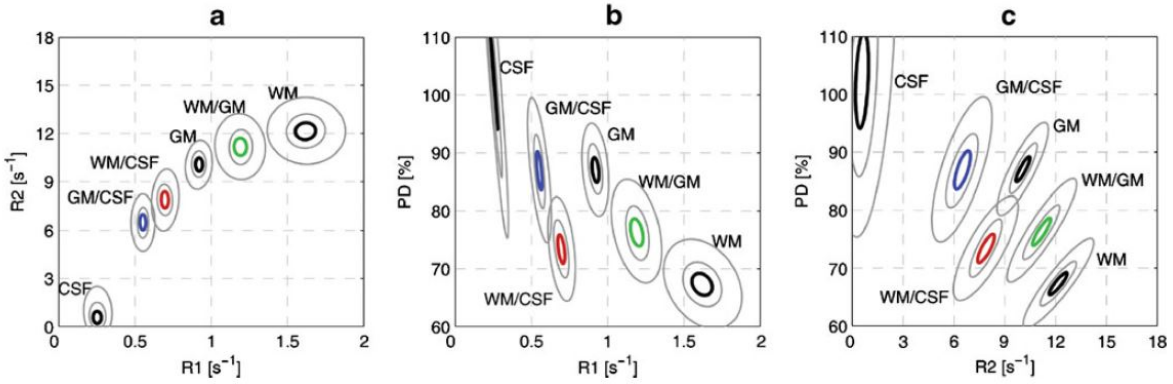

Figure 1.7: Lookup grid on R1-R2 (a), R1-PD (b) and R2-PD (c) projections for pure tissues WM, GM and CSF and 50% mixtures. The ellipses show 95% prediction for simulations with SNR 40 (smalles ellipses), 20 and 10, from [5]

The partial volume effect is a major source of error at heterogenous locations which is very likely in the brain. A higher spatial resolution can overcome this issue. [7] Alternatively, as mentioned above, the mixture of tissues in a single voxel can also reduce the effects. Therefore, the model is simulated for partial volumes with incremental steps of 0.1% from 0% to 100%. The magnetization state of tissue mixtures are calculated

$$\mathbf{E}_{combined} = \alpha \cdot PD_{tissue1} \cdot \mathbf{E}_{tissue1} + (1 - \alpha) \cdot PD_{tissue2} \cdot \mathbf{E}_{tissue2} \tag{1.17}$$

where α is the volume fraction of the first tissue. The same fitting algorithm is used in order to quantify T_1, T_2 and PD from $\mathbf{E}_{combined}$. Subsequently, with these 3000 multivariate tissue clusters a lookup-grid in the R_1-R_2-PD space can be defined. These curved bands are shown in figure 1.8 presenting the significance of the joint 95% prediction ellipses. The transitions are also presented in the absence of noise with diamonds plotted at every 20% tissue fraction. The orthognal lines are indicating the corresponding gridlines of the lookup-grid.

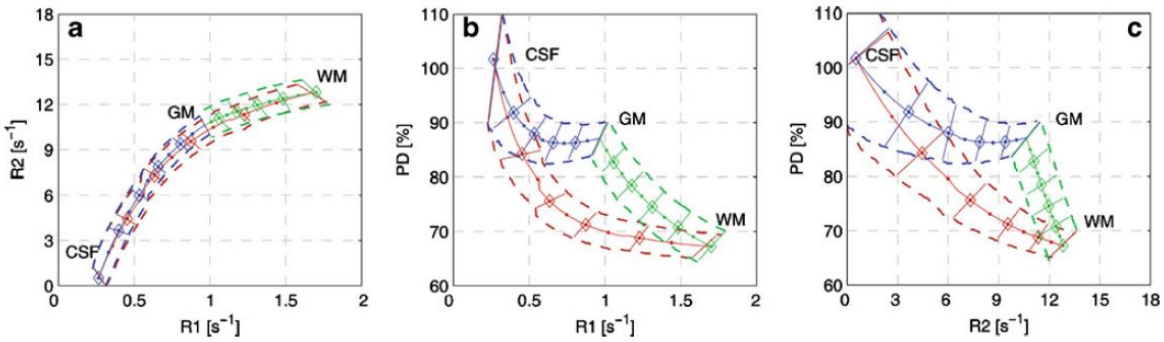

Figure 1.8: Joining the 95% prediction ellipses of the simulated partial-volume clusters results in curved bands (dashed lines). The solid lines are the transitions in the absence of noise (diamonds at 20% changes) with the orthogonal lines indicating the lookup-grid for tissue classification in R1-R2 (a), R1-PD (b) and R2-PD planes (c), from [5]

The brain tissue is segmented into WM, GM and CSF as follows. In the case of qMRI values within the 95% prediction ellipses of of pure tissues, the tissue fraction is 100%. Since the appearance of the remaining 2997 clusters is close and often overlapping, the quantified voxel can be mapped to the nearest cluster with the corresponding tissue fraction. In the case of a quantification outside the 95% prediction bands in the R_1-R_2-PD space, the voxel is considered undefined and classified as fourth type named Non-WM/GM/CSF (NoN). The occurrence of the same coordinates for clusters with different tissue fractions due to noise leads to an ambiguity. In this case a spatial kernel with 7x7 neighbouring voxels is applied. The decision of the partial volume transition is made by the two most occurring tissue types inside this kernel. An example slice of a segmentation is presented

in figure 1.9.

The total volume of WM, GM, CSF and NoN is a summation of the voxel volume multiplied with the corresponding volume fractions. Furthermore clinical relevant parameters like the Intracranial Volume (ICV), as the sum of all 4 tissues, and the Brain Parenchym Volume (BPV), which is the sum of WM, GM and NoN, can be calculated. The outer bounds of the ICV is defined where the PD is 50% because it is assumed as the middle between CSF (100%) and the skull (0%). The BPV is normalized by the ICV, named as Brain Parenchym Fraction (BPF), because the ICV has a high interpatient variance.

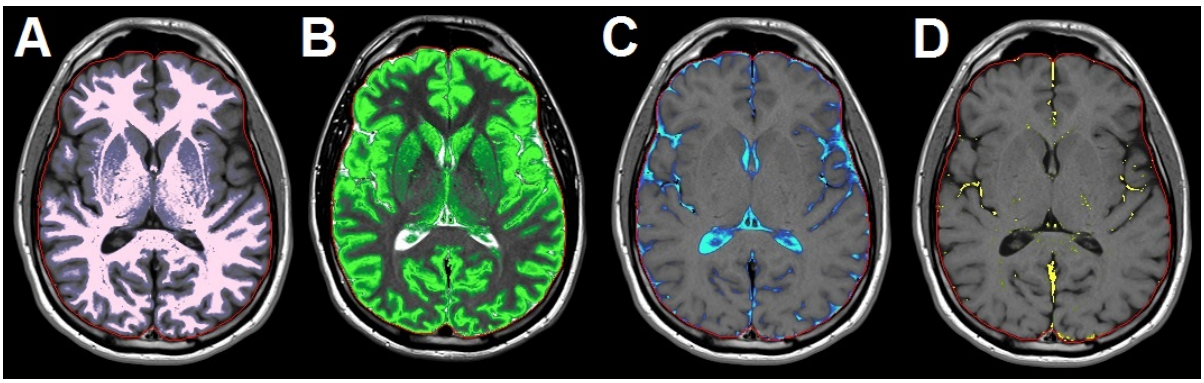

Figure 1.9: Segmentation example of one slice with the red line indicating the boundary of ICV with classification of WM, GM, CSF and NoN. The intensity is proportional to the fraction of the tissue with the sum for each pixel equal to 100%.

1.4.4 Myelin estimation

Magnetization Transfer

The basis for the MRI signal, e.g. the hydrogen atoms, appear in different compounds: free water, hydration layer and macromolecules, like proteins and lipids. In the latter compound hydrogen nuclei have a highly restricted motion and therefore short T_2 values. The free bulk water and the hydration layer exist in a state of rapid chemical equilibrium where the nuclei rotate rapidly resulting in long T_1 and T_2 values. Hence this close relationship between the hydration layer and free water are summarized to the free pool

and the macromolecular compound is defined as the bound pool. The immobile proteins of the bound pool cannot be detected directly by MRI because the transverse relaxation is too short, e.g., smaller than $1ms$. After an excitation pulse spatial encoding gradients have to be applied and the fast relaxation causes a nearly complete signal decay before the acquisition. On the contrary, the mobile protons have sufficient long T_2 to be measured directly. [16] Naturally magnetization is exchanged between the free and bound pool to obtain an equilibrium state and therefore the normally observed relaxations of the free pool also includes effects of the bound pool recovery which means if one pool is perturbated the changes occur in both pools. [17]

In figure 1.10 the spectral lines of the free and restricted pool are shown. While the free pool with longer T_2 has a narrow spectral line $(10 - 100Hz)$ the macromolecular pool with short T_2 has subsequently a broad spectral line $(10 - 50kHz)$. The broad absorption lineshape of the immobile protons makes this pools' magnitudes more sensitive to off-resonance RF pulses than magnitudes of the free pool. This opens the possibility to selectively excite the bound pool and thus create a magnetization difference between the two pools. Through magnetization exchange processes the spin states of the free pool are influenced by the spin states of the nuclei in the restricted pool. [16] The cross relaxation shortens the apparent longitudinal magnetization compared to T_1 of the MRI visible free pool since it takes less time to reach the smaller equilibrium magnetization. Hence the indirect influence of the macromolecules is visible in MRI by suppression of the signal, known as Magnetization Transfer (MT). [17]

While the effects and contrast mechanisms of MT are well understood at the tissue level the nature of interaction and exchange processes are not that clear on cellular and molecular level. The spin exchange which causes decreased longitudinal magnetization available for imaging by transferring bound pool saturation to the free pool is supposed to occur via dipole-dipole interactions or via chemical exchange. The dipolar interaction is understood as cross relaxation through space between the bound nuclei and the protons in the hydration layer. The chemical exchange also contributes to the transfer process but experiments with isotopically substituted protons and pH effects concluded that the

influence is a less significant factor. Nevertheless, the following shown model and the algebra cannot distinguish dipolar interaction and chemical exchange. [16] [17]

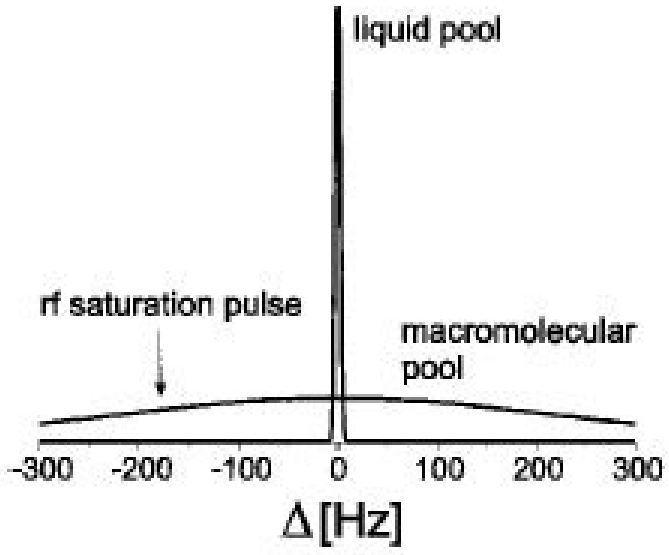

Figure 1.10: Absorption lineshapes of macromolecular and liquid protons. Only the macromolecular pool with immobile protons can be saturated with the marked off-resonance RF pulse. [16]

Henkelmann et al. [18] have introduced a description for the magnetization transfer of a two pool model as shown in figure 1.11. The free pool F and the bound pool B both consist of a longitudinal magnetization M_z^f and M_z^b, respectively, (white) and transverse and saturated magnetization (grey). R_f and R_b are the longitudinal relaxation rates, e.g. $R_i = 1/T_{1,i}$ with $i = f, b$. The number of spins in the free pool M_0^f is normalized to one, the number of spins in the bound pool is M_0^b and the exchange rate between the two pools is R. The exchange rate from free to bound pool is $R \cdot M_0^b$ and $R \cdot M_0^f$ vice versa.

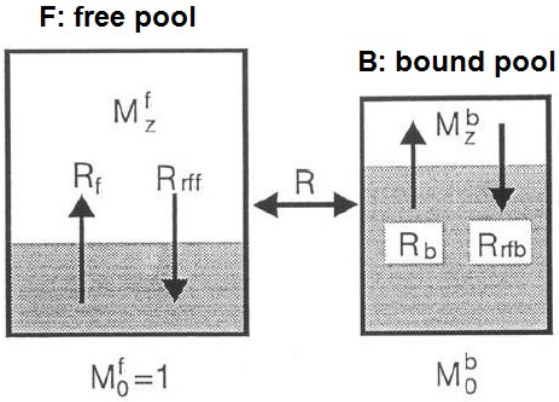

Figure 1.11: Two pool model with longitudinal magnetizations (white) and spins which are not aligned longitudinally. All variables are defined in the text and used in the Bloch equations, modified from [18]

This model can be mathematically expressed with the following coupled Bloch equations in a system of following differential equations

$$\frac{dM_x^{f,b}}{dt} = -\frac{M_x^{f,b}}{T_{2f,b}} - \Delta\omega M_y^{f,b} \tag{1.18}$$

$$\frac{dM_y^{f,b}}{dt} = -\frac{M_y^{f,b}}{T_{2f,b}} + \Delta\omega M_x^{f,b} - \omega_1 M_z^{f,b} \tag{1.19}$$

$$\frac{dM_z^f}{dt} = R_f(M_0^f - M_z^f) - RM_0^b M_z^f + RM_0^f M_z^b + \omega_1 M_y^f \tag{1.20}$$

$$\frac{dM_z^b}{dt} = R_b(M_0^b - M_z^b) + RM_0^b M_z^f - RM_0^f M_z^b + \omega_1 M_y^b \tag{1.21}$$

where ω_1 is the angular frequency of precession induced by the off-resonance RF pulse and $\Delta\omega$ is the frequency offset of the B_1 field.
When comparing to the Bloch equations without magnetization transfer effects (equations 1.22-1.24) the only difference can be found in the differential equation for M_z.

$$\frac{dM_x}{dt} = -\frac{M_x}{T_2} - \Delta\omega M_y \tag{1.22}$$

$$\frac{dM_y}{dt} = -\frac{M_y}{T_2} + \Delta\omega M_x - \omega_1 M_z \tag{1.23}$$

$$\frac{dM_z}{dt} = R_1(M_0 - M_z) + \omega_1 M_y \tag{1.24}$$

Hence magnetization exchange reduces significantly the available magnetization for imaging and thus reduces also the T_1 and T_2 of the visible free pool. [7] [16]

Myelin model based on qMRI

Axons are coated piecewise in myelin sheaths with nodes of Ranvier in between. The speed of the signal transmission is increased by saltatory conduction which means that the impulses are jumping from node to node. So myelin can be considered as accelerator of the signal transmission in the nervous system and therefore of particular pathological interest for clinics. Myelin main components are a wide range of proteins and lipids. Eng et al. [19] are considering lipid bilayers as an effective macromolecular structure for magnetization transfer. Therefore, the usage of the MT effects described in a model is an approach for a reliable myelin quantification. Another established method for the estimation of myelin is multicomponent T_2 relaxometry. This can be achieved since the water inside the myelin sheaths has a shorter T_2 than the intra- and extracellular water component. [20] A fast determination of the multiexponential relaxation is for example possible with a combination of SPGR and bSSFP but the short T_2 component of myelin water ($< 15ms$) makes this approach very sensitive for imperfections and hence limits the clinical usage. [21]
However, the fitting algorithm of the QRAPMASTER sequence assumes a monoexponential decay for both, longitudinal and transversal relaxation, which is often not applicable for in vivo microscopic environments. Instead of determining multiexponential factors only the dominant relaxation behaviour is quantified. [14] In addition the direct measure-

ment of the fast myelin water relaxation cannot be resolved. Therefore, a model exists in order to identify myelin indirectly by the MT effect causing a shift on the visible medium-time relaxation component and the decrease in the observed PD. [22]
This model for the determination of myelin present in a specific tissue using qMRI was introduced by Warntjes et al. [23]

The basis consists of 4 compartments with partial volumes ranging from 0% to 100% with a combined value of 100% for each acquisition voxel. The compartments myelin V_{MY}, cellular V_{CL}, free water V_{FW} and excess parenchymal water partial volume V_{EPW} have their own parameters R_1, R_2 and PD. The effective quantified parameters of an acquisition voxel represent a combination of the partial volumes with the respective quantitative values and the magnetization exchange between the compartments.
V_{MY} includes myelin water and sheaths with a very fast relaxation, e.g. T_2 of $13ms$, due to the closely packing around the axons. The macromolecules not related to myelin present besides intra- and extracellular water result in a medium-time relaxation behaviour for V_{CL}. V_{FW} consists of CSF with very long relaxation times and due to the phyiscal separation from the parenchym no magnetization exchange with other compartments is assumed. V_{EPW} has the same qMRI values as V_{FW} but since there is no distinction between excess parenchymal water partial volume and the parenchymal water of V_{CL}, the exchange rate $k_{VEPW-VCL}$ between these two compartments is infinitely high. V_{EPW} is introduced to be able to detect edemas, i.e. a cellular swelling.
Levesque and Pike [24] introduced a four-pool model which yields quantitative insights into the relaxation behaviour and MT effects of white matter. This model was approximized by merging myelin water and semi-solids to V_{MY} and intra- and extracellular water and non-myelin semi-solids to V_{CL}. In figure 1.12 (A) an acquisition voxel of normal brain parenchyma is presented as a mixture of V_{MY} (higher in WM, lower in GM) and V_{CL} (lower in WM, higher in GM) with the magnetization exchange rate $k_{VMY-VCL}$. Figure 1.12 (B) shows the border of the brain as a mixture of parenchyma and CSF (V_{FW}) and (C) is a model for myelin loss resulting in a relative decrease of V_{MY} and a subsequent increase of V_{CL}.

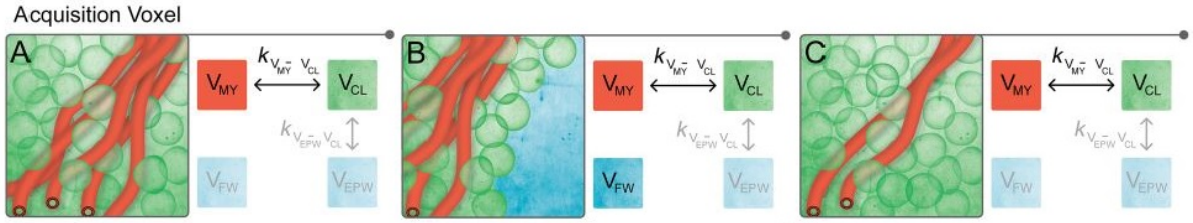

Figure 1.12: A single acquisition voxel presenting the compartmental exchange system with different contributions of the four compartments. (A) normal brain parenchyma with myelin and cellular partial volume and the magnetization exchange rate. (B) A free water partial volume without magnetization exchange contributes additionally at the interface to CSF. (C) Pathological brain parenchyma with decrease of myelin partial volume and hence increase of cellular partial volume ot maintain 100% tissue, modified from [23]

A system of coupled Bloch equations with 150 identical magnetization elements, each of them with the same partial volume distribution, normalized magnetization vectors for each compartment and equidistantly spread over the slice direction, is numerically simulated. The evolution of a magnetization element in small time steps ($t = 1\mu s$) is calculated according to:

$$M_{i,n+1} = R_{RF} * R_{GR} * R_{R1} * R_{R2} * M_{i,n} \tag{1.25}$$

R_{RF} is the rotation matrix with flip angle over the x- or y-axis equal to $2\pi\gamma B_1 t$ with B_1 the amplitude of the RF pulse at that interval and similar R_{GR} as rotation matrix of the applied slice-selective gradients around the z-axis calculated by $2\pi\gamma G d_i t$ with G the gradient strength and d_i the distance from the slice center. R_{R1} and R_{R2} are the relaxation matrices for the longitudinal and transversal relaxation acting only on the M_z and M_{xy} components, respectively. Besides the exponential decays the matrices also include the combined forward and backward exchange rate between V_{MY} and V_{CL}, defined as $K_{MC} = exp(-tk_{VMY-VCL})$, and different scaling factors required to quantify the relative volumes of PD in each compartment. The macroscopic observable magnetization for a specific T_E and T_I is calculated by summation over all elements with the total proton density in each

partial volume and the transversal magnetization component according to:

$$I_{TE,TD} = \sum_i (V_{MY} * PD_{MY} * M_{xy,MY} + V_{CL} * PD_{CL} * M_{xy,CL} + V_{FW} * PD_{FW} * M_{xy,FW} + V_{EPW} * PD_{EPW} * M_{xy,EPW}) \tag{1.26}$$

By fixing the model parameters of the free and excess parenchymal water partial volume, $R_{1,FW} = R_{1,EPW} = 0.24s^{-1}$, $R_{2,FW} = R_{2,EPW} = 0.87s^{-1}$, $PD_{FW} = PD_{EPW} = 100\%$ as literature values from [6], the relaxation rate of the myelin partial volume $R_{2,MY} = 77s^{-1}$ according to [24] and the exchange rate $k_{VEPW-VCL} = \infty$, only 6 model parameters have to be optimized.

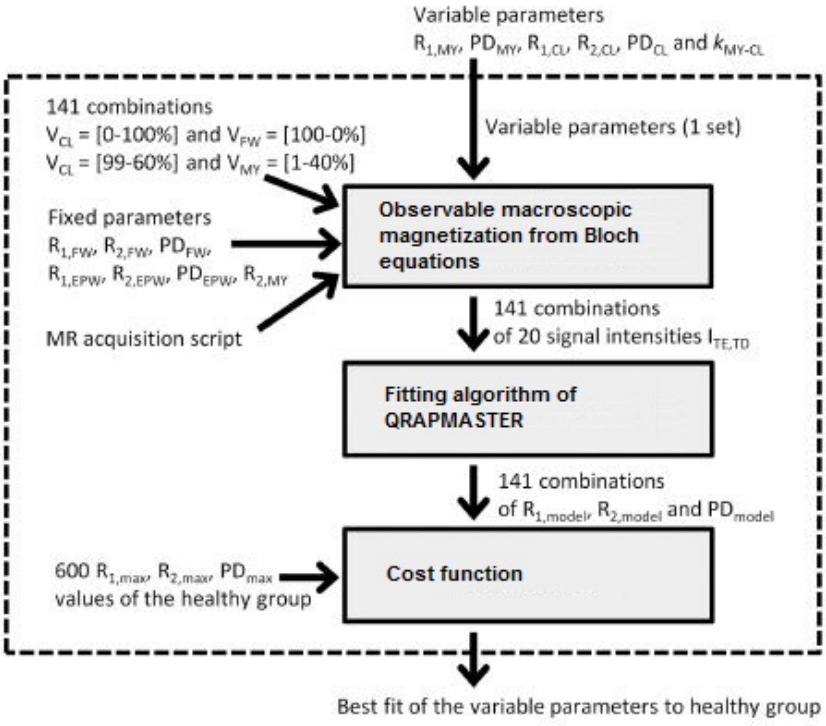

Figure 1.13: Scheme for the optimization of the variable model parameters with explanation of the procedere in the text, modified from [23]

$R_{1,MY}$, PD_{MY}, $R_{1,CL}$, $R_{2,CL}$, PD_{CL} and k_{MY-CL} are summarized as variable parameters in the flow chart (figure 1.13) for the optimization of the model parameters. In the first step, a random set of the variable parameters under the constraints $R_{1,FW} < R_{1,CL} <$

$R_{1,MY}$ and $R_{2,FW} < R_{2,CL} < R_{2,MY}$ is used to simulate 141 combinations where each combination consists of the signal intensities at the different T_E and T_I, which are also used for the acquisition of a healthy control group. The 141 combinations are the result of varying the partial volumes V_{CL} from 0% to 100% with V_{FW} from 100% to 0% and V_{CL} from 99% to 40% with V_{MY} from 1% to 40% in 1% steps and under the condition to have a total volume of 100% and the restriction for V_{MY} since no higher values are reasonable. The QRAPMASTER fitting algorithm is used to obtain the relaxation rates and proton density of the model for each combination. The 2D histograms of the acquired data (fig. 1.14, A and B) consist of 200 bins in each direction. The maximum values for each bin in every direction with the corresponding coordinates of the other 2 directions are recorded in order to obtain 600 $R_{1,max}$, $R_{2,max}$ and PD_{max} defining a characteristic data structure of the control group. These 600 values are reduced to the 141 closest combinations of the model values in order to quantify the similarity between model and acquired data with a cost function. The procedure is repeated with individually varying one variable parameter in order to minimize the residual. In the end, the best fit of the variable parameters to the healthy group is determined which are stated in [23].

From the optimized model a lookup-grid is constructed in the R_1-R_2-PD space where the quantified parameters of an acquisition can be projected to obtain the distribution of the 4 partial volumes ranging from 0% to 100%. This grid is shown in figure 1.14 (C and D) with the black lines as transitions between 100% free water, 100% cellular and 40% myelin partial volume. In figure 1.15 the model calculation of the partial volumes is presented on the central brain slice of the healthy control group.

Furthermore the calculation of the total aqueous content is possible by summation of the 4 partial volumes with their respective proton density ($\sum V_i * PD_i$, with $i = MY$, CL, FW and EPW). The remaining volume is the non-aqueous content attributed to macromolecules.

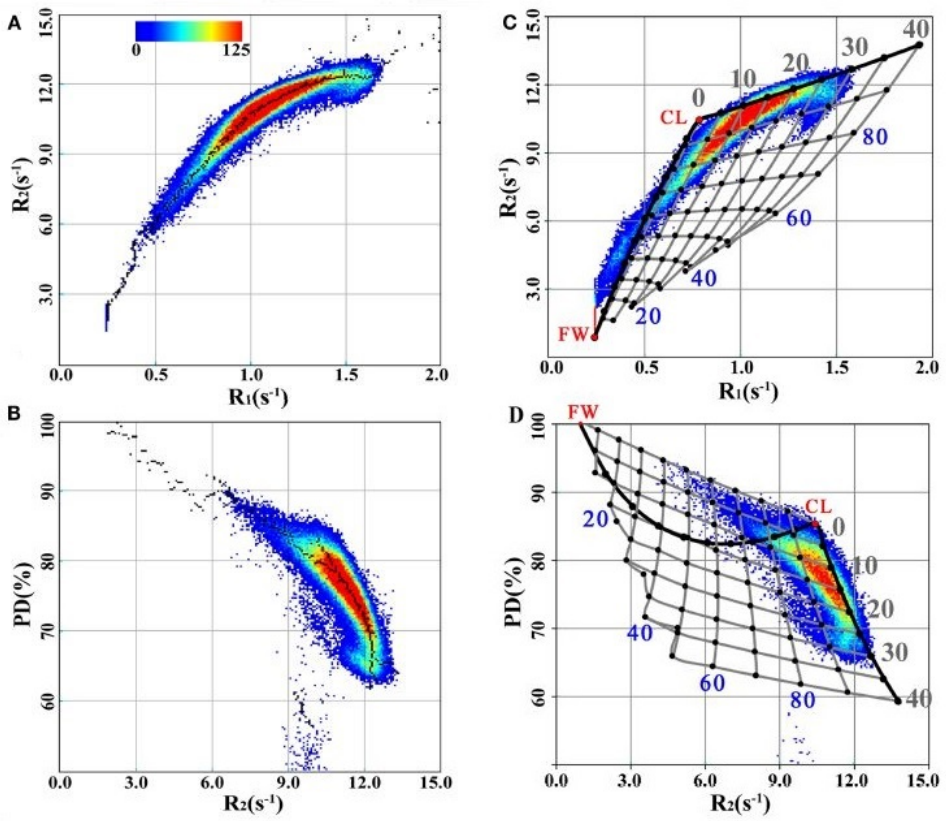

Figure 1.14: 2D histograms of R1, R2 and PD of the spatially normalized brain images with the colour indicating the number of voxels for each coordinate. (A) and (B) are from the control group with the black dots placed at the maximum of each direction used for the optimization. (C) and (D) are from the MS patients with the transitions from 100%V_{FW} to 100%V_{CL} to 40%V_{MY} using the optimized model parameters. Grey lines are the lookup-grid, modified from [23]

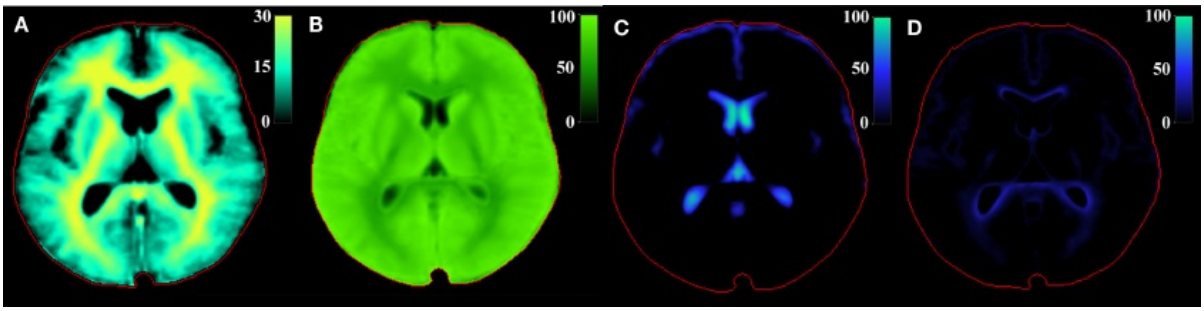

Figure 1.15: Example model calculation (A) V_{MY}, (B) V_{CL}, (C) V_{FW} and (D) V_{EPW} with the red line as the border of the ICV, modified from [23]

1.5 Objective

The objective of this thesis is to evaluate the clinical benefit for the Division of Pediatric Radiology where the QRAPMASTER sequence is available. A major goal of development for MRI acquisitions is the decrease of the overall examination time which is even more crucial for children or infants. Therefore, the possibility for the replacement of conventional acquired sequences, e.g. T_2-weighted, by synthetic contrast images is a question. In order to get an objective assessment, the conventional and synthetic images should be technically compared with the Structural Similarity Index (SSIM). Since the contrast between WM and GM is an important indicator the contrast difference of the two approaches should be also quantified. In addition the assessment of radiologists is desired to get insights to subjective similarity between the conventional and synthetic images.
The quantification of the SyMRI workflow should be compared to gold standard methods like inversion-recovery or multi-echo measurements. The effect of MT on the dfferent aquisition strategies should be investigated in order to explain differences in the contrast. The image synthesis could be one benefit because of the scan time shortening if the quality is acceptable compared to conventional images. Furthermore the additional features of the SyMRI should be investigated for the clinical relevance to define areas of specific interests where the QRAPMASTER sequence could be used to bring a benefit in the clinical routine.

2 Methods

2.1 Preliminary evaluation of SSIM

Experiments were held in order to get a principal understanding of the sensitivity and variation range of the Structural Similarity Index (SSIM). The measurements were executed with a phantom to overcome the influence of motion artefacts arising from long acquisition times. A pomegranate was chosen because the SSIM depends besides the luminescence and contrast also on the structure.
The measurements were constructed to examine the effect of changes in the scanning parameters on the SSIM. These changes are based on the small differences between the sequences which were scanned on the patients as part of the clinical routine. The intention was to investigate the SSIM of images

- which were identically acquired,
- with different acquisition matrices and the effect of downsampling,
- with different phase resolutions,
- with intended motion and the motion corrected stacks.

To extract the influence of only one parameter there were base parameter settings which were held constant and chosen closely to the standard of care brain MRI.

2.1.1 Structural Similarity Index

The SSIM was introduced by Wang et al. [25] to achieve an objective method for assessing the similarity between two images with respect to human visual perception. Therefore, the metric includes terms for luminance, contrast and structure because the idea is to quantify image degradation as change in structural information. The SSIM is a full reference metric where the quality of an image is based on an initial reference image. [26] The index for an image is computed by averaging the quantity of each pixel which is

$$SSIM(\mathbf{x}, \mathbf{y}) = [l(\mathbf{x}, \mathbf{y})]^{\alpha} \cdot [c(\mathbf{x}, \mathbf{y})]^{\beta} \cdot [s(\mathbf{x}, \mathbf{y})]^{\gamma} \tag{2.1}$$

with the terms for luminance (eq. 2.2), contrast (eq. 2.3) and structure (eq. 2.4) as follows:

$$l(\mathbf{x}, \mathbf{y}) = \frac{2\mu_x\mu_y + C_1}{\mu_x^2 + \mu_y^2 + C_1} \tag{2.2}$$

$$c(\mathbf{x}, \mathbf{y}) = \frac{2\sigma_x\sigma_y + C_2}{\sigma_x^2 + \sigma_y^2 + C_2} \tag{2.3}$$

$$s(\mathbf{x}, \mathbf{y}) = \frac{\sigma_{xy} + C_3}{\sigma_x\sigma_y + C_3} \tag{2.4}$$

The local mean intensity μ_x and standard deviations σ_x and σ_{xy} are calculated with an 11x11 circular-symmetric Gaussian weighting kernel $\mathbf{w} = \{w_1, w_2..., w_N\}$ with standard deviation of 1.5 samples and normalized to unit sum according to

$$\mu_x = \sum_{i=1}^{N} w_i x_i \tag{2.5}$$

$$\sigma_x^2 = \sum_{i=1}^{N} w_i (x_i - \mu_x)^2 \tag{2.6}$$

$$\sigma_{xy} = \sum_{i=1}^{N} w_i (x_i - \mu_x)(y_i - \mu_y) \tag{2.7}$$

The constants C_i are introduced in order to avoid instability when the denominators are

close to zero and chosen

$$C_1 = (K_1 L)^2 \quad C_2 = (K_2 L)^2 \quad C_3 = C_2/2 \tag{2.8}$$

with $K_1 = 0.01$, $K_2 = 0.03$ and L as the dynamic range of the images. When choosing the exponents α, β and γ to one (cf. eq. 2.1) the SSIM can be calculated in the specific form:

$$SSIM(\mathbf{x}, \mathbf{y}) = \frac{(2\mu_x\mu_y + C_1)(\sigma_{xy} + C_2)}{(\mu_x^2 + \mu_y^2 + C_1)(\sigma_x^2 + \sigma_y^2 + C_2)} \tag{2.9}$$

2.1.2 Acquisition

The sequences (T_2-weighted 2D-TSE in transversal orientation) were scanned on a 3T MRI scanner (MAGNETOM Vida, Siemens Healthcare, Erlangen, Germany) on the XA20 software platform using a 64-channel receive-only head/neck coil. The timing was set to T_E $95ms$ and T_R $5090ms$ with a turbo factor of 17, a flip angle of 150° and a bandwidth of $191Hz/Px$. The Field Of View (FoV) was set to $210mm$ and with a base resolution of 512 the pixel spacing resulted in $0.41mm$ x $0.41mm$. The phase resolution was 70% and 27 slices were acquired with a thickness of $5mm$ and a distance factor of 10%.
The acquisition was repeated with the same settings and two sets with an acquisition matrix of 320x224 (reconstructed to $0.66mm$ x $0.66mm$) were measured. Two stacks were acquired with a phase resolution of 75% resulting in the acquisition matrices 512x384 and 320x240. The original measurement (base 512 and phase resolution 70%) was repeated twice after two intended motions of the pomegranate.

2.1.3 Processing

A script was implemented in MATLAB R2019b (The MathWorks Inc., Natick, USA) to calculate the SSIM slicewise for 17 slices because in the upper and lower region no signal from the pomegranate was measured. Furthermore a masking was implemented in

order to compare the images only in the region where a signal in the reference image was obtained. The image stacks were compared as stated in table 2.1. For experiment 2, the reference image was downsampled with a bicubic interpolation. The two volumes acquired after the intended motion were coregistered with an affine registration in the Statistical Parametric Mapping toolbox SPM12 (UCL Queen Square Institute of Neurology, London, UK).

The following parameters were chosen: $sep = [5, 2, 1]$, $params = [0, 0, 0, 0, 0, 1, 1, 1, 0, 0, 0]$, $interp = 4$, $tol = [0.02, 0.02, 0.1, 0.001, 0.001, 0.005, 0.01, 0.01, 0.05, 0.001, 0.001, 0.005]$ and *cost_fun* = *nmi* (Normalized Mutual information). For a detailed explanation of the SPM12 toolbox and the parameters please refer to [27].

Table 2.1: SSIM experiments where 512 and 320 are the base resolution, the numberation of the measurements in brackets, *PR75* refers to a phase resolution of 75% and *MOTION1/MOTION2* are acquired after the first or second intended motion.

Experiment no.	Reference Image	Image
1 (identical)	512 (1)	512 (2)
	320 (1)	320 (2)
2 (downsampling)	512 (1)	320 (1)
	512 (1)	320 (2)
	512 (2)	320 (1)
	512 (2)	320 (2)
3 (phase res.)	512 (1)	512, PR75
	512 (2)	512, PR75
	320 (1)	320, PR75
	320 (2)	320, PR75
4 (original) (intended motion)	512 (1)	512, MOTION1
	512 (1)	512, MOTION2
	512 (2)	512, MOTION1
	512 (2)	512, MOTION2
4 (coregistered)	512 (1)	512, MOTION1
	512 (1)	512, MOTION2
	512 (2)	512, MOTION1
	512 (2)	512, MOTION2

2.2 Phantom measurements

The intention of the following measurements was to survey the QRAPMASTER accuracy of the relaxation time and proton density determination and the influence of MT effects on the contrast at different acquisition methods, eg. SE and TSE). As a consequence of the necessity for a lot of different sequences the overall examination time was in the range of three hours. The probability and intensity of artefacts are usually increased for this duration due to more motion as a result of subjects being impatient. In order to eliminate this influence, measurements were taken on phantoms.

2.2.1 Phantom preparation

For the measurements eight different phantoms were created, two with distilled water only and six with Electran® Agarose DNA Grade (VWR International, Radnor, USA). The agarose powder was mixed into distilled water at room temperature and subsequently heated in a microwave until the composition became transparent. In order to get in the range of biological relevant relaxation times, e.g. WM and GM, the distilled water and the agarose mixtures were doped with Gadobutrol (Gadovist®, Bayer, Leverkusen, Germany) and Mangan(II)-chlorid Tetrahydrat (Sigma-Aldrich, St. Louis, USA). The agarose relaxivities were determined in an additional measurement and the relaxivities of the doping agents and formulas for calculation of concentrations were taken from [28]. Due to the agarose relaxivity there were some restrictions which made it impossible to mix phantoms with identical relaxation behaviour. The composition of the phantoms with the desired relaxation times is stated in table 2.2.

Table 2.2: The composition and the respective intended relaxation times of the mixed phantoms.

No.	Agarose $[mass\%]$	Gadovist $[mM]$	$MnCl_2$ $[mM]$	T_1 $[ms]$	T_2 $[ms]$
1	4	0.136	0.065	700	25
2	4	0.129	0	960	29
3	2	0.163	0.052	700	45
4	2	0.159	0	960	58
5	1	0.201	0.022	700	80
6	1	0.145	0	960	97
7	0	0.125	0.103	700	80
8	0	0.101	0.051	960	100

2.2.2 Quantitative Magnetic Resonance Imaging

The intrinsic tissue parameters quantified by the QRAPMASTER (or MDME) sequence and the SyMRI postprocessing were compared to the determination by common methods. The following described methods include the current gold-standard quantification sequences for T_1, i.e., Inversion-Recovery (IR) with different T_I and T_2, i.e., Spin Echo (SE) with different T_E. These methods also include a quantification of M_0 which is direct proportional to PD with the gain of the receiver system. [7]

Determination of T_1

The accurate quantification of the Longitudinal Relaxation Time (T_1) is the IR sequence. In figure 2.1 the mono-exponential recovery following equation 2.10 in relation to the inversion time is plotted. The signal is normalized by the longitudinal magnetization M_0 and starts at -1 immediately after the inversion pulse. Another method for the determination is the Saturation-Recovery (SR) sequence with the condition $f_{inv} = 1$ and therefore $S(0) = 0$. Because the SR method has the drawbacks of a half dynamic range and a lower Signal-To-Noise Ratio (SNR) compared to the IR, it is not commonly used.

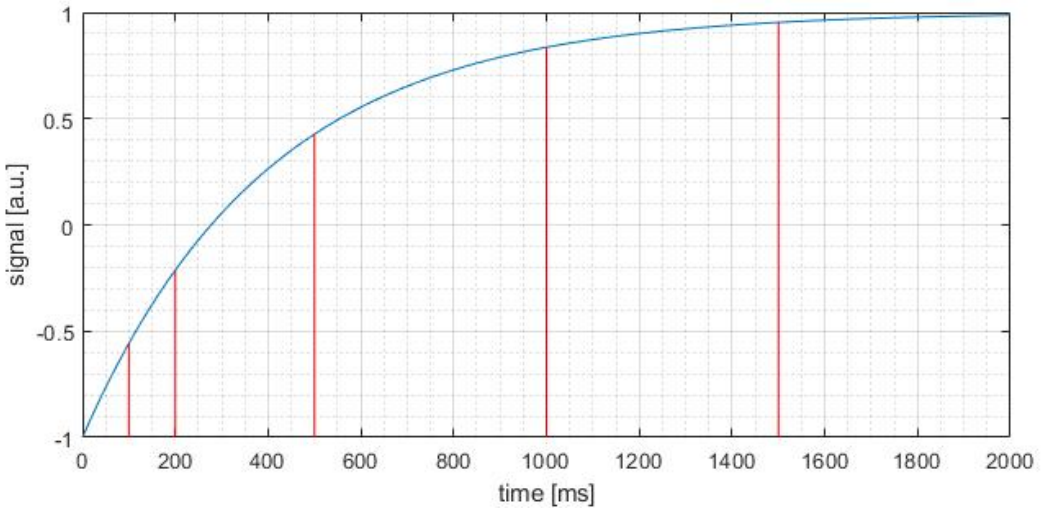

Figure 2.1: Normalized signal of IR-SE in relation to the inversion time acquired at different T_I.

$$S_{IR}(T_I) = M_0(1 - f_{inv} \cdot \exp^{-\frac{T_I}{T_1}}) \tag{2.10}$$

For the IR method the condition $T_R > 5 \cdot T_{1,max}$ has to be fulfilled to assure full relaxation, i.e., all spins are in equilibrium before the following excitation. $T_{1,max}$ is the longest appearing longitudinal relaxation time in the tissue and is typically in the range $1-2s$. It should be considered that some tissues like Cerebrospinal Fluid (CSF) show a longitudinal relaxation up to $4s$ and hence a longer T_R is required. To achieve a high SNR the echo time should be chosen as short as possible. The images have to be acquired with identical T_R and T_E but different inversion times T_I in order to approximate the T_1 value of every pixel. The need of a long T_R in combination with multiple acquisitions with different T_I is the reason for the long scan time with this method for T_1 quantification. The parameters T_1, M_0 and f_{inv} are computed pixel-wise with an appropriate fitting routine which can be simplified by assuming a perfect inversion, i.e., $f_{inv} = 2$.

Variable Flip Angle method

Another possibility for the quantification of T_1 is the Variable Flip Angle (VFA) approach which is clearly faster than the IR method and relatively accurate. [29] The information of the Driven Equilibrium Single Pulse Observation of T_1 (DESPOT1) method established by Homer and Beevers [30] and Deoni et al. [31] is derived from spoiling the transverse magnetization after each excitation pulse. With the formula (eq. 2.11) of the signal evolution for this sequence, called Spoiled Gradient Echo (SPGR), it is possible to extract T_1 when collecting images over a range of flip angles α with constant T_R. The very short repetition time in the range of ms and the sensitivity to T_1 for a wide range of flip angles are the the reasons for the rapid acquisition and high measurement precision, respectively. By representing the signal intensity S_{SPGR} (eq. 2.11) in a linear form as in equation 2.12 the computational effort can be reduced to a linear regression which makes the postprocessing very efficient.

$$S_{SPGR}(\alpha) = M_0 \cdot sin(\alpha) \frac{1 - \exp^{-\frac{T_R}{T_1}}}{1 - \exp^{-\frac{T_R}{T_1}} cos(\alpha)} \tag{2.11}$$

$$\frac{S_{SPGR}}{sin(\alpha)} = \exp^{-\frac{T_R}{T_1}} \frac{S_{SPGR}}{tan(\alpha)} + M_0(1 - \exp^{-\frac{T_R}{T_1}}) \tag{2.12}$$

The DESPOT1 data can either be fitted from multiple or, for decreasing the acquisition time, just from two flip angles. Deoni et al. [31] showed that there is an analytical equation for two ideal flip angles which achieve an accurate fit. The two flip angles α are calculated with equation 2.13, where $f = 0.71$ and $E_1 = \exp^{-\frac{T_R}{T_1}}$.

$$\alpha = cos^{-1}\left(\frac{f^2 \pm (1 - E_1^2\sqrt{1 - f^2})}{1 - E_1^2(1 - f^2)}\right) \tag{2.13}$$

The limitation of the DESPOT1 method is that one does not know the relaxation time

a prior which would be beneficial for computing the ideal flip angles. Furthermore small flip angles yield small signals and therefore also a bad SNR.

The T_1 mapping with the VFA method is very sensitive to inhomogeneities of the RF field B_1 which are caused by induced RF eddy and displacement currents in a loaded coil. To reduce the inaccuracy of the quantification it is necessary to include an additional B_1-mapping for calibrating the nominal flip angle to its actual value. The Double Angle Method (DAM) introduced by Stollberger & Wach [32] is an approach to determine the active component of the B_1 field with an SE measurement. From the spin echo signal equation it is obvious that there are various parameters like T_R, T_E, excitation and refocusing angles, spin density, system constants, coil sensitivity and the relaxation of the tissue affecting the signal. The ratio of two consecutive measurements with identical scan parameters except varying excitation flip angle α is assumed to be independent on all of the residual influences. This assumption is only valid when respecting the condition $T_R > 5 \cdot T_{1,max}$ for a full longitudinal relaxation similar to the above mentioned T_1 quantification. The actual flip angle distribution can be calculated with equation 2.14 where the intensity I_1 is measured after an excitation with α_1, I_2 with α_2 and the nominal excitation flip angles are proportional, i.e. $\alpha_2 = 2\alpha_1$.

$$\alpha(\mathbf{x}) = arccos \frac{I_2(\mathbf{x})}{2I_1(\mathbf{x})} \tag{2.14}$$

α is proportional to B_{1+} and therefore the field distribution can be obtained from the determined flip angle distribution. The linear proportionality is an approximation when using slice selective pulses but it was shown that the deviations can be neglected up to 140°. Therefore, the DAM is often acquired with the nominal excitation flip angles of 60° and 120°.

Determination of T_2

The principle of the Transversal Relaxation Time (T_2) quantification is based on the signal equation of the SE. In figure 2.2 the mono-exponential decay following equation 2.15 in relation to the echo time normalized by M_0 is plotted. When applying an excitation pulse with a flip angle of 90° in the equilibrium state the complete longitudinal magnetization M_0 is tipped into the transversal plane. The idea is to measure the refocused signal with different values of Echo Time (T_E). Analogue to the T_1 determination the repetition time must be kept constant along all acquisitions and also has to fulfill the condition $T_R > 5 \cdot T_{1,max}$.

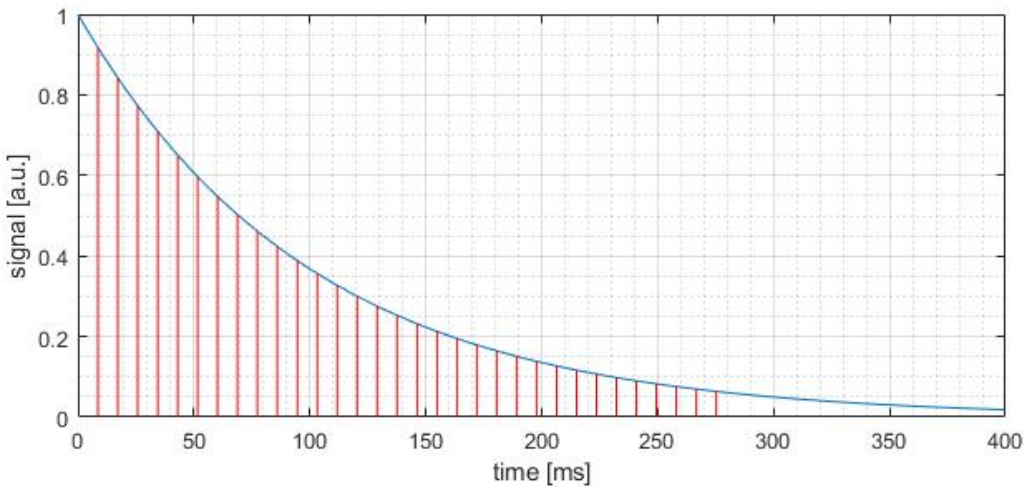

Figure 2.2: Normalized signal of Multi-SE with different T_E sampling points plotted.

$$S_{SE}(T_E) = M_0 \cdot \exp^{-\frac{T_E}{T_2}} \tag{2.15}$$

There are basically two different sequences to get the data of the exponential decay for quantifying T_2: several single spin-echo, i.e., SE and multi spin-echo, i.e., MSE. [33] While the SE sequence is designed to refocus the magnetization after a 90°-excitation pulse only once with a 180°-pulse, the MSE sequence applies multiple refocusing pulses which makes

it possible to measure the whole decay within one T_R. However, the acquisition duration of the SE sequence is proportional to T_R and also the number of different T_E and therefore in the range of the IR for T_1 quantification. The advantage of the shorter measurement time for the MSE method comes along with the drawback of a systematic error caused by stimulated echoes. The stimulated echoes are generated when more than two RF pulses with flip angle $\alpha \neq 180°$ are applied. In theory the MSE with perfect 90°- and 180°-pulses would overcome this issue because the magnetization stays in the transversal plane. Due to imperfections in the scanner hardware, magnetic field and flip angle variations cause the transversal magnetization distribution to be rotated into a new elliptical transversal and a longitudinal magnetization. The new transversal part can be rephased which is the reason for the stimulated echoes after the third RF pulse. To minimize the systematic error the MSE fitting routine is typically computed without the first echo since this is the only one unaffected by stimulated echoes and thus deviant from the mono-exponential decay. The contribution of stimulated echoes on the residual echoes leads to an overestimation up to 30% but could be substantially reduced by a closed-form solution. [34] Despite the fact that the MSE method is inaccurate it is often used as reference measurement for in-vivo T_2 determination due to the time reduction.

2.2.3 Acquisition

The measurements were taken on a 1.5T MRI scanner (MAGNETOM Sola, Siemens Healthcare, Erlangen, Germany) on the XA20 software platform using a 20-channel receive-only head/neck coil.
At first, a MDME sequence with the same parameters as for the patients in clinical routine (see tab. 2.3) was examined.
The 2D-IR sequences acquired the five center slices (each slice $5mm$, gap 10%) with T_R $6000ms$, T_E $8.4ms$ and seven T_Is, i.e., 50, 100, 250, 500, 1000, $1500ms$ and $2400ms$. The pixel spacing was set to $1.41mm$ x $1.41mm$ (base resolution of 128) and the bandwidth to $249Hz/Px$. The relatively short T_R was chosen because eq. 2.10 was fulfilled with the

assumption that relaxation times of the phantoms were $< 1s$.

The second approach to calculate the longitudinal relaxation was a set of 3D-GREs with 12 different flip angles from 1° to 23°, equally spaced by 2°. 16 slices (thickness $5mm$) per slab were acquired by setting T_R $7.7ms$, T_E $3.73ms$ and bandwidth $250Hz/Px$ with FoV $180mm$, base resolution 128, interpolation on and pixel spacing $0.70mm$ x $0.70mm$. For the determination of the imperfect flip angle distribution in-plane the DAM was applied. The flip angles of the single-slice 2D-SE were 60° and 120°, T_R $10000ms$ and T_E $8.9ms$. The base resolution was set to 64 and therefore the pixel spacing was $2.81mm$ x $2.81mm$ because the B_1-field was assumed to not change rapidly over the volume.

The 2D multiecho sequence settings were 9 slices (thickness $5mm$, gap 10%), bandwidth $250Hz/Px$, T_R $3000ms$ and 32 T_E, equally spaced from $8.6ms$ to $275.2ms$. A base resolution of 128 and onset interpolation results in the pixel spacing of $0.70mm$ x $0.70mm$. For comparison multiple single echo SE sequences were acquired with 9 slices ($5mm$ thickness, 10% gap), T_R $3000ms$, pixel spacing $1.41mm$ x $1.41mm$, bandwidth $250Hz/Px$ at 20 different echo times equally distributed from $8.4ms$ to $168ms$.

The last quantitative experiment consisted of two almost equivalent 2D-GRE sequences: one with an onset MTC pulse (frequency offset from water resonance $1.2kHz$, pulse duration $9.984ms$, and nominal flip angle 500°) and one without. The other parameters were T_R $85ms$, T_E $3.84ms$ and flip angle 30°, five slices with thickness $5mm$ and a gap of 10%, bandwidth $250Hz/Px$, FoV 180mm, base resolution 128, interpolation on and pixel spacing $0.70mm$ x $0.70mm$.

In order to evaluate the contrast differences further acquisition were held. The first experiment consists of 3 different two-dimensional T_2-weighted sequences: two TSE with a turbo factor of 17 in an interleaved multi-slice mode (27 and 5 slices) and one single-slice SE. All of the three sequences were acquired with T_R $5000ms$, T_E $92ms$, excitation flip angle 90°, refocusing angle 150°, $5mm$ slices, pixel spacing $1.41mm$ x $1.41mm$ and bandwidth $250Hz/Px$.

The T_1-weighted sequences were acquired with T_R $550ms$, T_E $8.9ms$, excitation flip angle

90°, refocusing angle 180°, 5mm slices and pixel spacing 1.41mm x 1.41mm. The SE sequence had a bandwidth of 250Hz/Px and the TSE with a turbo factor of three had 219Hz/Px.

2.2.4 Processing

The MDME data was processed with the syngo.via (Siemens Healthcare, Erlangen, Germany) Plugin SyMRI 11.2 (SyntheticMR, Linköping, Sweden). A script was implemented in MATLAB R2019b (The MathWorks Inc., Natick, USA) for the fitting of the quantitative parameters and the evaluation of the regions of interest. Therefore, the function *lsqcurvefit* with a Levenberg-Marquardt optimization algorithm was applied for a simultaneous quantification of the MDME data with equation 1.14, T_1 fitting according to equations 2.10 (IR method), respectively 2.12 (variable flip angle approach) and T_2 fitting with equation 2.15.
The Magnetization Transfer Ratio (MTR) was calculated with

$$MTR = \frac{M_0 - M_{SAT}}{M_0} \tag{2.16}$$

where M_0 was the unperturbed signal and M_{SAT} was the obtained reduced signal with an off-resonance RF pulse.

2.3 In vivo measurements

The patient data was aquired as part of the clinical routine at the Division of Pediatric Radiology. The retrospective data evaluation was approved by the Regional Ethics Committee of the Medical University Graz (EK-Nr 33-618 ex 20/21).

2.3.1 Subjects

During the considered study period, from March to June 2021, the data from 60 patients, 35 males and 25 females, were evaluated. The age of the subjects ranged from 3 month to 18 years, with a mean age of 9.82 years. The diagnostic questions included abscesses, cephalea, pre- and postoperative states as well as follow-ups of medullablastoms, mental retardation, microcephalus and checkup of shunts.

2.3.2 Aquisition

The measurements were taken on a $1.5T$ MRI scanner (MAGNETOM Sola, Siemens Healthcare, Erlangen, Germany) on the XA20 software platform using a 20-channel receive-only head/neck coil. The standard parameters used for the transversal 2D-SE/FLAIR/MDME sequences are described in table 2.3. Since there were clinical necessities for adjustments the number of slices and the FoV vary in some cases. These adjustments were executed for all of the patient's sequences to maintain a good intrapatient comparability.

2.3.3 Data processing

The MDME datasets were evaluated with the syngo.via (Siemens Healthcare, Erlangen, Germany) Plugin SyMRI 11.2 (SyntheticMR, Linköping, Sweden) where the parameter quantification of T_1, T_2 and PD, synthesis of images and segmentation of tissues are implemented. For each patient the contrasts with the same timing parameters ($T_R/T_E/T_I$)

Table 2.3: Clinical routine standard patient data acquisition parameters for T_2-/T_2-FLAIR/T_1-weighted conventional sequences and MDME-sequence.

	T2w	T2FLAIR	T1w	MDME
T_R (ms)	5000	8500	550	4000
T_E (ms)	92	86	8.9	22/97
T_I (ms)	-	2440	-	173/617/1802/3876
FoV (mm)	210	210	210	210
base resolution	512	320	320	320
phase resolution (%)	70	75	80	75
acceleration factor	1	1	1	2
slices	27	27	27	27
slice thickness (mm)	5	5	5	5
slice gap (%)	10	10	10	10
averages	2	1	1	1
bandwidth (Hz/pixel)	191	191	150	150
turbo factor	17	15	1	5
scan time (min)	3:25	3:40	2:45	6:56

as conventionally acquired images (T_1/T_2/FLAIR-weighted images) were synthesized. Finally the generated masks for ICV, WM and GM and the required synthetic images were exported to the Picture Archiving and Communication System (PACS).
Before the quantitative assessment, e.g. calculation of SSIM and contrast between WM and GM, the images were motion corrected. The coregistration was implemented with the Statistical Parametric Mapping toolbox SPM12 (UCL Queen Square Institute of Neurology, London, UK). The same parameters as in chapter 2.1.3 were chosen. Due to the fact that the series derived from the MDME data of the patients, e.g. the synthetic sequences and the ICV/WM/GM masks, are aligned per definition only the conventional acquired images were pairwise coregistered to the matching synthetic images. The coregistration downscaled the conventional acquired images to the size of the synthetic images with bicubic interpolation.

2.3.4 Quantitative Assessment

The quantitative assessment of the images was implemented with MATLAB R2019b (The MathWorks Inc., Natick, USA). The SSIM and the WM/GM-contrast was calculated slicewise. Before these calculations the number of considered slices was reduced as follows:

first, the upper and lower slices without a mask of the ICV were discarded and second, from the remaining volume the 10% lowest and highest slices were neglected.
The synthetically and conventionally acquired images were masked with the corresponding ICV mask. The images were normalized with the according 95%-percentile in order to get a similar dynamic range, which was defined as L to calculate the constants for the SSIM (eq. 2.8).
The contrast was calculated separately for the conventional and synthetic images with the following ratio

$$C = \frac{I_{WM} - I_{GM}}{I_{WM} + I_{GM}} \tag{2.17}$$

where I_{WM} and I_{GM} are the mean intensities of the corresponding region of interest. Therefore, the pixel intensities where the WM or GM mask exceeded the limit of 95%, which means a significant certainty for white respectively grey matter segmentation, were averaged.

2.3.5 Qualitative evaluation

The synthetic and conventional image sets were randomized and anonymized. 5 radiologists (years of experience: 9, 12 and three times > 20) assessed the following parameters on a 4-point Likert-scale of each set:

- overall image quality (IQ) with
  1-excellent, 2-good, 3-sufficient and 4-poor

- diagnostic certainty (DC) with
  1-certain, 2-almost certain, 3-probable and 4-possible

3 Results

3.1 Preliminary evaluation of the SSIM

In figure 3.1 exemplary the reference image and the compared image with the SSIM-map is depicted. The top row shows the comparison before, and the bottom row after the coregistration of experiment 4. Table 3.1 shows the mean and standard normal deviation SSIM values across the sets and slices for each experiment of the preliminary evaluation.

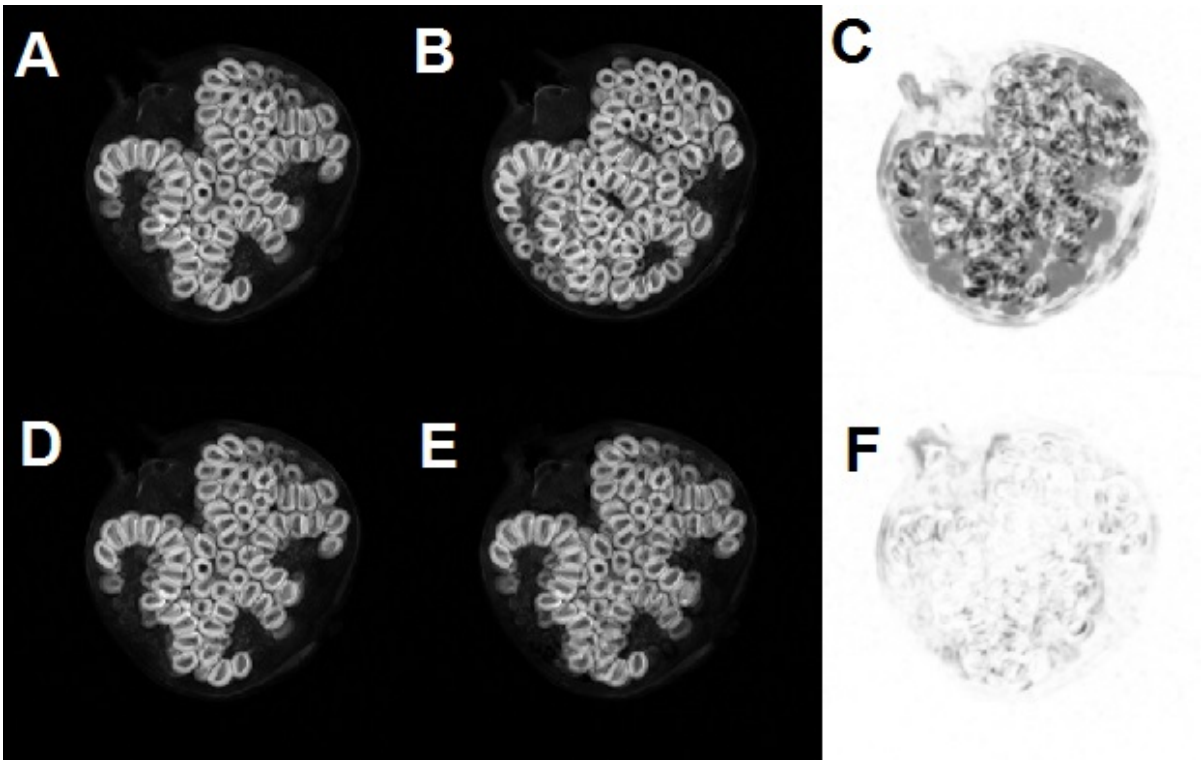

Figure 3.1: Central acquired slice, A and D before and B and E after the second intended motion. Top row: C is the SSIM-map of A and B with averaged SSIM of 30.72% before coregistration, bottom: F is the SSIM-map of coregisterd slices (88.33%).

Table 3.1: SSIM of the experiments as mean value and standard normal deviation across the processed slices. 512 and 320 are the base resolution, the number of the measurement in brackets, *PR75* refers to a phase resolution of 75% (interpolation by the scanner) and *MOTION1/MOTION2* are acquired after the first or second intended motion.

Experiment no.	Reference Images	Images	mean [%]	std [%]
1 (identical)	512 (1), 320 (1)	512 (2), 320 (2)	98.228	1.940
2 (downsampling)	512 (1), (2)	320 (1), (2)	95.822	1.415
3 (phase res.)	512, 320, each (1), (2)	512, PR75, 320, PR75	98.347	2.007
4 (intended motion)	512 (1), (2)	512, MOTION1, 2	58.331	32.949
4 (coregistered)	512 (1), (2)	512, MOTION1, 2	91.930	5.701

3.2 Comparison of tissue quantification by QRAPMASTER and conventional methods

In figure 3.2 the T_1-maps (top row) and the relative errors of QRAPMASTER- (middle) and VFA-method (right) compared to the gold-standard considered IR-approach (left) of the acquisition set 1 are shown.

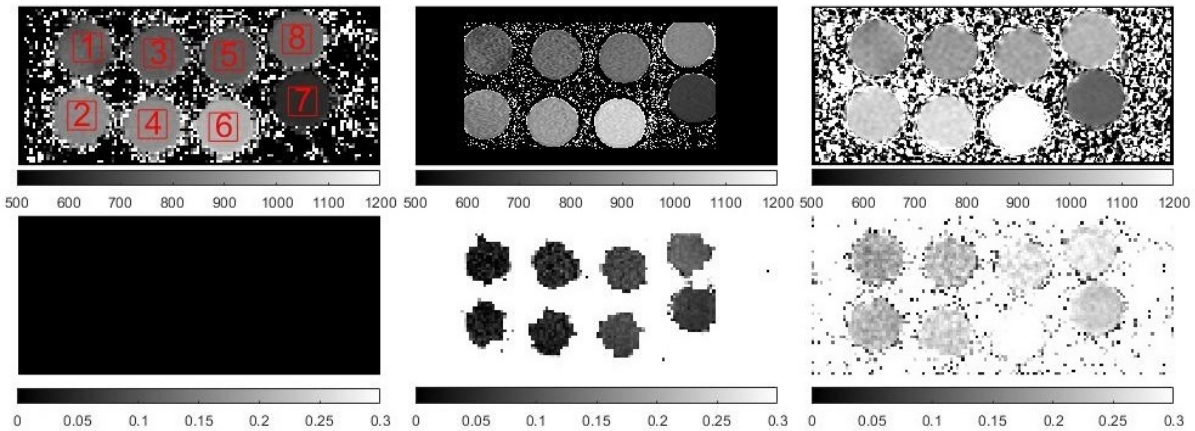

Figure 3.2: Quantitative T_1 maps (top row) and relative error (bottom) compared to IR. IR- (left), QRAPMASTER- or MDME- (center) and VFA-approach (right) of measurement 1. Same ROIs as shown in left map are used for the evaluation of the other methods.

In table 3.2 the quantified T_1 values within the separate regions of interest are stated. The column *Acquisition* refers to the measurement set on a specific time point. In table 3.3 the relative error in % is stated where the true value is defined as T_1 value of the method in column *Ref.*, e.g. IR of the respective acquisition. For acquisition $3-6$ the true value is defined as mean of the other three acquisitions, e.g. for aquisition 3 the mean of MDME acquisitions 4, 5 and 6. The last column *mean* refers to the average across the ROIs.

Table 3.2: T_1 of different Regions of Interest (ROIs) in *ms* with the IR-, MDME- and VFA-approach.

Acquisition	Method	ROIs							
		1	2	3	4	5	6	7	8
1	IR	761.83	881.47	756.31	892.75	748.28	986.70	620.32	782.60
	VFA	907.87	1066.65	927.03	1113.14	952.97	1312.06	770.59	1000.07
	MDME	753.60	859.24	797.46	927.39	809.94	1069.01	660.71	868.55
2	IR	689.62	812.09	709.38	809.97	706.28	913.41	590.61	748.10
	MDME	677.32	799.73	732.51	850.32	738.91	987.93	619.34	781.93
3	MDME	683.67	831.23	760.92	891.22	778.20	1047.61	653.71	874.62
4	MDME	693.15	838.07	769.07	897.76	783.01	1051.90	656.00	875.04
5	MDME	694.23	838.91	770.63	902.11	782.15	1051.97	648.87	865.56
6	MDME	692.72	835.61	768.25	901.83	783.34	1050.95	651.04	863.80

Table 3.3: The relative error of T_1 quantification for different ROIs and methods compared to *reference* method. Error and *mean* across ROIs in %.

Acq.	Ref.	Method	ROIs								mean
			1	2	3	4	5	6	7	8	
1	IR	VFA	19.17	21.01	22.57	24.69	27.35	32.97	24.23	27.79	24.97
		MDME	1.08	2.52	5.44	3.88	8.24	8.34	6.51	10.98	5.87
2	IR	MDME	1.78	1.52	3.26	4.98	4.62	8.16	4.86	4.52	4.21
3-6	mean of MDME	MDME	1.40	0.75	1.09	1.04	0.59	0.38	0.27	0.75	0.78
		MDME	0.43	0.34	0.32	0.07	0.23	0.16	0.74	0.81	0.39
		MDME	0.64	0.47	0.59	0.58	0.08	0.17	0.72	0.64	0.49
		MDME	0.34	0.05	0.18	0.53	0.28	0.04	0.28	0.91	0.33

A similar depiction is chosen for the quantitative T_2 maps and the relative error. Here, the QRAPMASTER- (middle) and MSE-method (right) are compared to the gold-standard, which is considered to be a spin-echo acquisition with only one refocusing pulse. In comparison, the MSE-method uses more refocusing pulses acquiring multiple echoes after one excitation.

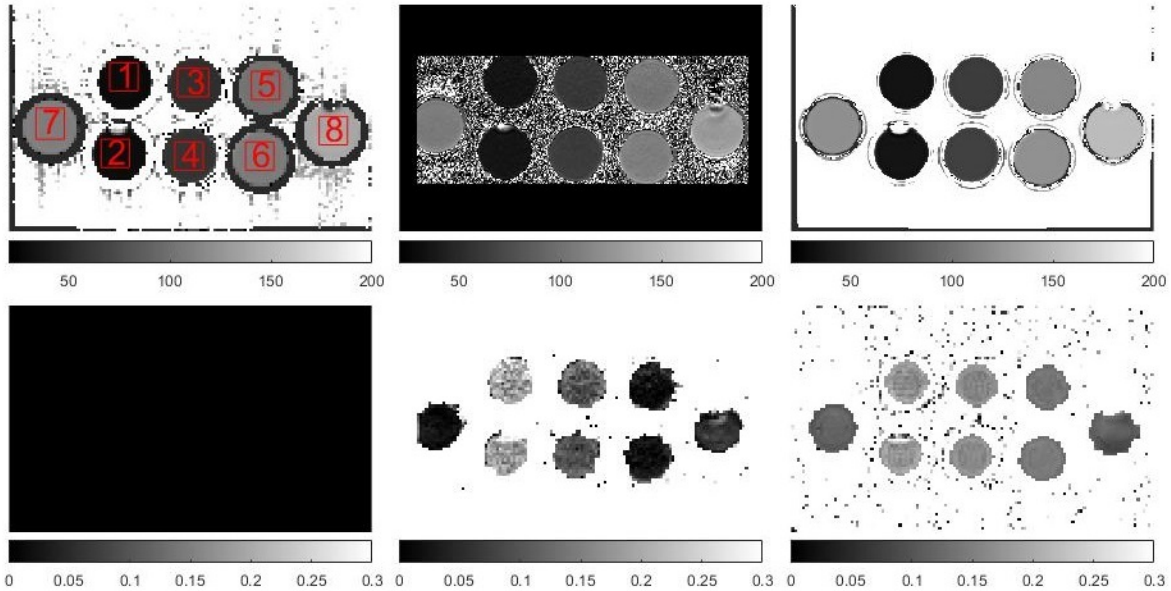

Figure 3.3: Quantitative T_2 maps (top row) and relative error (bottom) compared to SE with different echo times. SE- (left), QRAPMASTER- or MDME- (center) and MSE-approach (right) of measurement 2. Same ROIs as shown in left map are used for the evaluation of the other methods.

Table 3.4 shows the quantified T_2 values with the different approaches. Again, *Acquisition* refers to the different time points of the measurement. Table 3.5 shows the relative error with respect to a reference method. The MDME quantifications of acquisitions 1 and 2 are compared to the MSE-approach. The spin-echo method with different echo times was only acquired once (measurement 2) and compared to MDME- as well as the MSE-approach of the respective measurement. Analogue to the relative error of T_1 determination, the error for acquisitions 3-6 is referenced to the mean of the other three MDME measurements of this group.

Table 3.4: T_2 of different Regions of Interest (ROIs) in *ms* with the SE- , MDME- and MSE-approach.

Acquisition	Method	ROIs							
		1	2	3	4	5	6	7	8
1	MSE	32.95	33.15	61.26	63.43	113.27	118.56	120.99	152.46
	MDME	32.53	32.86	57.40	59.52	101.57	107.54	109.88	133.74
2	SE	28.85	29.24	54.33	56.93	101.82	107.37	108.00	138.07
	MSE	33.27	34.05	61.35	64.47	112.70	119.61	118.21	149.97
	MDME	34.42	34.72	59.66	62.09	103.18	108.88	106.60	128.42
3	MDME	32.89	32.67	57.20	58.73	99.41	103.36	109.91	133.00
4	MDME	32.68	32.64	57.69	59.39	100.40	104.48	110.74	133.48
5	MDME	32.70	32.63	57.87	59.06	100.79	104.50	108.88	132.83
6	MDME	32.69	32.68	57.61	59.10	100.81	104.38	108.42	132.83

Table 3.5: The relative error of T_2 quantification for different ROIs and methods compared to *reference* method. Error and *mean* across ROIs in %.

Acq.	Ref.	Method	ROIs								mean
			1	2	3	4	5	6	7	8	
1	MSE	MDME	1.26	0.90	6.29	6.17	10.32	9.30	9.19	12.28	6.96
2	SE	MSE	15.34	16.42	12.92	13.25	10.68	11.39	9.45	8.62	12.26
		MDME	19.34	18.73	9.82	9.07	1.33	1.41	1.30	6.99	8.50
	MSE	MDME	3.47	1.99	2.75	3.70	8.45	8.97	9.82	14.37	6.69
3-6	mean of MDME	MDME	0.61	0.08	0.91	0.76	1.25	1.05	0.52	0.04	0.65
		MDME	0.23	0.06	0.22	0.72	0.06	0.39	1.53	0.45	0.46
		MDME	0.18	0.11	0.65	0.02	0.58	0.41	0.74	0.20	0.36
		MDME	0.20	0.09	0.05	0.06	0.61	0.26	1.29	0.21	0.35

Table 3.6 reflects the effective longitudinal magnetization M_0 which is also referred to as pseudo proton density, quantified by the different approaches at the different acquisition occasions. There is one essential difference between the MDME-method and the other approaches: only the MDME-images were reconstructed with a prescan normalization by the scanner software which corrects amongst others the coil sensitivities. Therefore, the

error between different measurements is only comparable between the MDME quantifications. The relative error for each measurement is referenced to the average M_0 of the other acquisitions. *mean* is the mean value of ROI 1 to ROI 7 since ROI 8 is normalized to 1 for each measurement.

Table 3.6: M_0 of ROIs in *a.u.* with different approaches. For each method the value is normalized by the pseudo proton spin density of ROI 8. For all images except the MDME-method the prescan normalization was turned off for reconstruction.

Acquisition	Method	ROIs							
		1	2	3	4	5	6	7	8
1	IR	0.554	0.769	0.563	0.816	0.723	0.970	1.269	1.000
	VFA	0.608	0.885	0.579	0.877	0.727	1.032	1.272	1.000
	MSE	0.609	0.803	0.580	0.792	0.731	0.907	1.389	1.000
	MDME	0.772	0.778	0.889	0.896	0.954	0.981	1.032	1.000
2	IR	0.455	0.669	0.447	0.618	0.567	0.775	1.056	1.000
	SE	0.533	0.795	0.466	0.668	0.565	0.740	1.014	1.000
	MSE	0.423	0.584	0.412	0.567	0.536	0.673	1.049	1.000
	MDME	0.802	0.800	0.916	0.930	0.982	0.988	1.017	1.000
3	MDME	0.754	0.763	0.860	0.886	0.930	0.946	0.973	1.000
4	MDME	0.754	0.759	0.864	0.883	0.931	0.943	0.976	1.000
5	MDME	0.748	0.751	0.853	0.871	0.912	0.925	0.971	1.000
6	MDME	0.752	0.749	0.858	0.874	0.917	0.926	0.991	1.000

Table 3.7: The relative error of M_0 quantification for different ROIs and methods compared to *reference* method. Error and *mean* across ROIs in %.

Acq.	Ref.	Method	ROIs								mean
			1	2	3	4	5	6	7	8	
1	mean of MDME	MDME	1.277	1.738	2.114	0.850	2.083	3.726	4.697		2.355
2		MDME	6.094	5.259	5.908	5.450	5.725	4.662	2.886		5.141
3		MDME	1.513	0.529	1.760	0.581	1.006	0.655	2.461		1.215
4		MDME	1.500	1.255	1.283	0.896	0.810	1.032	2.063		1.263
5		MDME	2.440	2.374	2.811	2.575	3.308	3.387	2.663		2.794
6		MDME	1.832	2.764	2.075	2.177	2.591	3.215	0.316		2.139

3.3 Phantom contrasts with different aquisition strategies

Table 3.8 shows the calculated value of the MTR according to equation 2.16.

Table 3.8: MTR in %.

Acquisition	Method	ROIs							
		1	2	3	4	5	6	7	8
1	GRE	21.22	22.04	12.48	13.01	6.98	7.79	3.90	3.64

Two phantoms were selected which should imitate the WM (phantom 3) and GM (6) tissue. The quantitative values of these phantoms, estimated by the MDME-approach of acquisition 3, are T_1 760.92ms, T_2 57.20ms and M_0 0.86, respectively 1047.61ms, 103.36ms and 0.95. The intensities and contrasts of the different acquisitions are stated in table 3.9. *Ratio* is the contrast of the TSE (turbo factor 17) contrast divided by the SE contrast respectively the synthetic contrasts generated with the MDME-sequence divided by the conventional TSE contrast. All images are acquired or synthesized with T_R 5000ms and T_E 92ms.

Table 3.9: Signal intensities of ROIs (in column *Phantoms*) and the according *Contrast* of conventional (*CONV*) and synthetic *(SYN)* T_2-weighted images with T_R 5000ms and T_E 92ms. *Ratio* of TSE and SE acquisitions and MDME and TSE acquisitions.

Acquisition	Method	Type	Phantoms		Contrast	Ratio
			3	6		
3	TSE	CONV	351.76	744.82	-0.3584	83.66
3	SE	CONV	260.30	650.52	-0.4284	
3	MDME	SYN	1629.37	3773.03	-0.3968	110.70
4	MDME	SYN	1692.92	3837.76	-0.3878	108.19
5	MDME	SYN	1702.03	3857.45	-0.3877	108.16
6	MDME	SYN	1696.05	3852.81	-0.3887	108.44

In the case of the contrast comparison for T_1-weighted images, the WM is imitated by phantom 5 (T_1 778.20, T_2 99.41 and M_0 0.93) and GM by phantom 6. All of the synthetic and conventional images have the same setting of T_R 550ms and T_E 8.9ms.

Table 3.10: Signal intensities of ROIs (in column *Phantoms*) and the according *Contrast* of conventional (*CONV*) and synthetic *(SYN)* T_1-weighted images with T_R 550ms and T_E 8.9ms. *Ratio* of TSE and SE acquisitions and MDME and SE acquisitions.

Acquisition	Method	Type	Phantoms		Contrast	Ratio
			5	6		
3	TSE	CONV	712.83	604.06	0.0826	91.32
3	SE	CONV	462.56	385.82	0.0904	
3	MDME	SYN	4364.21	3509.86	0.1085	119.96
4	MDME	SYN	4342.69	3505.44	0.1067	117.95
5	MDME	SYN	4337.47	3521.09	0.1039	114.86
6	MDME	SYN	4354.29	3526.88	0.1050	116.07

3.4 Quantitative comparison of in vivo data

In figure 3.4 exemplary data and results of the SSIM calculation for a single slice are shown. The motion corrected images, acquired conventionally (A) or synthesized (B) are masked with the according binary ICV (C). The trimmed volumes are scaled with the respective 95%-percentile (D: conventional and E: synthetic). The similarity is calculated for each pixel according to equation 2.1 and depicted in (F) as SSIM-map. The SSIM between the conventional and synthetic image for a slice is the mean of the SSIM-map inside the ICV.

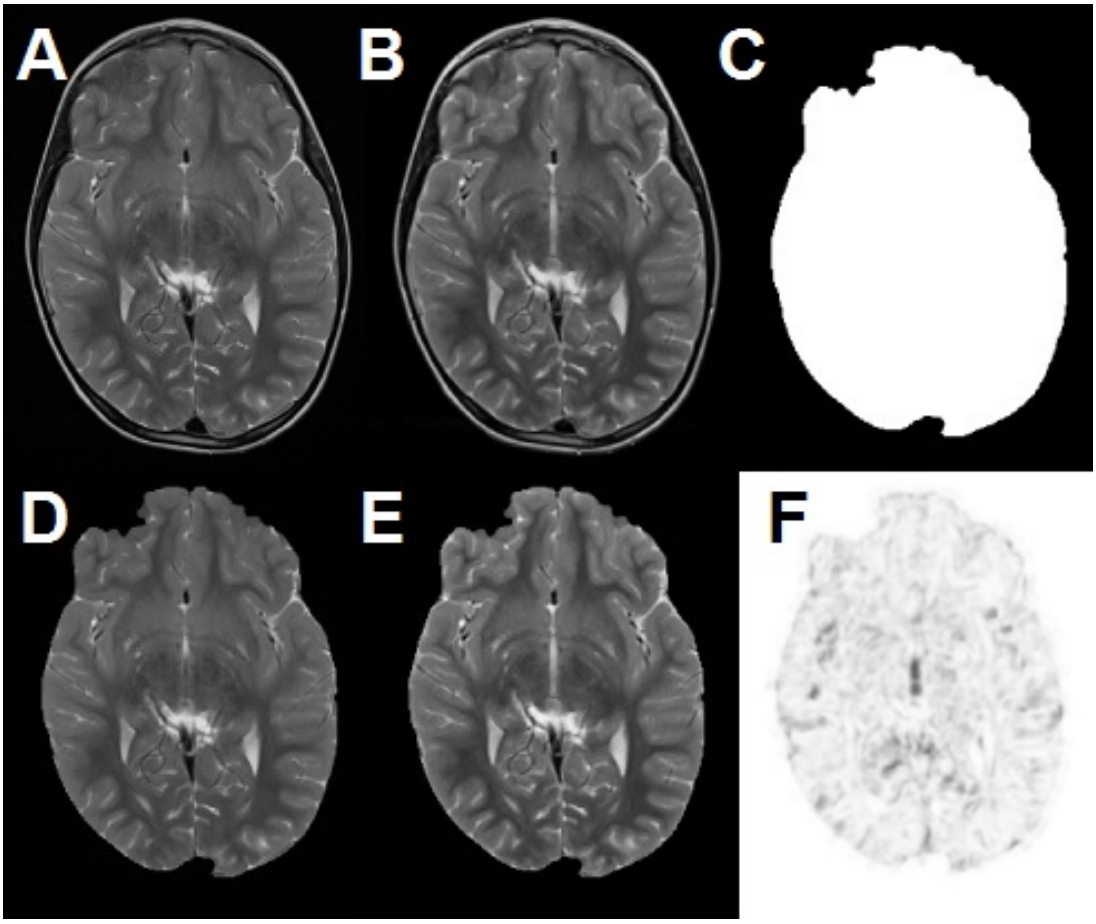

Figure 3.4: Conventionally acquired (A, acquisition matrix 512x325) and synthesized (B, acquisition matrix 320x217) slice with the respective masking and scaling (D) and (E). The average of the SSIM-map (F) inside the ICV mask (C) is 81.19%.

Interpatient variation with subsequent differences in the ICV segmentations results in averaged 20.25 (T_2- and T_2-FLAIR-weighted) and 20.55 (T_1-weighted) slices per patient and sequence. The overall result of the in vivo SSIM comparison is written in table 3.11.

Table 3.11: Mean and standard deviation of SSIM between the conventional and synthetic images across all patients and slices.

	T2-weighted	T2-FLAIR-weighted	T1-weighted
mean [%]	77.864	63.123	69.322
std [%]	4.359	4.879	5.180

In figure 3.5, exemplary a synthetic (A) and a conventional image (D) are shown with the respective WM- (B and E) and GM-masking (C and F). The contrast for each slice is calculated according to equation 2.17.

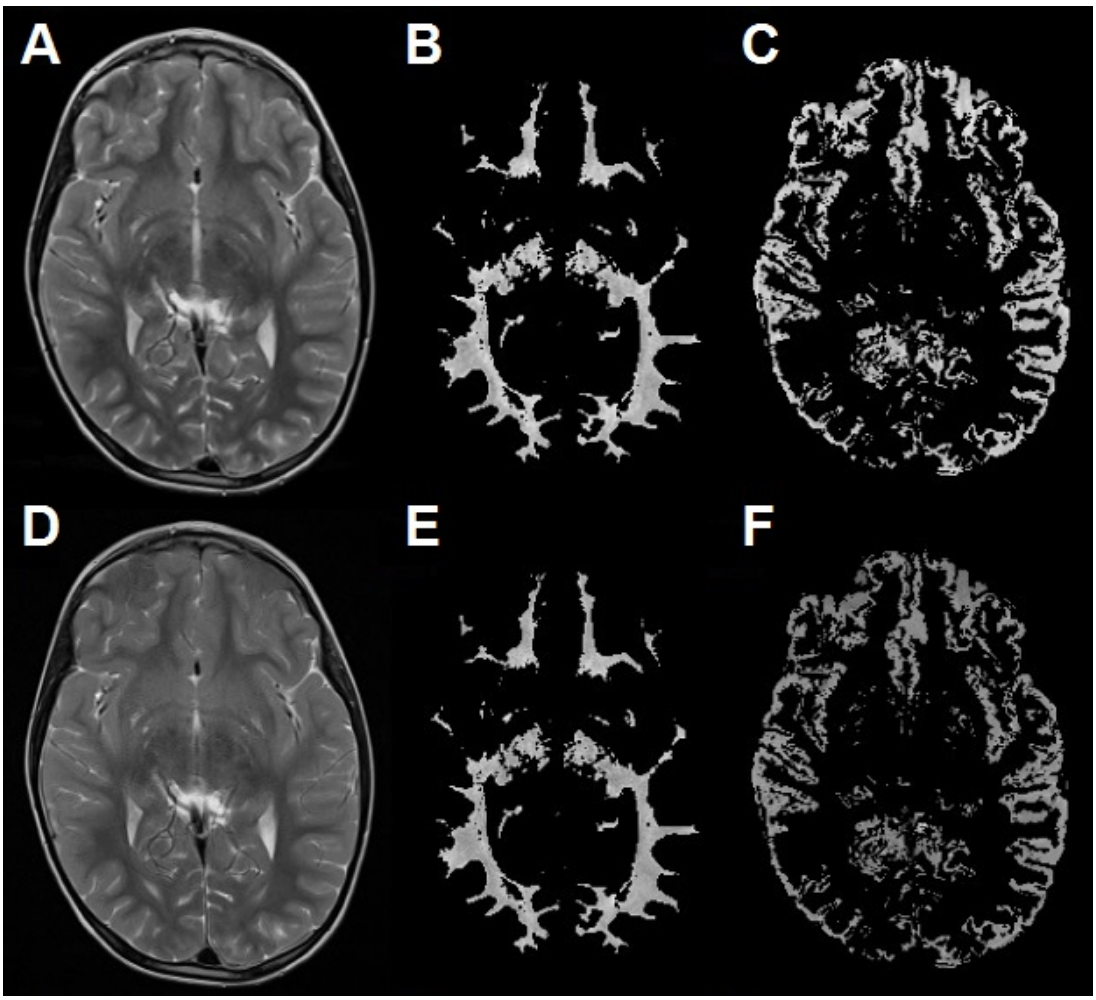

Figure 3.5: Synthetic image (A, acquisition matrix 320x217) masked with WM (B) and GM (C), same in bottom row for conventional acquired T_2-weighted image (D, acquisition matrix 512x325). The ratio of synthetic to conventional contrast is 139.65%.

Interpatient variation and hence differences in the white and grey matter masks results in averaged 20.00 (T_2- and T_2-FLAIR-weighted) and 20.50 (T_1-weighted) slices per patient and sequence for the WM/GM-contrast calculation. In table 3.12 the overall results for all patients and sequences is reflected.

Table 3.12: Mean and standard deviation of WM/GM-contrast for synthetic (*SYN*) and conventional acquired (*CONV*) images across all patients and slices.

Sequence		mean	std	ratio [%]
T2w	SYN	-0.2300	0.0267	141.58
	CONV	-0.1624	0.0231	
T2w-FLAIR	SYN	-0.0933	0.0420	156.25
	CONV	-0.0597	0.0263	
T1w	SYN	0.1485	0.0121	113.37
	CONV	0.1310	0.0158	

3.5 Subjective evaluation of in vivo data

Five radiologists with 9 (rater 1), 12 (rater 2) and more than 20 years (all others) of experience assessed the conventional and synthetic images anonymized and blinded. The mean value for each sequence and rater as well as the combined value is stated in table 3.13.

Table 3.13: Mean of the subjective assessment by the raters 1 to 5 individually and combined (*all*) for synthetic (*SYN*) and conventional acquired (*CONV*) images. Rating for *Diagnostic Certainty* includes 1-certain, 2-almost certain, 3-probable and 4-possible and for the *Image Quality* 1-excellent, 2-good, 3-sufficient and 4-poor.

Parameter		Diagnostic Certainty						Image Quality					
Rater		1	2	3	4	5	all	1	2	3	4	5	all
T2w	SYN	2.38	3.17	1.25	2.83	3.42	2.61	2.88	3.28	1.82	2.90	3.57	2.89
	CONV	1.35	1.28	1.07	1.20	1.18	1.22	1.52	1.42	1.25	1.27	1.20	1.33
T2w-FLAIR	SYN	2.35	3.22	1.37	2.82	3.50	2.65	2.95	3.37	1.92	2.90	3.70	2.97
	CONV	1.73	1.78	1.17	1.72	1.88	1.66	1.93	1.88	1.42	1.83	2.02	1.82
T1w	SYN	1.95	2.65	1.00	2.50	2.75	2.17	2.30	2.65	1.35	2.60	2.90	2.36
	CONV	1.75	1.70	1.00	1.65	1.60	1.54	1.75	1.65	1.10	1.65	1.65	1.56

For a clear visual depiction the values of the overall image quality (IQ) are also presented in a diagram in figure 3.6.

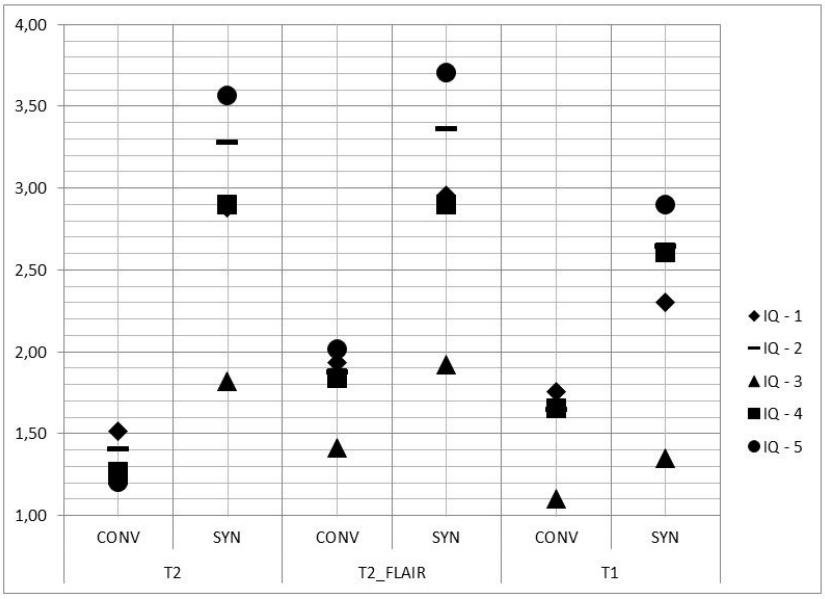

Figure 3.6: Mean of overall image quality (IQ) assessed by rater 1 to 5.

4 Discussion

4.1 Preliminary evaluation of SSIM

By repeating the same acquisition with the same phantom and identical parameter settings subsequently, several influences on the resulting image are eliminated. These dependencies include the field inhomogeneities of the static field B_0 and the transmit and receive field B_1, the coil sensitivities and temperature effects. Furthermore the usage of a phantom eliminates the effects of motion. Therefore, the result of experiment 1 (table 3.1) where two identically acquired images are compared is the consequence of noise on the SSIM. This result can be divided into the comparison of the two acquisitions with a base resolution of 320 and 512 with an average similarity of 99.733% and 96.724%, respectively. The difference can be explained by the fact that a larger scan matrix is associated with a lower SNR since the volume of an acquired voxel is smaller. Considering the larger base resolution the SSIM can be considered as a full reference metric which is sensitive with respect to noise assuming it as the only difference between the images.

The downsampling of the larger image with a bicubic interpolation results in an average SSIM of 95.822% as stated in table 3.1, experiment 2. With the bicubic method the calculated pixel is a weighted average of pixels in the nearest 4-by-4 neighbourhood. Other methods like bilinear interpolation (weighted average in 2-by-2 neighbourhood) and filtering with a Lanczos-2 and Lanczos-3 kernel were also tested, each of them yielding a lower similarity. Therefore, the bicubic interpolation method is chosen for the in vivo comparison. Nevertheless, the downsampling of an image and the subsequent comparison with the same acquired volume reduces the SSIM independent on the interpolation method. Figure 4.1 shows an image downsampled from 512x512 to 320x320, the same slice acquired

with base resolution 320 and the according SSIM-map. Both images were acquired with 70% phase resolution and reconstructed by the scanner software to the squared size with zero-filling of the k-space before the transformation (sinc-interpolation). This example demonstrates the sensitivity of the SSIM despite the practically non-existing differences when observing visually.

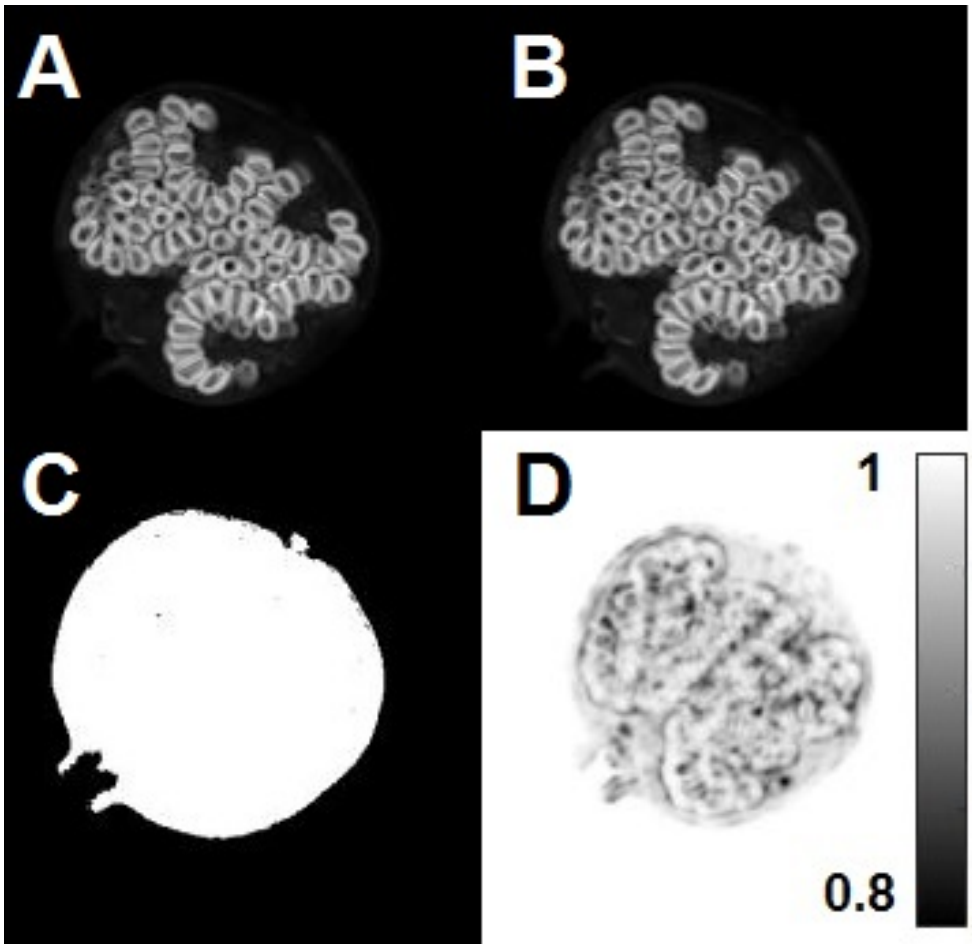

Figure 4.1: Exemplary depiction of experiment 2 (downsampling), with the downsampled image (A), image acquired with scan matrix 320 (B), masking for considering only a region with significant signal (C) and the SSIM-map (D)with an average of 95.390% inside the mask.

Experiment 3 reveals an interesting point: the overall mean SSIM of the comparisons is 98.347 and thus marginally higher than the comparison of the identically acquired images. When observing the individual sets, the SSIM of the 320x320 images with phase resolution

70% compared to 75% is lower than for the identically acquired images. This outcome was expected although the difference is very small with a value of 0.2%. The overall higher similarity can be explained since the similarity of set 512, acquisition 2 (70%) to 512, 75% is higher than compared with 512, acquisition 1 (70%). This outcome was not expected and could be explained with statistical variation but to validate this theory further measurements would be necessary. However, the conclusion of this experiment is that the change of the phase resolution from 70% to 75% has only a marginal effect on the SSIM which can be neglected compared to other variations.

The last experiment shows the dependence of intended motion on the similarity measure. The combined average value of 58.331% across the sets after the first and the second intended motion again indicates the sensitivity of the calculation, the standard deviation of 32.949% arises from the different magnitude of motion. After *MOTION1* a SSIM of 90.221% and after *MOTION2* 26.440% is achieved which indicates the inherent dependance on the range of motion itself, as it is expected. Furthermore, a significant increase of the values after the coregistration illustrates the function of the correction although smaller similarities of 97.242% (*MOTION1*) and 86.618% (*MOTION2*) are achieved. This experiment shows the SSIM dependance on motion of the acquired object between the measurements and the effect of coregistration. It can be presented that the correction of a higher magnitude of motion is not sufficient enough to achieve the same similarity as without motion for this case. Furthermore it should be considered that in vivo volumes can also move during the acquisition itself which has other effects like blurring or ghosting. This relation cannot be shown with the here used settings with a pomegranate.

In conclusion the SSIM can be considered as a sensitive method for the evaluation of different acquisition matrices and motion between the measurements whereas the change of the phase resolution has only a marginal effect for the here presented experiment.

4.2 Quantification by QRAPMASTER

Monoexponential behaviour

An essential point of the quantification with the QRAPMASTER sequence is the assumption of a monoexponential decay for both, the longitudinal as well as for the transversal relaxation. This assumption might be not valid for various biological tissues, especially when considering white matter environments as discussed by Whittall et al. [20] and Labadie et al. [35]. On the other hand, a multiexponential decay can be useful for the determination of myelin as discussed in chapter 1.4.4 or give interesting insights into brain microstructure as stated by MacKay et al. [36] The multiexponential effect is also particulary strong at the interface of brain tissue and CSF may leading to partial volume errors. [14] However, the QRAPMASTER uses only a limited number of data points for the determination of the parameters, for instance two echoes (22 and 97ms) and four saturation delay times (173, 617, 1802 and 3876ms) for the here presented acquisitions and results, which prohibits the accurate determination of multiple relaxation times. Hence, the quantified relaxation times are a composition of the fast and slow relaxations, mainly reflecting the dominant component. Therefore, the phantoms were assumed to decay monoexponentially despite the fact that especially samples with a high MTR may have a multiexponential relaxation behaviour. So the other qMRI approaches like the IR- and MSE-method were also fitted with a monoexponential decay for a better comparability. The resulting systematic error due to neglecting biexponential behaviour is thus similar for the quantification methods when using the same inversion- or echo-times, respectively.

Longitudinal Relaxation Time T_1

The relative error of the quantification by the VFA-method compared to the IR is significantly larger than the MDME determined T_1 as it is stated in table 3.3. One of the reasons for an error of the VFA-approach is the significant influence of the imperfect slice

profiles but this effect is minimized by the acquisition with a 3D-GRE. Another reason could be that the VFA-method relies in general on the crucial assumption of ideal spoiling of the transversal magnetization. [31] A considerable systematic error can be produced by neglecting the issue of incomplete spoiling. This means that the residual T_2 dependency results in a bias of the determination. [37] The relative error of the longitudinal relaxation time quantified by the VFA-approach (compared to the gold-standard IR) is plotted in relation to the transversal relaxation in figure 4.2. In the below represented measurements a direct proportionality between T_2 (determined by the MSE) and the error can be obtained. This behaviour was expected since a smaller relaxation time results in a faster decay or larger amount of elimination of the residual coherent transversal relaxation. Furthermore the T_1 overestimation may be caused by an inaccuracy of the B_1-mapping. Accurate results can be achieved by effectively destroying the residual transversal magnetization before each excitation pulse which can be achieved with a longer T_R. Another possibility would be the usage of a correction for the non-ideal spoiling by using the T_2 values as introduced by Heule et al. [37]

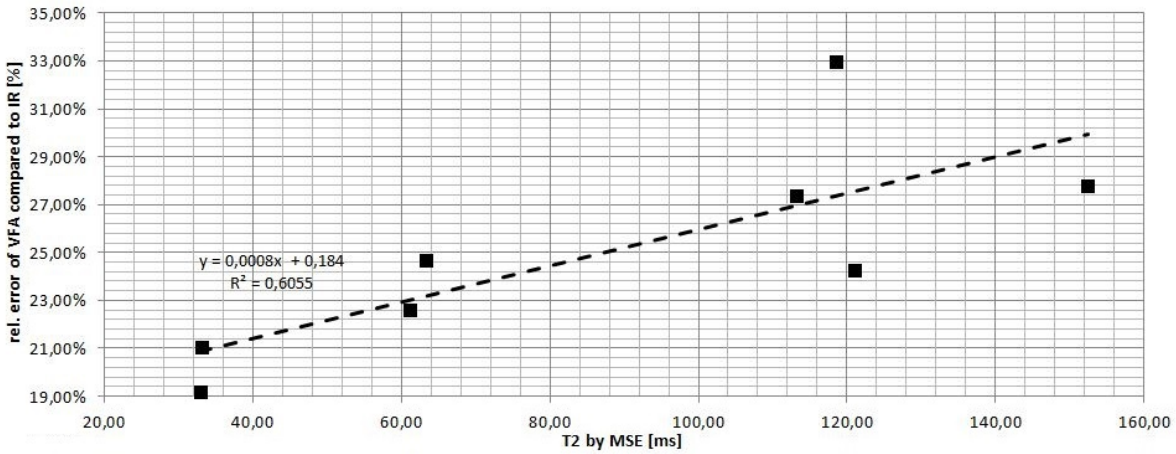

Figure 4.2: The relative error of T_1 by the VFA-method (compared to the gold-standard IR) in relation to the quantified T_2 (by the MSE). A direct proportionality can be obtained between error and T_2.

The relative error of the QRAPMASTER quantification compared to the gold-standard

IR-method is 5.87% (acquisition 1) and 4.21% (acquisition 2) as stated in table 3.3. Warntjes et al. compared the accuracy in a similar manner in vivo (brain) and obtained an overall mean error without CSF of 6.2%. The measurements were performed on a $1.5T$ Achieva scanner (Philips Medical Systems, Best, The Netherlands). The larger error can be explained by the differences in the acquisition parameters compared to the here presented experiments. They acquired the MDME data with a T_R of $2600ms$ (here: $4000ms$) and the inversion recovery with a large repetition time of $10000ms$. The here used repetition time of $6000ms$ (for IR) was chosen under the assumption that every phantom has a smaller T_1 of $1200ms$ to fulfill the condition $T_R > 5 \cdot T_{1,max}$ as described in chapter 2.2.2. However, by setting the standard parameters of the MDME sequence as in the clinical routine, i.e. T_R $4000ms$, the condition is violated and an error arises from the non-complete longitudinal relaxation before the next excitation. Figure 4.3 shows the relation of the quantification error between the MDME- and IR-method in relation to T_1 (determined by IR).

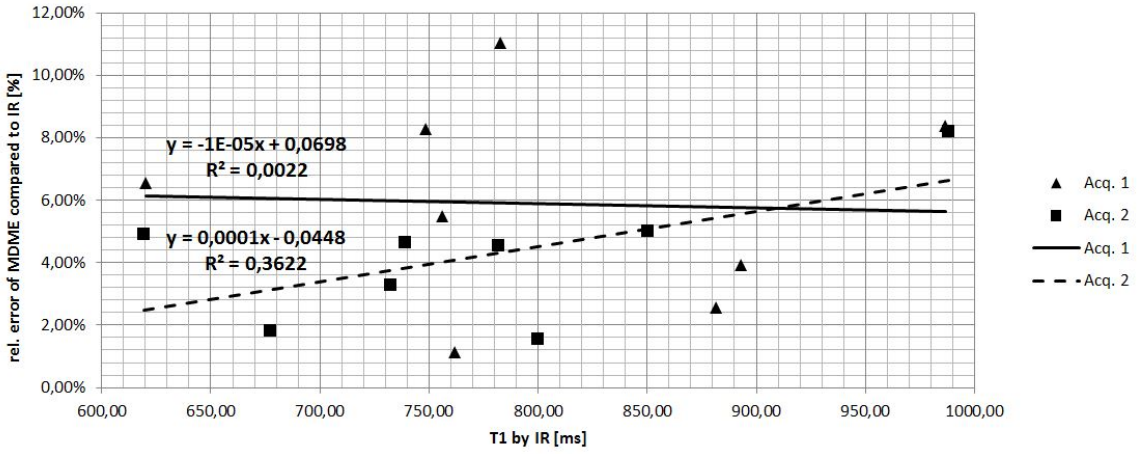

Figure 4.3: The relative error of T_1 by the MDME-method (compared to the gold-standard IR) in relation to the quantified T_1 (determined by IR). Acquisition 1 shows a direct proportionality between error and T_1.

Assuming a T_1 of $1000ms$, which was the maximal value of the phantoms, and an ideal saturation pulse, only 97.25% for T_R $4000ms$ and 88.86% (T_R $2600ms$) of the longitudinal

magnetization is recovered before the next excitation. The amount of relaxation with T_1 of $600ms$ is higher with 99.81% and 98.03%, respectively. Hence, T_R and the systematic error are indirect proportional, which could explain the difference of error between [6] and here. Furthermore, T_1 and the error are direct proportional where a tendency can be obtained for acquisition 2 in figure 4.3 despite a relatively low coefficient of determination of 0.3622. For acquisition 1, this relation cannot be stated since there is no tendency ($R^2 = 0.0022$). The systematic error can only be shown for one acquisition and should therefore be considered with limitations. First, the relationship is exponential and not linear, which should only show the tendency. Second, further measurements, e.g. repetitions, should be processed for full representation of this relationship since small changes can be blurred by different uncertainties, e.g. noise.

Krauss et al. evaluated the accuracy with a EurospinII-(TO5) phantom (Diagnostic Sonar, Livingstone, Scotland) with known values and obtained an relative error of the MDME-sequence of 4.45% on a $1.5T$ scanner. [38] The smaller error compared to the presented results in table 3.3 may be explained by a longer T_R of $4360ms$ or the knowledge of the relaxation times eliminating an amount of uncertainty in the reference measurement. Nevertheless, the error from [38] compared to that found in this study is very similar.

Hagiwara et al. evaluated the intrascanner repeatability with phantoms on $3T$ scanners (MAGNETOM Prisma, Siemens Healthcare). They repeated ten measurements over a period of 2 months and observed an intrascanner coefficient of variation for T_1 $506 - 1324ms$ of 1.38%. [39] The coefficient of variation defined as ratio of standard deviation and mean value for the 8 measured phantoms during acquisitions 3-6 is averaged 0.42%. The smaller value can be explained with less measurements and a smaller time span.

In conclusion, when considering practical applications (with T_R $4000ms$) the systematic eror is negligible for WM ($< 0.5\%$ to full longitudinal relaxation), small for GM ($2 - 5\%$) and crucial for the determination of CSF, e.g. approximately 30% for T_1 of $2500ms$. [2] Furthermore the T_1 determination with the QRAPMASTER-approach can be considered to have a high repeatability.

Transversal Relaxation Time T_2

From table 3.4 it can be obtained that the MDME-approach underestimates the value of T_2 compared to the MSE-method for both, acquisition 1 and 2. In figure 4.4 the relative error is plotted in dependance of the quantified T_2, showing an increasing error with larger relaxation times. Krauss et al. evaluated the performance and also stated an underestimation which is direct proportional to T_2. They applied 5 instead of 2 echo times at multiples of $15ms$ to the MDME-sequence and calculated a deviation of 6.6% related to known values of the phantoms. [38] In the here presented experiments an averaged error of 6.96% and 6.69% (table 3.5) is computed, only deviating little from literature despite the smaller amount of echo times.

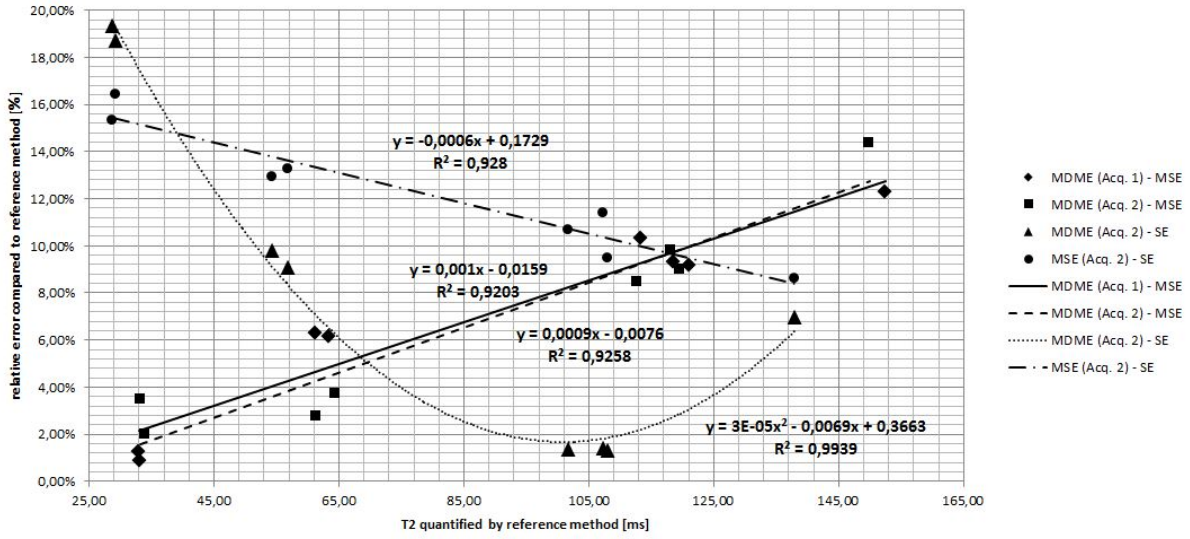

Figure 4.4: The relative error of T_2 by different methods (first name in legend) compared to reference method (second name in legend) in relation to the quantified T_2 (determined by reference method).

The in vivo experiment from Warntjes et al. shows a mean error of 5.2% in the brain without CSF when comparing MDME (5 echoes at multiples of $20ms$) with a MSE-sequence. [6] However, in a white paper by Warntjes it is recommended to use the least possible number of points, i.e. 2, to achieve the highest SNR per point and resulting in a

better fit of the T_2 relaxation within a given scan time. Furthermore the sensitivity of the 2-point approach to inhomogeneities and pulse profile imperfections should be corrected within the fitting algorithm. [40]

The differences between a multi- and single-spin-echo determination of T_2 as stated by Petrovic et al. [34] was the reason to quantify the phantoms also by the more accurate method. Contrary to the comparison to the MSE-method, the MDME T_2 values are bigger than quantified by the SE-method, at least for the agar phantoms $(1-6)$. Only the water phantoms are underestimated by MDME as stated in table 3.4. Furthermore the error between the SE-method and MDME is smaller (8.50%) than SE and MSE (12.26%) as written in table 3.5 or visually depicted in figure 4.4.
The repeatability study of Hagiwara et al. revealed a coefficient of variation of 0.90% for the Siemens scanner and relaxation times $32.9 - 127ms$. [39] The result of the here processed acquisitions $3-6$ averaged over all phantoms is 0.40%.

In summary, the measurements and quantifications presented here show a good repeatability. The application of the MDME sequence with two echo times show an acceptable error for a clinically relevant range when considering WM (T_2 of $77ms$, from [41]) and GM ($76 - 89ms$, [42] and [43]) of adults. Some differences can arise for larger relaxation times, e.g. for GM of infants by the model of Leppert et al. [3] T_2 decreases from $189ms$ (1 month) to $128ms$ (6 months).

Longitudinal magnetization M_0

Due to the switched off prescan normalization, it is impossible to compare the longitudinal magnetization M_0 of the IR-, VFA-, SE- or MSE-method with the MDME-approach. The results from table 3.7 show the error compared to the mean value within the MDME-sequence resulting in a coefficient of variation of 2.43% (acquisitions $1-6$) across all phantoms. Also the variation of acquisitions $3-6$ is with 0.72% higher than the variation for T_1 (0.42%) and T_2 (0.40%) of the same acquisitions. Similarly, Hagiwara et al. obtained

a higher coefficient of variation for the determination of the PD (1.70%) compared to T_1 (1.38%) and T_2 (0.90%).

Figure 4.5 shows the M_0 values of the different MDME acquisitions in relation to the determined MTR (table 3.8). Clearly, an indirect proportionality between the MT effect and the longitudinal magnetization, which is available for imaging, can be obtained. This behaviour can be explained since the cross-relaxation between the two pools of spins is the cause of a reduction in the free water signal. Furthermore the MT effect is also an intrinsic problem for multislice T_1 determination due to the off-resonance pulses as a result of slice cross-talks. [7] For example, Watanabe et al. [44] found a decrease in multislice determined T_1 compared to a single-slice acquisition. A larger MTR is linked to more cross-relaxation effects and hence a smaller visible magnetization as well as a shorter longitudinal relaxation time.

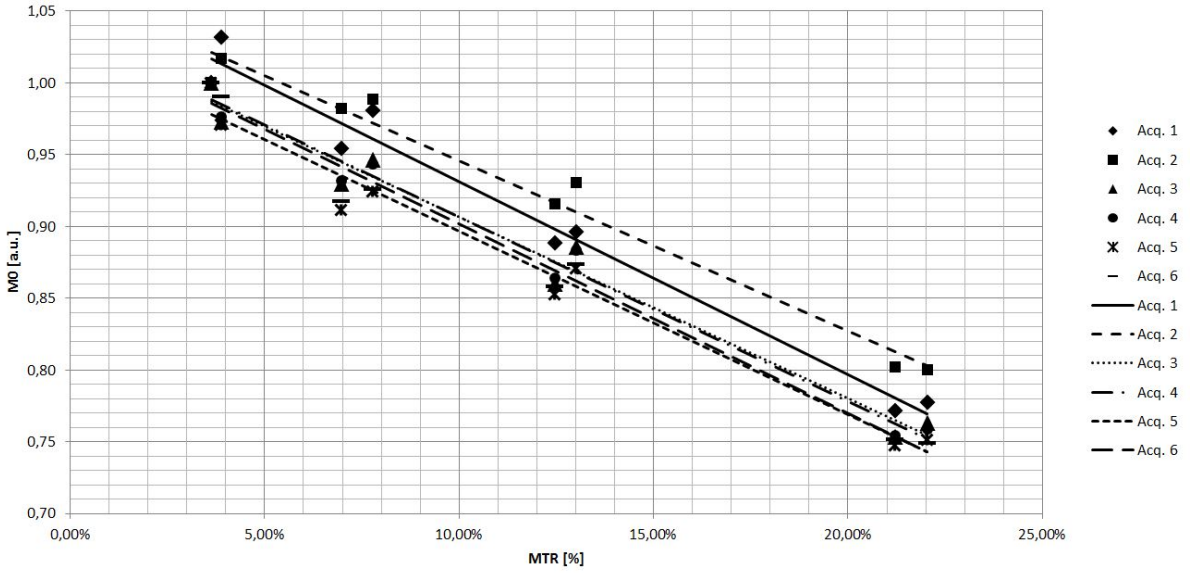

Figure 4.5: The longitudinal magnetization M_0 by the MDME-method in relation to the MTR. All acquisitions $1-6$ show a similar indirect proportionality between M_0 and MTR.

Warntjes et al. combined the reference methods (IR and MSE) to calculate the proton density resulting in a mean difference of 12.1% compared to QRAPMASTER. They explained the moderate accuracy as a result of elongated scan time and error propagation

from previous parameters. [6] Krauss et al. obtained a relative error of 3.3% when evaluating 12 test tubes with a known amount of relative water content from $50 - 100\%$ in 5% steps and 72.5%. From 65% to 90% an overestimation of PD was demonstrated. [38] Cercignani et al. may explain the inaccuracy due to limitations of the QRAPMASTER method, including the low number of relaxation points and a monoexponential fit. [45]

4.3 qMRI in clinical routine

Structural Similarity Index

The SSIM evaluation of in-vivo data (table 3.11) shows the highest similarity for T_2-weighted, a smaller agreement between synthetic and conventional T_1-weighted and an inferior similarity for T_2-FLAIR-weighted contrast images. Furthermore it should be considered that the T_2w set is the only one processed with downsampling of the larger conventional images. Taking the findings of the preliminary SSIM evaluation the result of 77.864% was also shortened by the downsampling. On the other hand the synthetic images have a lower resolution than the conventional ones. This influence is shown primarily by the radiologists in the subjective evaluation.

Tanenbaum et al. have observed more artifacts in T_2-FLAIR-weighted images than for T_1w and T_2w images. [46] Also Lee et al. [47] stated a lower quality for FLAIR images, Betts et al. [48] concluded a higher degree of artefacts and DiGiuliano et al. [49] suggested an improvement for the synthesis of T_2-FLAIR images. Hagiwara et al. improved the quality of synthetic FLAIR images using deep learning. Including generative adversarial networks in the pixel-by-pixel synthesis allows for suppression of hyperintense edges and areas, minimization of flow artefacts and a smoothening of CSF. [50] These improvements were implemented in the here used software SyMRI 11.2 to give a more natural appearance. Nevertheless, the similarity of T_2-FLAIR-weighted contrast images is inferior (63.123%) compared to T_1w (69.322%) and T_2w (77.864%) image sets.

Limitations of the SSIM evaluation include the weighting of a single pixel. The similarity is calculated slice-wise inside the ICV which is not equal in every slice. Therefore, a single pixel in a slice with a smaller segmented intracranial volume has a larger contribution to the SSIM of this slice. To reduce this effect, the number of slices was shortened to 80% by cutting 10% each at the base of the skull and at the calvaria where the ICV masks are expected to particulary small. Nevertheless, there are remaining variations in size leading to differences in the weighting.

Another point which should be considered is the segmentation itself which is stable and reliable under normal circumstances. The comparison inside the intracranial volume is sufficient but failures in the segmentation are not impossible which is shown in figure 4.6, an example of a slice with a difference in the segmentation due to a metal artefact, i.e. a shunt. Inside the ICV the SSIM is 71.29% whereas the similarity for the whole brain volume is clearly lower because a larger volume is darkened in the synthetic image. Patients with shunts or brackets were not excluded from the studies since SyntheticMR claimed a better performance of synthetic images compared to conventionally acquired sets in the case of known metal artefacts. In summary, 5 patients with metal in brain are evaluated and a SSIM of 77.37 (T_2w), 68.02 (T_1w) and 56.38 (T_2-FLAIRw) was calculated with only the latter one deviating from the results of table 3.11. Despite not every patient and slice showing such differences between conventional and synthetic images, the figure should exemplify the possibility of this error.

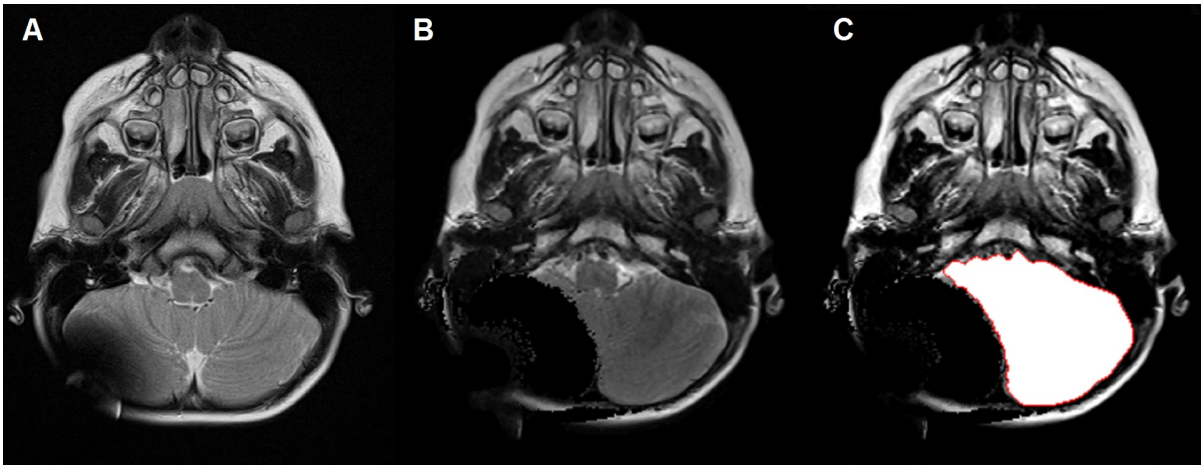

Figure 4.6: Conventional (A) and synthetic (B) T_2w (overlay of ICV in (C)) of a 3-year old patient with a shunt. The SSIM of this slice is 71.29% due to the small mask, whereas the visual similarity is quite inferior.

WM/GM Contrast

The comparison of WM/GM contrast between synthetic and conventional images is shown in table 3.12. The ratio of 141.58% (T_2w), 156.25 (T_2-FLAIRw) and 113.37 (T_1w) indicates a significant higher contrast in synthetic images. The contrast evaluation with the same calculation was done before but none of them used the WM and GM masks from the QRAPMASTER segmentation. [49][51] Both of them used 6 (GM) respectively 4 (WM) circular regions of interest with a diameter of $4mm$ which were marked by neuroradiologists in homogeneous areas to minimize partial volume effects. Blystad et al. [51] additionally considered the lesion to white matter contrast and obtained a 22% (T_2w), 25% (T_2-FLAIRw) and 32% (T_1w) better contrast for synthetic images. Another discrepancy besides the selection of the areas of [51] and the here evaluated images is the synthesis of FLAIR images according to [50] which was adapted certainly after the other study. Nevertheless, they obtained also a significant higher contrast in synthetic images. DiGiuliani et al. [49] evaluated the contrast in a similar manner but only reported a higher contrast for synthetic T_2w (8%) and T_2-FLAIRw (14%) images. Contrary to [51]

and this thesis they obtained a lower WM/GM contrast in synthetic T_1w (14%) images compared to the conventional ones.

Limitations of the WM/GM contrast calculation includes the selection of the masks. Both, WM and GM masks, have partly very small structures, which may suffer partial volume effects despite the thresholding with the value of 95%. It is assumed that the motion correction is valid but such small structures are also prone to minimal spatial variations. Analogous to the SSIM calculation, where the weighting of the pixels is dependent on the ICV mask, the contrast, which is also slicewise calculated, is depending on the size of the WM and GM masks. These masks can be very small, e.g. containing only a few pixels, which makes the calculation with an intensity ratio mathematically unstable. Furthermore the contrast varies also with the age of the patient since the relaxation times are age-related decaying as shown in 1.2. [3] [4] All these variables contribute to a large coefficient of variation across the slices and patients, especially for synthetic (45%) and conventional (44%) FLAIR images. Nevertheless, in conclusions these deviations cannot blur such large ratios indicating a higher WM/GM contrast of synthetic images in the case of T_2- and T_2-FLAIR-weightings.

Subjective evaluation of Diagnostic Certainty and Image Quality

Table 3.13 reveals the differences rated by experienced neuroradiologists for the diagnostic certainty and the overall image quality with the scores 1 (best rating) to 4 (worst rating). Both criterions are lower for synthetic than for conventional images across all raters except the diagnostic certainty for T_1w by rater 3. The mean overall image quality decreases by 1.56 (T_2w), 1.15 (T_2-FLAIRw) and 0.80 (T_1w) for all raters. Regarding the FLAIR compared to T_1w images an inferior quality can be observed which was also reported in literature. Tanenbaum et al. observed more artefacts in this type of reconstruction [46] and also DiGiuliano et al. found significant differences [49]. Betts et al. [48] and Lee et al. [47] assessed the image quality in children and reported a decrease of 0.85 on a 4-point [48] and 1.33 on a 5-point scale [47] for FLAIR images compared to 0.30 and

0.23 for T_1w images, respectively. The large difference for T_2w images can be explained by a smaller acquisition matrix for the QRAPMASTER sequence resulting in a lower resolution whereas the difference reported in literature is 0.30 ([48], 4 point scale) and 0.59 ([47], 5 point scale) for the same acquisition matrix.

There is a significant difference across the raters of this study independent of their experience. The lowest disagreement between synthetic and conventional images (0.57, 0.50 and 0.25) was assessed by rater 3 who has more than 20 years of experience. Rater 5 with a similar grade of practical experience rated the overall image quality of synthetic images 2.37 (T_2w), 1.68 (T_2-FLAIRw) and 1.25 (T_1w) worse than conventional acquired stacks. In general the tendency is the same for all raters as it can be observed in figure 3.6. Moreover the proportionality is similar for diagnostic certainty whereas the differences are smaller.

One possible limitation of this study depends on the experience of the reviewers. Despite the anonymization of the sequences, all raters are used to observing and diagnosing with conventional images which may lead to a bias in the rating. The comparison of the T_2-weighted images is influenced by the different acquisition matrices and resolutions. However, it was considered to leave the base resolution of 512 constant because it was used anyway in the clinical routine before the introduction of the QRAPMASTER sequence.

For a further evaluation of the differences in the rating for the image quality and diagnostic certainty, selected image stacks with a significant diverging rating of the conventional and the respective synthetic acquisitions are compared and discussed by radiologists. The following examples give justifications and further insights to the subjective assessment.
The first two examples in figure 4.7 and 4.8 show T_2-FLAIR-weighted conventional images (A, C) with the corresponding synthesized contrast images (B, D). In figure 4.7 motion within the MDME acquisitions is reconstructed to oval artefacts. This highlights the sensitivity for motion during the QRAPMASTER approach with the longer acquisition time prone to these artefacts. In figure 4.8 two examples are given where the visualization of the anatomy near the calvaria is not sufficient for synhtetic images. In (B) the differen-

tiation between white and grey matter is diffuse compared to (A). The black dots in (D) indicate an unclear quantification of the parameters which makes the synthesis impossible resulting in a significantly worse quality in imaging.

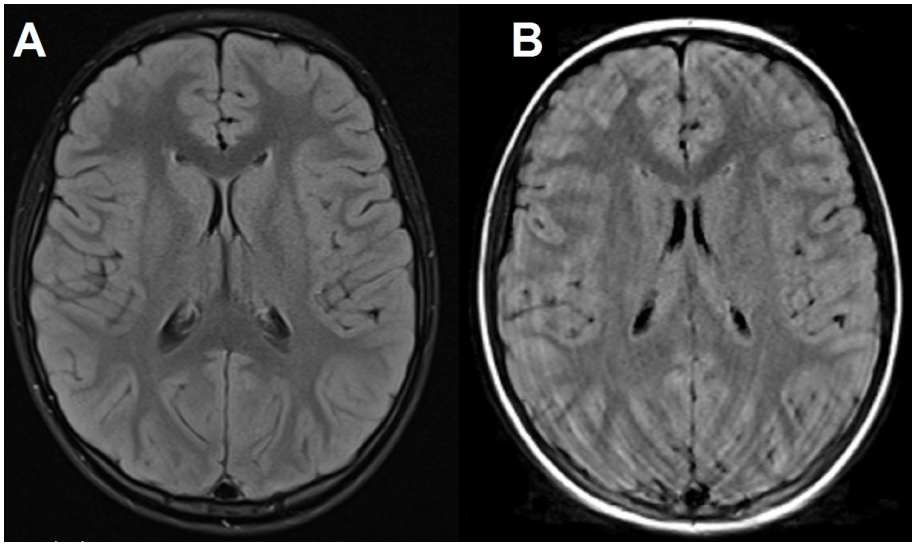

Figure 4.7: Conventional (A) and corresponding synthetic (B) T_2-FLAIR-weighted image showing the predisposition of the QRAPMASTER-approach for motion artefacts.

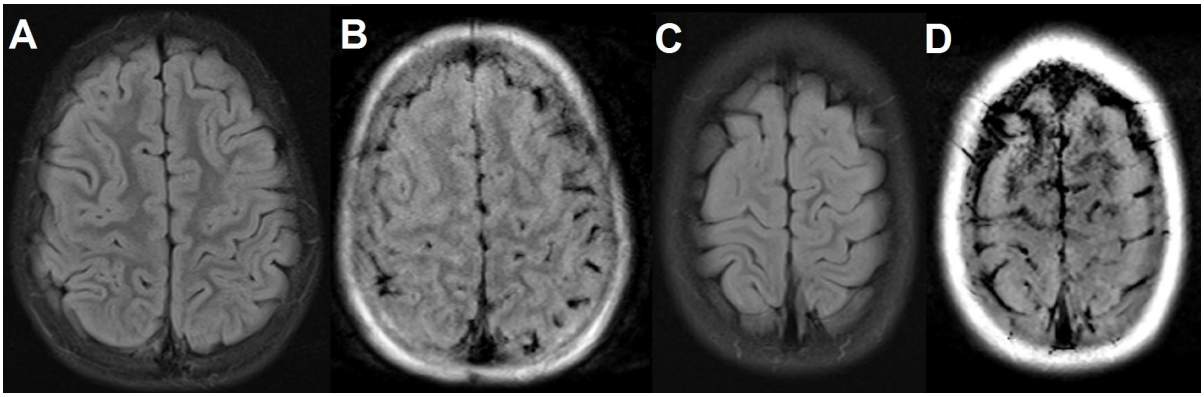

Figure 4.8: Conventional (A, C) and corresponding synthetic (B, D) T_2-FLAIR-weighted images with artefacts in synthetic images near the calvaria.

Figure 4.9 shows a zoomed part of T_1-weighted images where the red rectangle marks the region with a insufficient distinction of tissue types in the synthetic image (B). The radiologists stated a worse differentiation between the cerebral cortex and white matter.

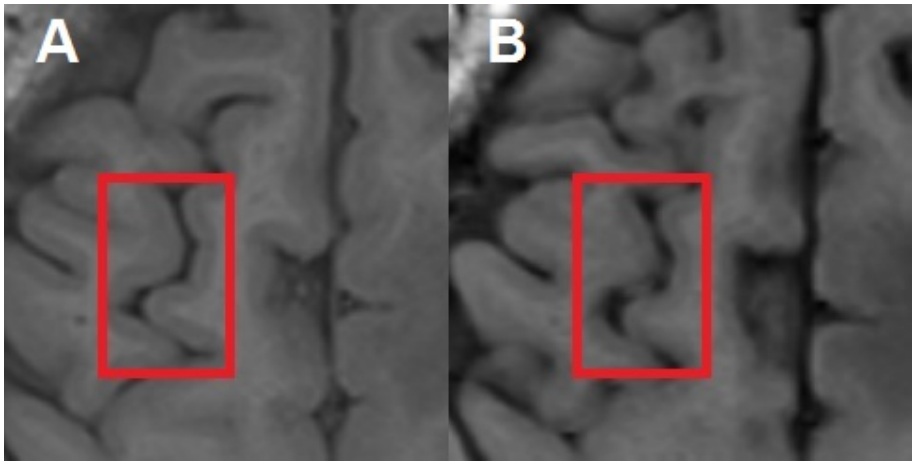

Figure 4.9: Example of a zoomed part in a conventional (A) and the corresponding synthetic (B) T_1-weighted image. Both images have identical acquisition parameters except the phase resolution: 80% in the conventional and 75% in the synthetic image. The red rectangle marks the region with a significant difference in the distinction of tissue types.

The following T_2-weighted images indicate another types of artefacts influencing the image quality. In figure 4.10 the radiologists identified pulsation artefacts more present in synthetic images (B). The zoomed part in the region of the cranial base or basal ganglia shows the handicap for the differentiation of the capsula interna. Figure 4.11 shows an example of higher noise of CSF in the synthetic image (B). The noise makes the boundary diffuse and therefore complicates the differentiation of tissues.

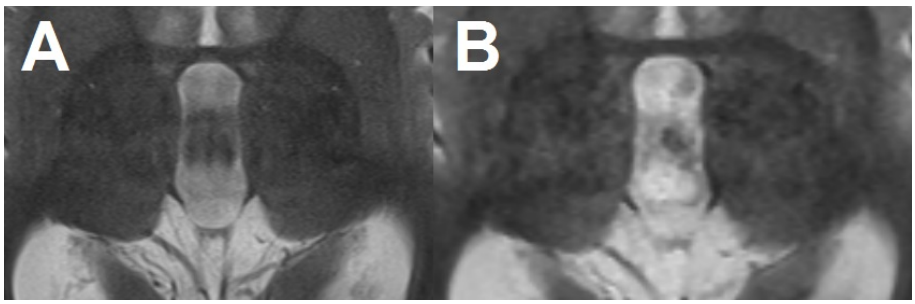

Figure 4.10: Zoomed part in the region of cranial base of a conventional (A) and synthetic (B) T_2-weighted images showing pulsation artefacts which hinder the differentiation of the capsula interna.

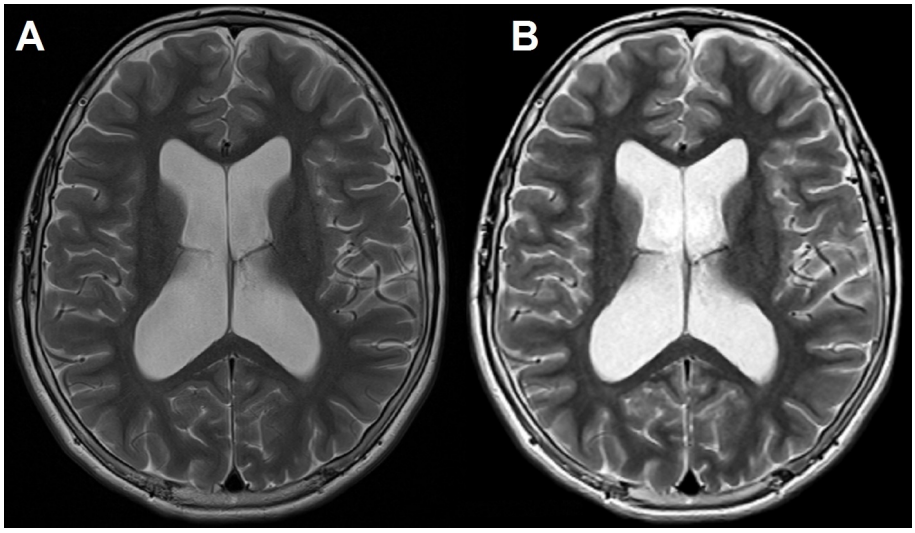

Figure 4.11: Reduced quality in synhtetic (B) compared to corresponding conventional (A) T_2-weighted image due to higher noise in CSF.

The here presented examples reveal further insights to the subjective rating of the radiologists. The difference between conventional and synthetic images can be explained by the different impression of the image or a lower potential for a sufficient distinction of tissue types, mostly for small structures. Therefore the latter one causes a limitation in the diagnosis of diseases linked to small structural changes. The blurring of the image can influence the detection of small and focal or lacunar lesions, either in the case of Multiple Sclerosis as well as vascular ones. Furthermore the diagnosis of small or diffuse tumors is hindered. In the case of pediatric radiology a periventricular leucoencephalopathy may not be properly recognized. However, it should be considered that these pathologies are not present in the here shown study.

In conclusion larger differences in the subjective assessment of the overall image quality in this study are evaluated than comparable literature reports. Comparing the scan times of the different acquisition methods in table 2.3 the following point can be stated: there is only a significant temporal benefit in the case of the necessity of T_2-, T_2-FLAIR- and T_1-weighted images. Many patients require only T_2- and T_2-FLAIR-weighted images which are acquired in nearly same time as the QRAPMASTER-sequence. The time-

saving benefit as a result of conventional sequences replaced by the MDME-sequence is only meaningful if the images are clinically acceptable for the radiologist. This assumption can only be stated for one out of the five raters. The general replacement for an acquisition time acceleration can therefore not be stated. In the case of a significant divergent rating, some examples including motion artefacts, lower possibility for differentiation of tissues and higher noise in synthetic images are presented influencing the diagnosis of different diseases. However, the application of the QRAPMASTER-approach involves some benefits.

4.3.1 Benefits for diagnosis

More WM/GM contrast can be generated with synthetic images already with the same setting of T_R and T_E as it was reported in table 3.12. Further improvements can be achieved by the optimization of the virtual acquisition parameters. This feature was only rarely used by the radiologists which may assume an already sufficient contrast. On the other hand especially experienced viewers are familiar with the given visualization making this possibility more or less redundant.

The segmentation allows for an objective measurement of the classified tissue type volumes. This allows for a quantification of follow-ups of a patient as well as the comparison to healthy controls. For this purpose, studies from Vagberg et al. [52] and McAllister et al. [53] were taken to provide reference curves. Exemplary, some of the reference curves regarding myelin-, CSF- and brain parenchyma volume are shown in figure 4.12. These curves allow for an age-related comparison to the average with providing the deviation of the normal value. Hence, especially brain atrophies like hydro- or microcephalus can be detected and diagnosed in an objective manner. A hydrocephalus correlates with the quantified volume of CSF and the Brain Parenchym Fraction (BPF), the volumes of WM, GM and NoN-WM/GM/CSF normalized by the ICV. [14] A microcephalus can be objectively indicated by a decreased volume of ICV and BPV. [54]

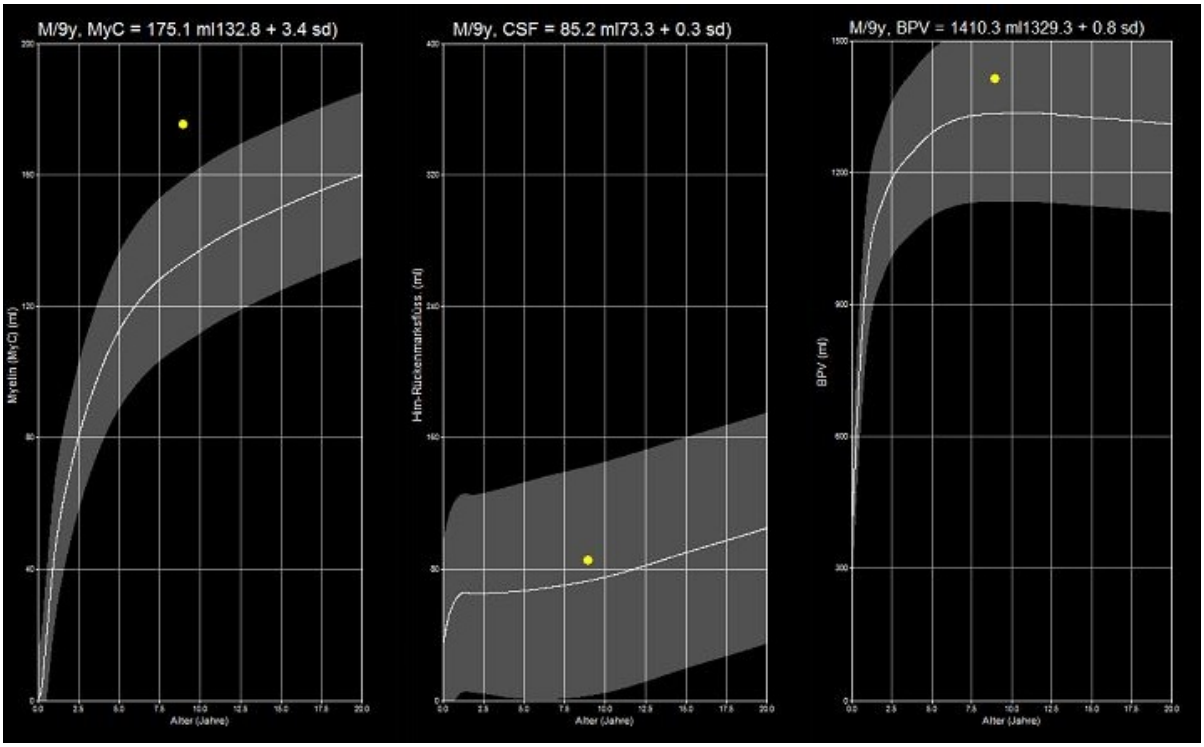

Figure 4.12: Reference curves for myelin-, CSF- and brain parenchyma volume of a 9-year old patient. The myelin volume is elevated by 3.4 standard deviations from the normal value of his age. Examples of misclassified myelin of this patient are shown in figure 4.13, B-D.

The essential benefit compared to conventional imaging is the quantification of myelin. Particularly for inexperienced readers the diagnosis of myelin correlated disorders is more difficult. As described in the introduction, Multiple sclerosis is associated with the quantity of myelin for adults. [2] [5] [7] Analogous for children or pediatric neuroimaging a developmental delay is linked to a lack of myelination. Therefore, a decrease in the myelin volume for a patient's age can be an indicator for a developmental disorder. Additionally useful information is provided by the volume decrease. The myelin determination was reported to be valid compared to other methods. [22] Nevertheless, during the assessment of the patient data some obvious errors in the myelin determination were detected. Figure 4.13 shows two patients which have a myelin volume 5.4 and 3.4 standard deviations above the normal value at their age. (A) shows overestimation of a 3-year old patient due to a shunt, in (B) parts of the eye are classified to myelin and (C) and (D) show myelin

in the region of the ICV border. The here presented examples show exemplary extreme cases to raise the awareness for such obvious deviations in the determination and is not representative for the majority of the patients.

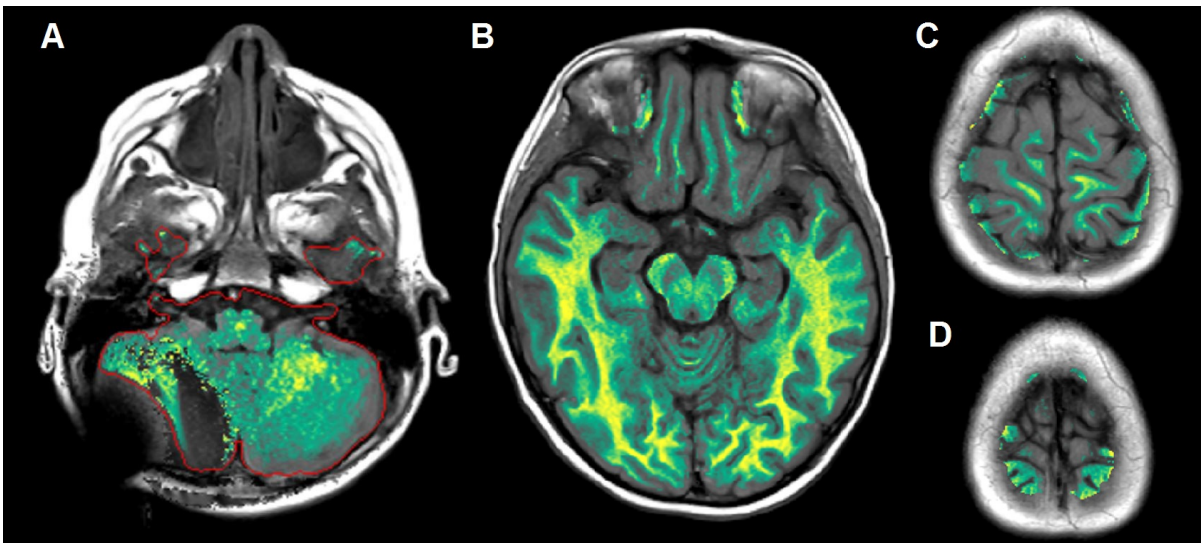

Figure 4.13: Obvious error in the determination of myelin for a 3-year old patient due to a shunt (A), and a 9-year old patient. (B) shows myelin in parts of the eyes, (C) and (D) represents inaccurate myelin in the region near to the skull.

4.4 Contrast differences

The evaluation of the phantom signal intensities revealed that there is more contrast in images acquired with a spin-echo scheme than in turbo spin-echo sequences. The T_2-weighted TSE images are acquired with a turbo factor of 17 and only achieve 83.66% of the single spin-echo contrast. The ratio for T_1-weighted images, which are acquired with turbo factor 3, is 91.32%.

Regarding the ratio of synthetically acquired images by the MDME-data to the clinical routine sequences, values of 108.87% (compared to TSE for T_2w) and 117.21% (SE for T_1w) are achieved. Contrary to these results, the in vivo comparison revealed a 141.58% and 113.37% better contrast in synthetic images. Possible explanations of the differences

in the results include the MTR and the quantitative values. Phantom 3 with the relatively short T_2 of $57.20ms$ was chosen to obtain a higher contrast and to compare mathematically more stable results. The PD or M_0 is usually smaller for WM and GM. [7] The major difference between the phantoms and the brain tissue refers to the MTR. The maximum MTR of a phantom was 22.04% in a mixture of 4% agarose which leads to a small value for T_2. For the comparison, phantoms with an MTR in the range of $7-13\%$ were chosen. In the literature a significantly higher signal reduction of $40-70\%$ for WM and $40-50\%$ for GM is reported. [55] Cercignani et al. [56] obtained an MTR of 41.2% for normal-appearing white-matter and 39.7% for normal-appearing grey matter. Also Davies et al. [57] reported similar values of 38.3% for WM and 32.4% for GM.

The amount of magnetization transfer effects is dependent on the cause for the behaviour, e.g. the off-resonance irradiation. Melki et al. [58] reported an increasing attenuation factor in dependance on the number of acquired slices which can be seen in figure 4.14. However, the number of slices in the study of this thesis is constant. Another possible reason for the differences in the contrast could be the echo train length. A longer length or a higher turbo factor means physically more refocusing pulses during the acquisition pronouncing the MT effects. The off-resonance irradiation of a single slice as a result of refocusing pulses of another slices can be the cause for this behaviour. With this theory the higher contrast in SE images compared to TSE images could be explained but the T_1-weighted images are acquired in a single-echo scheme whereas the QRAPMASTER sequence consists of 10 echoes in the explained study. Considering this study, additional reasons may lead to the contrast differences.

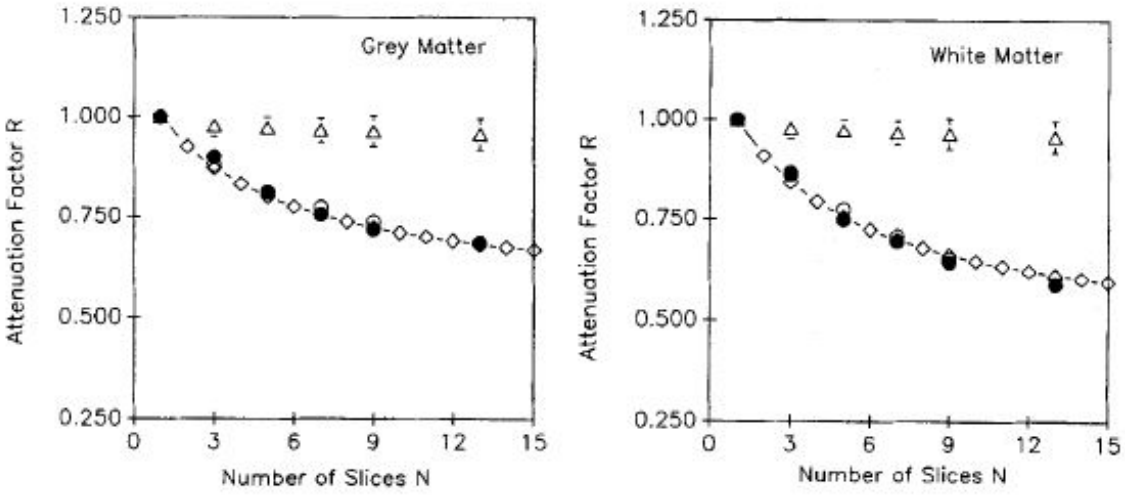

Figure 4.14: Proportionality of number of acquired slices to an attenuation factor equivalent to $1-MTR$. Both, white and grey matter, are more attenuated with the increasing number of acquired slices, by [58].

The comparison for contrast differences has major limitations. First, only a small number of phantoms is investigated and show only a qualitative behaviour compared to in vivo. Second, the MTR and also some quantitative values of these phantoms are differ quite much from the in vivo parameters. Blystad et al. [51] reported a possible theory for the contrast differences with a higher number of RF refocusing pulses leading to a stronger MT effect and resulting in a throughplane blurring causing the loss of contrast. The in vivo results can be a sign for the theory since the conventional T_2-weighted sequence consists of the longest echo train and shows the lowest contrast. For a full validation of this theory further measurements with different number of turbo factors would be necessary. Furthermore phantoms with a higher MTR or in vivo data should be considered.

4.5 Conclusion

The preliminary evaluation of the SSIM shows the sensitivity of the metric with respect to different causes. The downsampling and motion between the acquisitions has influences on the mathematical metric and also with a motion correction the error between the images is visible. The change of the phase resolution from 70% to 75% shows nearly no dependence on the SSIM.

The comparison of the QRAPMASTER quantification and gold-standard methods like IR or MSE revealed an error in the range of 5%. Combined with a high repeatability the approach can be considered as a relative accurate method when considering the gold-standard as ground truth. Limitations include the range of the quantified values which should be especially for T_1 known a priori to achieve accurate results by using adequate acquisition parameters as well as the possibility of multiexponential behaviour of different tissue types. In this thesis only monoexponential fitting is considered since the QRAPMASTER can only quantify this type accurately. There was a negative correlation between the the longitudinal magnetization and the MTR.

The scan time reduction with the usage of the QRAPMASTER based synthetic image reconstruction has limitations. First, a significant decrease of the scan time can only be achieved if T_2-, T_2-FLAIR- and T_1-weighted images are required. Second, the SSIM evaluation showed a restricted agreement between synthetic and conventional images. In combination with the subjective assessment an inferior quality for FLAIR-images was obtained and for T_2-images the consequence of the smaller acquisition matrix is significant. In conclusion, a replacement of conventional image stacks by synthesized images is limited by the acceptance of the radiologist who is diagnosing the patient.

The application of the QRAPMASTER sequence is beneficial in two ways. First, more WM/GM contrast can be generated with the same acquisition parameters. This effect can be increased by the optimization of the parameters which is efficient and trivial with the knowledge of the quantitative maps. The reason for the higher contrast may

be linked to MT effects combined with the echo train length but this assumption has major limitations requiring further experiments and evaluations. The second and probably main advantage over conventional MRI is the full automatic brain segmentation and the myelin measurement which can provide useful informations for a variety of diseases in pediatric neuroimaging. The introduced models can be considered as well-founded and in combination with the control for the shown artefacts, e.g. evoked by metal like brackets, mis-segmentation can be prevented resulting in accurate results for the volumes.

5 Literature

[1] R. W. Brown, Y. N. Cheng, E. M. Haacke, M. R. Thompson, and R. Venkatesan, *Magnetic Resonance Imaging: Physical Principles and Sequence Design.*, second edition ed. Wiley, 2014.

[2] J. B. M. Warntjes, M. Engström, and P. Tisell, A Lundberg, "Brain Characterization Using Normalized Quantitative Magnetic Resonance Imaging." *PloS one*, vol. 8, p. e70864, 2013.

[3] I. Leppert, C. Almli, R. Mckinstry, R. Mulkern, C. Pierpaoli, M. Rivkin, and B. Pike, "T2 Relaxometry of Normal Pediatric Brain Development." *Journal of Magnetic Resonance Imaging*, vol. 29, pp. 258 – 267, 02 2009.

[4] D. Gräfe, J. Frahm, D. Voit, and F. Hirsch, "Quantitative T1 mapping of the normal brain from early infancy to adulthood." *Pediatric Radiology*, vol. 51, pp. 1–7, 03 2021.

[5] J. West, J. B. M. Warntjes, and P. Lundberg, "Novel whole brain segmentation and volume estimation using quantitative MRI." *European Radiology*, vol. 22, pp. 998–1007, 2011.

[6] J. B. M. Warntjes, O. Dahlqvist Leinhard, J. West, and P. Lundberg, "Rapid Magnetic Resonance Quantification on the Brain: Optimization for Clinical Usage." *Magnetic Resonance in Medicine*, vol. 60, no. 2, pp. 320–329, 2008.

[7] P. Tofts, Ed., *Quantitative MRI of the Brain: Measuring Changes Caused by Disease.* Wiley, 2003.

[8] P. Schmitt, M. Griswold, P. Jakob, M. Kotas, V. Gulani, M. Flentje, and A. Haase,

"Inversion Recovery TrueFISP: quantification of T1, T2, and Spin Density." *Magnetic Resonance in Medicine*, vol. 51, pp. 661–7, 2004.

[9] D. Ma, V. Gulani, N. Seiberlich, K. Liu, J. Sunshine, J. Duerk, and M. Griswold, "Magnetic Resonance Fingerprinting." *Nature*, vol. 495, pp. 187–92, 2013.

[10] J. Hamilton and N. Seiberlich, "Machine Learning for Rapid Magnetic Resonance Fingerprinting Tissue Property Quantification." *Proceedings of the IEEE*, vol. PP, pp. 1–17, 2019.

[11] E. Henderson, G. McKinnon, T. Lee, and B. Rutt, "A fast 3D Look-Locker method for volumetric T1 mapping." *Magnetic Resonance Imaging*, vol. 17, no. 8, pp. 1163 – 71, 1999.

[12] J. B. M. Warntjes, O. Dahlqvist Leinhard, and P. Lundberg, "Novel Method for Rapid, Simultaneous T1, T2*, and Proton Density Quantification." *Magnetic Resonance in Medicine*, vol. 57, pp. 528–537, 2007.

[13] L. Leroi, "Quantitative MRI: towards fast and reliable T1, T2 and proton density mapping at ultra-high field." Ph.D. dissertation, Université Paris-Saclay, 2018.

[14] A. Hagiwara, J. B. M. Warntjes, M. Hori, C. Andica, M. Nakazawa, K. K. Kumamaru, O. Abe, and S. Aoki, "SyMRI of the Brain: Rapid Quantification of Relaxation Rates and Proton Density, With Synthetic MRI, Automatic Brain Segmentation, and Myelin Measurement." *Investigative Radiology*, vol. 52, no. 10, pp. 647–657, 2017.

[15] *System Requirements List for SyMRI 11*, SyntheticMR AB, 2020, Siemens Healthineers Scanner Settings.

[16] R. M. Henkelmann, G. J. Stanisz, and S. J. Graham, "Magnetization transfer in MRI: a review." *NMR in Biomedicine*, vol. 14, pp. 57–64, 2001.

[17] R. W. de Boer, "Magnetization transfer contrast Part 1: MR physics."

[18] R. M. Henkelmann, X. Huang, Q. Xiang, G. J. Stanisz, S. Swanson, and M. Bronskill, "Quantitative Interpretation of Magnetization Transfer." *Magnetic Resonance in Medicine*, vol. 29, no. 6, pp. 759–66, 1993.

[19] J. Eng, T. Ceckler, and R. Balaban, "Quantitative 1H Magnetization Transfer Imaging in Vivo." *Magnetic Resonance in Medicine*, vol. 17, pp. 304–14, 1991.

[20] K. P. Whittall, A. L. Mackay, D. A. Graeb, R. A. Nugent, D. K. B. Li, and D. W. Paty, "In vivo measurement of T2 distributions and water contents in normal human brain." *Magnetic Resonance in Medicine*, vol. 37, pp. 34–43, 1997.

[21] S. Deoni, D. Dean, J. O'Muircheartaigh, H. Dirks, and B. Jerskey, "Investigating white matter development in infancy and early childhood using myelin water faction and relaxation time mapping." *NeuroImage*, vol. 63, pp. 1038–53, 2012.

[22] A. Hagiwara, M. Hori, K. Kamagata, M. Warntjes, D. Matsuyoshi, M. Nakazawa, R. Ueda, C. Andica, S. Koshino, T. Maekawa, R. Irie, T. Takamura, K. Kumamaru, O. Abe, and S. Aoki, "Myelin Measurement: Comparison Between Simultaneous Tissue Relaxometry, Magnetization Transfer Saturation Index, and T1w/T2w Ratio Methods," *Scientific Reports*, vol. 8, p. 10554, 2018.

[23] J. B. M. Warntjes, M. Engström, A. Tisell, and P. Lundberg, "Modeling the Presence of Myelin and Edema in the Brain Based on Multi-Parametric Quantitative MRI." *Frontiers in Neurology*, vol. 7:16, 2016.

[24] I. Levesque and B. Pike, "Characterizing Healthy and Diseased White Matter Using Quantitative Magnetization Transfer and Multicomponent T-2 Relaxometry: A Unified View via a Four-Pool Model," *Magnetic Resonance in Medicine*, vol. 62, pp. 1487–96, 2009.

[25] Z. Wang, A. Bovik, H. Sheikh, and E. Simoncelli, "Image Quality Assessment: From Error Visibility to Structural Similarity." *IEEE Transactions on Image Processing*,

vol. 13, pp. 600 – 12, 2004.

[26] Z. Wang, A. Bovik, and H. Sheikh, "Structural Similarity Based Image Quality Assessment," *Digital Video Image Quality and Perceptual Coding, Ser. Series in Signal Processing and Communications*, 2005.

[27] The FIL Methods Group, *SPM12 Manual*, https://www.fil.ion.ucl.ac.uk/spm/doc/spm12_manual.pdf, Functional Imaging Laboratory, UCL Queen Square Institute of Neurology, 2020.

[28] T. B. Rieder, "Construction and evaluation of an MRI-phantom to simulate typical tissue parameters," Master's thesis, Graz University of Technology, 2019.

[29] K. A. Christensen, D. M. Grant, E. M. Schulman, and C. Walling, "Optimal determination of relaxation times of fourier transform nuclear magnetic resonance. Determination of spin-lattice relaxation times in chemically polarized species," *The Journal of Physical Chemistry*, vol. 78, pp. 1971–77, 1974.

[30] J. M. Homer and M. S. Beevers, "Driven-equilibrium single-pulse observation of T1 relaxation. A reevaluation of a rapid "new" method for determining NMR spin-lattice relaxation times," *Journal of Magnetic Resonance*, vol. 63, pp. 287–297, 1985.

[31] S. C. L. Deoni, B. K. Rutt, and T. M. Peters, "Rapid combined T1 and T2 mapping using gradient recalled acquisition in the steady state," *Magnetic Resonance in Medicine*, vol. 49, pp. 515 –26, 2003.

[32] R. Stollberger and P. Wach, "Imaging of the active B1 field in vivo." *Magnetic Resonance in Medicine*, vol. 35, pp. 246–51, 1996.

[33] S. Meiboom and D. Gill, "Modified Spin-Echo Method for Measuring Nuclear Relaxation Times," *Review of Scientific Instruments*, vol. 29, pp. 688–691, 1958.

[34] A. Petrovic, E. Scheurer, and R. Stollberger, "Closed-form solution for T2 mapping

with nonideal refocusing of slice selective CPMG sequences," *Magnetic Resonance in Medicine*, vol. 73, pp. 818–27, 2015.

[35] C. Labadie, J. H. Lee, W. D. Rooney, S. Jarchow, M. Aubert-Frecon, C. S. Springer, and H. E. Moeller, "Myelin Water Mapping by Spatially Regularized Longitudinal Relaxographic Imaging at High Magnetic Fields." *Magnetic Resonance in Medicine*, vol. 71, pp. 375–87, 2014.

[36] A. L. MacKay, C. Laule, I. M. Vavasour, T. A. Bjarnason, S. H. Kolind, and B. Mädler, "Insights into Brain Microstructure from the T2 distribution." *Magnetic Resonance Imaging*, vol. 24, no. 4, pp. 515–25, 2006.

[37] R. Heule, C. Ganter, and O. Bieri, "Variable Flip Angle T1 Mapping in the Human Brain with Reduced T2 Sensitivity Using Fast Radiofrequency-Spoiled Gradient Echo Imaging," *Magnetic Resonance in Medicine*, vol. 75, p. 1413–1422, 2016.

[38] W. Krauss, M. Gunnarsson, T. Andersson, and P. Thunberg, "Accuracy and Reproducibility of a Quantitative Magnetic Resonance Imaging Method for Concurrent Measurements of Tissue Relaxation Times and Proton Density." *Magnetic Resonance Imaging*, vol. 33, pp. 584–91, 2015.

[39] A. Hagiwara, M. Hori, J. Cohen-Adad, M. Nakazawa, Y. Suzuki, A. Kasahara, M. Horita, T. Haruyama, C. Andica, T. Maekawa, K. Kamagata, K. Kumamaru, O. Abe, and S. Aoki, "Linearity, Bias, Intra-Scanner Repeatability, and Inter-Scanner Reproducibility of Quantitative Multi-Dynamic Multi-Echo Sequence for Rapid Simultaneous Relaxometry at 3T: A Validation Study with a Standardized Phantom and Healthy Controls." *Investigative Radiology*, vol. 54, no. 2, pp. 39–47, 2019.

[40] J. B. M. Warntjes, "White Paper: How many echoes are required for a T2-relaxation time measurement?" SyntheticMR AB, Tech. Rep., 2021.

[41] J. Oh, S. Cha, A. H. Aiken, E. T. Han, J. C. Crane, J. A. Stainsby, G. A. Wright,

W. P. Dillon, and S. J. Nelson, "Quantitative apparent diffusion coefficients and T2 relaxation times in characterizing contrast enhancing brain tumors and regions of peritumoral edema." *Journal of Magnetic Resonance Imaging*, vol. 21, no. 6, pp. 701–8, 2005.

[42] S. C. L. Deoni, T. M. Peters, and B. K. Rutt, "High-resolution T1 and T2 mapping of the brain in a clinically acceptable time with DESPOT1 and DESPOT2." *Magnetic Resonance in Medicine*, vol. 53, no. 1, pp. 237–41, 2005.

[43] C. A. McKenzie, Z. Chen, D. J. Drost, and F. S. Prato, "Fast acquisition of quantitative T2 maps." *Magnetic Resonance in Medicine*, vol. 41, no. 1, pp. 208–12, 1999.

[44] A. Watanabe, C. Boesch, T. Obata, and S. E. Anderson, "Effect of Multislice Acquisition on T1 and T2 Measurements of Articular Cartilage at 3T." *Journal of Magnetic Resonance Imaging*, vol. 26, pp. 109 – 117, 2007.

[45] M. Cercignani, N. Dowell, and P. Tofts, *Quantitative MRI of the Brain: Principles of Physical Measurement.*, second edition ed. CRC Press, 2018.

[46] L. Tanenbaum, A. Tsiouris, A. Johnson, T. Naidich, M. DeLano, E. Melhem, P. Quarterman, S. Parameswaran, A. Shankaranarayanan, M. Goyen, and A. Field, "Synthetic MRI for Clinical Neuroimaging: Results of the Magnetic Resonance Image Compilation (MAGiC) Prospective, Multicenter, Multireader Trial." *American Journal of Neuroradiology*, vol. 38, pp. 1103–1110, 2017.

[47] S. M. Lee, Y. H. Choi, J.-E. Cheon, I.-O. Kim, S. H. Cho, W. H. Kim, H. J. Kim, H.-H. Cho, S.-K. You, S.-H. Park, and M. J. Hwang, "Image quality at synthetic brain magnetic resonance imaging in children." *Pediatric Radiology*, vol. 47, no. 12, pp. 1638–47, 2017.

[48] A. M. Betts, J. L. Leach, B. V. Jones, B. Zhang, and S. Serai, "Brain imaging with synthetic MR in children: clinical quality assessment." *Neuroradiology*, vol. 58, no. 10,

pp. 1017–26, 2016.

[49] F. D. Giuliano, S. Minosse, E. Picchi, G. A. Marfia, V. D. Ros, M. Muto, M. Muto, C. A. Pistolese, A. Laghi, F. Garaci, and R. Floris, "Comparison between synthetic and conventional magnetic resonance imaging in patients with multiple sclerosis and controls." *Magnetic Resonance Materials in Physics, Biology and Medicine*, vol. 33, pp. 549–57, 2019.

[50] A. Hagiwara, Y. Otsuka, M. Hori, Y. Tachibana, K. Yokoyama, S. Fujita, C. Andica, K. Kamagata, R. Irie, S. Koshino, T. Maekawa, L. Chougar, A. Wada, and S. Aoki, "Improving the Quality of Synthetic FLAIR Images with Deep Learning Using a Conditional Generative Adversarial Network for Pixel-by-Pixel Image Translation." *American Journal of Neuroradiology*, vol. 40, pp. 224–30, 2019.

[51] I. Blystad, J. B. M. Warntjes, O. Smedby, A.-M. Landtblom, P. Lundberg, and E.-M. Larsson, "Synthetic MRI of the brain in a clinical setting." *Acta Radiologica*, vol. 53, no. 10, pp. 1158–63, 2012.

[52] M. Vågberg, K. Ambarki, T. Lindqvist, R. Birgander, and A. Svenningsson, "Brain parenchymal fraction in an age-stratified healthy population – determined by MRI using manual segmentation and three automated segmentation methods." *Journal of Neuroradiology*, vol. 43, no. 6, pp. 384–391, 2016.

[53] A. McAllister, J. Leach, H. West, B. Jones, B. Zhang, and S. S., "Quantitative Synthetic MRI in Children: Normative Intracranial Tissue Segmentation Values during Development." *American Journal of Neuroradiology*, vol. 38, pp. 2364–2372, 2017.

[54] J. Leach, "Case study: Getting the Whole Pediatric Picture with MR Quantification in Under 6 Minutes." SyntheticMR AB, Tech. Rep., 2020.

[55] D. W. McRobbie, E. A. Moore, M. J. Graves, and M. R. Prince, *MRI: From Picture to Proton.*, second edition ed. Cambridge University Press, 2006.

[56] M. Cercignani, M. Bozzali, G. Iannucci, G. Comi, and M. Filippi, "Magnetisation transfer ratio and mean diffusivity of normal appearing white and grey matter from patients with multiple sclerosis." *Journal of Neurology, Neurosurgery and Psychiatry*, vol. 70, pp. 311–17, 2001.

[57] G. Davies, D. Altmann, A. Hadjiprocopis, W. Rashid, D. Chard, C. Griffin, P. Tofts, G. Barker, R. Kapoor, A. Thompson, and D. Miller, "Increasing normal-appearing grey and white matter magnetisation transfer ratio abnormality in early relapsing-remitting multiple sclerosis." *Journal of Neurology*, vol. 252, pp. 1037–44, 2005.

[58] P. S. Melki and R. V. Mulkern, "Magnetization Transfer Effects in Multislice RARE Sequences." *Magnetic Resonance in Medicine*, vol. 24, pp. 189–95, 1992.